https://doi.org/10.1016/j.pecs.2018.01.001

Advances and challenges in alkaline anion exchange membrane fuel cells

Z.F. Pan[a], L. An[a]*, T.S. Zhao[b]*, Z.K. Tang[c]

[a] Department of Mechanical Engineering, The Hong Kong Polytechnic University, Hung Hom, Kowloon, Hong Kong SAR, China.

[b] Department of Mechanical and Aerospace Engineering, The Hong Kong University of Science and Technology, Clear Water Bay, Kowloon, Hong Kong SAR, China.

[c] Department of Physics, The Hong Kong University of Science and Technology, Clear Water Bay, Kowloon, Hong Kong SAR, China.

*Corresponding authors.

[a] Email: liang.an@polyu.edu.hk (L. An)

[b] Email: metzhao@ust.hk (T.S. Zhao)

Abstract

The last several decades have witnessed the rapid development of alkaline anion exchange membrane fuel cells (AAEMFCs) that possess a series of advantages as compared to acid proton exchange membrane fuel cells, such as the enhanced electrochemical kinetics of oxygen reduction reaction and the use of inexpensive non-platinum electrocatalysts, both of which are rendered by the alkaline medium. As an emerging power generation technology, the significant progress has been made in developing the alkaline anion exchange membrane fuel cells in recent years. This review article starts with a general description of the setup of AAEMFCs running on

hydrogen and physical and chemical processes occurring in multi-layered porous structure. Then, the electrocatalytic materials and mechanisms for both hydrogen oxidation and oxygen reduction are introduced, including metal-based, metal oxide-based, and non-metal based electrocatalysts. In addition, the chemistries of alkaline anion exchange membranes (AAEMs), e.g. polymer backbone and function groups, are reviewed. The effects of pre-treatment, carbonate, and radiation on the performance of AAEMs are concluded as well. The effects of anode and cathode ionomers, structural designs, and water flooding on the performance of the single-cell are explained, and the durability and power output of a single-cell are summarized. Afterwards, two innovative system designs that are hybrid fuel cells and regenerative fuel cells are presented and mathematical modeling on mass transport phenomenon in AAEMFCs are highlighted. Finally, the challenges and perspectives for the future development of the AAEMFCs are discussed.

Keywords: Fuel cells; alkaline anion exchange membranes; electrocatalysts; single-cell designs; power density

1. Introduction

We have to adopt new energy supply technologies that utilize renewable energy sources [1-8], due to the current energy and environmental issues we are facing today. Among them, fuel cells have been considered as one of the most promising clean and efficient power generation technologies for a sustainable future [9-15]. Hence, tremendous efforts have been made on the development of fuel cells [16-22]. Alkaline fuel cells (AFCs) that use potassium hydroxide (KOH) solution as the liquid electrolyte have shown much success since the 1960s, particularly working as the energy supply devices powering the Gemini and Apollo spacecraft, due to the fact that the electrochemical kinetics of the oxygen reduction reaction (ORR) is much enhanced resulting from the alkaline environment, allowing the absence of expensive noble metals in preparing the electrocatalysts and thus reducing the cost of the fuel cell system [23-25]. Despite its compelling merits, however, this fuel cell technology has not made sufficient progress in market presence yet. One significant factor preventing widespread commercialization is the use of the alkaline liquid electrolyte, which may cause two problems [26]. One is the carbonate, the product of the side reaction between hydroxide ions in the liquid electrolyte and carbon dioxide in the air, reducing the concentration of hydroxide ions and potentially blocking the pores of the porous electrode via the precipitation of the metal carbonate [27-29]. The other is electrode flooding and drying

problems, which are more likely to arise if the liquid electrolyte is not well controlled [30,31].

To address the issues caused by involving the liquid electrolyte, ion exchange membrane fuel cells that employ solid electrolyte have received ever-increasing attention [32-36]. The use of solid electrolyte membranes in fuel cells can remove the carbonate problem and avoid the liquid electrolyte management. Hence, extensive efforts have been devoted to developing alkaline AAEMFCs and remarkable achievements have been made [37-39]. In addition, many other advantages of the AAEMFCs are summarized as follows: (1) faster electrochemical kinetics of the ORR in alkaline media [40,41], (2) absence of noble metal electrocatalysts [42,43], (3) minimized corrosion problems in the alkaline environment [44,45], and (4) cogeneration of electricity and valuable chemicals [46-48]. Currently, compressed hydrogen and liquid alcohol are the most common fuels used in AAEMFCs. The liquid alcohols, e.g. methanol, ethanol, formate, and small polyalcohols, are convenient to handle, store, and transport [49-51]. Another advantage is that they are easy to be acquired from the abundant biomass, suggesting that the process is carbon-neutral and the sources are sufficient [52]. Borohydrides with high energy density are also recognized as a suitable fuel for AAEMFCs due to the fact that they are easy to handle, store, and transport as well. In addition, the products in the anode effluent can be

converted back to borohydrides, which is beneficial for a sustainable future [18]. In consideration of degree of commercialization, this article will focus on the AAEMFCs running on hydrogen that is the maturest in commercialization. The objective of this review is to provide a general description of this type of fuel cell, introduce electrocatalytic materials for hydrogen oxidation and oxygen reduction reactions, summarize the alkaline anion exchange membranes (AAEM) and single-cell performance, as well as highlight the remaining challenges and future directions.

2. General description

In principle, the structure of AAEMFCs is just borrowed from proton exchange membrane fuel cells (PEMFCs), with the main difference that the solid membrane is an AAEM instead of a proton exchange membrane (PEM). In AAEMFCs, the charge carrier is OH^- transporting through the AAEM from the cathode to the anode, while H^+ works as charge carrier transporting through the PEM from the anode to the cathode in PEMFCs. Hence, AAEMFCs have been considered as an alternative to PEMFCs and garnered renewed attention recently due to the above-mentioned advantages. Currently, many researchers have put their focus on the synthesis of polymeric alkaline anion exchange membranes with high ionic conductivity and excellent chemical stability, as well as novel electrocatalysts that are favorable and low cost [53-63].

Like other fuel cells, a single AAEMFC consists of three main components, i.e. an

anode, a cathode, and an AAEM, so-called membrane electrode assembly (MEA), as shown in Fig. 1. Specifically, the integrated multi-layered porous structure is constituted sequentially by an anode gas diffusion layer (GDL), an anode catalyst layer (CL), an AAEM, a cathode CL, and a cathode GDL. The GDLs in the anode and cathode that are both composed of two layers, a backing layer (BL) based on carbon paper or carbon cloth and a micro-porous layer (MPL) that is comprised of carbon powders mixed with hydrophobic polymer (typically PTFE). The CLs are usually made of electrocatalysts mixed with ionomer, resulting in the formation of triple-phase boundaries (TPBs) for the electrochemical reactions, i.e., hydrogen oxidation reaction (HOR) and ORR. Particularly, the GDL provides the support for the corresponding CL, distributes the reactants uniformly, and transports electrons to the current collector. Recently, Li et al. [64] proposed a metal foam-based electrode integrating the flow field, BL, MPL, and CL into a whole, which facilitates the mass and charge transport and extends the TPBs. The anode and the cathode are separated by an AAEM, preventing the hydrogen crossover to the cathode, which causes the fuel loss and mixed potential. Meanwhile, the pathway for conducting hydroxide ions is built up. The external circuit provides the channel for the electrons to form the loop.

On the anode, humidified hydrogen is fed to the anode flow channel and transported through the anode GDL, finally to the anode CL, where hydrogen reacts with hydroxide

ions to produce water and electrons. The anodic reaction is:

$$H_2+2OH^-\rightarrow 2H_2O+2e^- \qquad E_a^0=-0.83V \qquad (1)$$

On the cathode, humidified oxygen supplied by the cathode flow channel is transported through the cathode GDL to the cathode CL, where oxygen is reduced in the presence of water to produce hydroxide ions:

$$\frac{1}{2}O_2+H_2O+2e^-\rightarrow 2OH^- \qquad E_c^0=0.40V \qquad (2)$$

Then, the generated hydroxide ions are conducted through the AAEM for the HOR. Therefore, the overall reaction combining the HOR given by equation (1) and the ORR given by equation (2) is expressed as follows:

$$H_2+\frac{1}{2}O_2\rightarrow H_2O \qquad E^0=1.23V \qquad (3)$$

It should be noted that the theoretical cell voltage cannot be realized due to a series of irreversible losses, such as overpotentials caused by activation, ohmic, and mass-transport processes. In addition, it is worthwhile to note that the hydrogen and oxygen gases need humidification before fed into the fuel cell in order to achieve better performance. The major reasons can be summarized as follows: (1) one of the main deficiencies of AAEMs is that the conductivity of AAEMs is sensitive to relative humidity. Hence, the humidified gases that are supplied to the channel can humidify the membrane, enhancing the ionic conductivity and thus reducing the internal resistance; (2) in consideration of the electrochemical reaction on the cathode, humidified oxygen

provides the essential water molecular that will react with oxygen to form hydroxide ions. In the following section, the electrocatalytic materials for HOR, including metal electrocatalysts and metal oxide electrocatalysts, are reviewed and discussed.

3. Electrocatalytic materials and mechanisms for hydrogen oxidation reaction in alkaline media

Platinum (Pt) is generally used as the electrocatalysts for hydrogen oxidation in AAEMFCs, which negates a prime advantage of alkaline fuel cells, which is potentially free from Pt-based electrocatalysts. The anodic reaction in acid media is expressed:

$$H_2 \rightarrow 2H^+ + 2e^- \quad (4)$$

while, the product of the anodic reaction in alkaline media is water:

$$H_2 + 2OH^- \rightarrow 2H_2O + 2e^- \quad (5)$$

Particularly, the HOR activity on the platinum group metals (PGM) decreases with increasing the pH value. Sheng et al. [65] reported that the electrochemical kinetics of the HOR were at least two orders of magnitude slower in alkaline media than that in acid media. Similarly, Durst et al. [66] demonstrated that the exchange current densities on Pt/C, Pd/C, and Ir/C in acidic media (pH=0) were all declined by about two orders of magnitude when the pH increased to 13. The oxophilicity did not contribute to enhancing the HOR activity in high pH. They suggested that the pH-dependent HOR activity was associated with the hydrogen binding energy (HBE). It was explained by

Sheng et al. [67] that HBE is likely the sole descriptor for the HOR/HER activity on Pt in pH-buffered electrolytes. The results from the rotating disk electrode test and cyclic voltammetry test showed that the HOR/HER activity decreased and HBE linearly increased with the increasing pH, respectively. It was proposed that the adsorbed OH species did not participate in the reaction, but influenced the HBE, leading to the reduce of HOR/HER activity. However, Ledezma-Yanez et al. [68] argued that the pH-dependent HBE change did not account for the HER overpotential on Pt(111). They observed that both the HER and H-underpotential deposition (H-UPD) were slower in alkaline media even if the thermodynamic driving force was the same, implying that hydrogen adsorption was a kinetically hindered step. Therefore, it was elucidated that at the potential of H-UPD and HER, the interfacial water network interacted with the strong interfacial electric field in alkaline media, resulting in the water network more rigid and more difficult to reorganize during the charge transfer through the electrical double layer. Consequently, the rate of hydrogen adsorption was severely influenced by the energetic barrier derived from the strength of the interfacial electric field. To overcome this constrain, many efforts have been made to develop non-platinum catalysts for HOR with high activity at a lower cost [69-84]. This section will describe some types of electrocatalyst, including metals and metal oxides.

3.1. Metals

Many efforts have been made to increase the metal electrocatalyst activity aiming at reducing the amount of Pt, even replacing Pt [53,69,70,74,77,79-81]. Since palladium (Pd) is similar to Pt in electronic properties, the HOR on the Pd surface may follow the same mechanism. In addition, Pd/C and Pt/C exhibited comparable HOR activity examined by the thin-film rotating disk electrode in acid environment [78]. Hence, many efforts have been conducted to improve the electrocatalytic activity of Pd [53,69,79-81]. Bakos et al. [53] studied the synergetic activity of Pd/Ni for the HOR in alkaline media. Fig. 2 illustrated the surface and size distribution of the Pd/Ni. It was shown that 17% of a Ni film covered by a Pd layer of around 1.5 nm thickness exhibited the highest HOR activity than other Pd coverages. For the Pd coverage lower than 17%, the current density increased linearly with the coverage, and then reached a plateau upon further increase, which is attributed to the diffusion limit for the HOR process. Similarly, Alesker et al. [69] used Pd nanoparticles to grow onto Ni nanoparticles as the HOR electrocatalyst, resulting in a peak power density of 400 mW cm^{-2} in an AAEMFC fabricated with Pd (1.5 mg cm^{-2}) as anode electrocatalyst and Ag (3 mg cm^{-2}) as cathode electrocatalyst with dry hydrogen fed at a flow rate of 200 standard-state cubic centimeter per minute (sccm) and the air fed at a flow rate of 1000 sccm. It was indicated that the HOR activity was enhanced, which was evidenced by the negative shift of the HOR onset potential. In addition, it was believed that the high activity was

193 ascribed to the presence of the OH_{ads} on the Ni surface, providing a faster reaction route
194 for the HOR. In addition, the nickel-based electrocatalysts for the HOR have also been
195 investigated [74-76]. Hu et al. [74] studied the feasibility of tungsten doped nickel (Ni-
196 W) as the anode electrocatalyst for AAEMFCs. The results showed that the equilibrium
197 potential of the HOR on Ni-W was established in 200 s, indicating that the electronic
198 surface of Ni was tuned and the oxidation tolerance of Ni surface was significantly
199 enhanced. It was shown that the highest power density reached 40 mW cm^{-2} with
200 humidified hydrogen and oxygen both at a flow rate of 50 sccm at 60ºC, when Ni-W
201 (17.5 mg cm^{-2}) and CoPPY/C (2 mg cm^{-2}) were employed as anode and cathode
202 electrocatalysts, respectively. To further improve the HOR activity, Sheng et al. [75]
203 synthesized noble-metal-free electrocatalyst via electro-depositing a ternary metallic
204 CoNiMo on a polycrystalline gold (Au) disk electrode. It was shown that the HOR
205 activity of CoNiMo was 20 times higher than pure Ni in alkaline media, which is
206 attributed to the weakened hydrogen binding energy on CoNiMo. Zhuang et al. [76]
207 prepared a composite electrocatalyst, nitrogen-doped carbon nanotubes supporting
208 nickel nanoparticles (Ni/N-CNT), to replace Pt for an efficient HOR. Although the N-
209 CNT did not directly contribute the HOR activity, it could significantly improve the
210 catalytic activity of Ni nanoparticles, meaning that the mass activity and exchange
211 current density of the Ni/N-CNT were increased 33 and 21 times than that of bare Ni

212 nanoparticles, respectively. It was indicated that the high HOR activity was ascribed to
213 the synergetic effect of N atom and Ni. Ohyama et al. [70] synthesized small ruthenium
214 nanoparticles by liquid phase reduction of $RuCl_3$ by $NaBH_4$ under pH control and
215 characterized the structure of the Ru/C via X-Ray diffraction (XRD), transmission
216 electron microscope (TEM), and X-ray absorption fine structure (XAFS) spectroscopy.
217 The results indicated that the diameter of Ru particles was 3nm under pH control
218 (pH=7), which was much smaller than that without pH control (pH=2). The peak power
219 densities of a H_2/O_2 fuel cell fed with humidified H_2 and O_2 both at a flow rate of 500
220 sccm employing Tokuyama A201 as AAEM, Pt/C (0.5 mg cm^{-2}) as cathode
221 electrocatalyst, and 3 nm Ru/C, 3 nm Pt/C, and 11 nm Ru/C as anode electrocatalysts
222 are 250, 185, and 134 mW cm^{-2}, respectively. In addition, the cell performance with
223 using Ru/C was increased with the cycle of fuel cell operation, primarily because the
224 Ru species was reduced during fuel cell operation, resulting in the highly active sites
225 for hydrogen adsorption and oxidation. Recently, Alia et al. [77] synthesized copper
226 (Cu) nanowires (NWs) supported Pt (Pt/CuNWs) with a 100-nm diameter and a 25-40
227 μm length for HOR in alkaline media. It was indicated that compared to Pt/C, the area
228 and mass exchange current densities of Pt/CuNWs were promoted by 3.5 and 1.9 times,
229 respectively. Therefore, the improved performance was attributed to compressive strain
230 on Pt and more adsorption of hydroxyl species provided by inclusion of Cu. In summary,

231 the novel HOR metal electrocatalysts that exhibit comparable performance with Pt are
232 mainly based on Pd, Ni, and Ru. Although the great progress has been made recently,
233 attentions also should be paid to developing other substrate materials that are more cost-
234 effective.

235 **3.2. Metal oxides**

236 Although the metal electrocatalysts are promising, metal oxide electrocatalysts that are
237 inexpensive as well have been extensively studied [71-73,82,83]. Lu et al. [71]
238 synthesized Cr-decorated Ni (CDN) nanoparticles and tested the effect of modulation
239 on the surface reactivity toward oxygen via XRD and X-ray photoelectron spectroscopy
240 (XPS). It was indicated that CDN can be easily activated by gaseous hydrogen at room
241 temperature, resulting in the employment of CDN as anode electrocatalyst. They
242 showed that a peak power density of 50 mW cm^{-2} was achieved when CrO_x/Ni (5 mg
243 cm^{-2}) and Ag/C (1 mg cm^{-2}) were used as anode and cathode electrocatalysts,
244 respectively, as well as a quaternary ammonium polysulphone membrane with H_2
245 (relative humidity (RH) = 100%) in the anode and O_2 (RH = 100%) in the cathode at
246 60°C. Lu et al. [72] also indicated that the CrO_x was believed to weaken the binding of
247 oxygen to the Ni nanoparticles, resulting in the mild deactivation of Ni via oxidation.
248 Miller et al. [73] demonstrated that Pd nanoparticles deposited by CeO_2 showed
249 excellent HOR activity. The single fuel cell fabricated with Pd/C-CeO_2 (0.3 mg cm^{-2})

as anode electrocatalyst and Ag (3 mg cm^{-2}) as cathode electrocatalyst yielded a maximum power density of 500 mW cm^{-2}, when dry hydrogen was fed into the anode at a flow rate of 200 sccm and air was fed into the cathode at a flow rate of 1000 sccm. While pure Pd was employed as anode electrocatalyst, the peak power density was decreased to 100 mW cm^{-2}. CeO_2, one of the most oxygen deficient compounds, is known for the rapid saturation with hydroxide ions [82] and spillover of hydroxide ions to support metal nanoparticles [83]. It was demonstrated that the Pd-H bonds were weakened and the supply of the OH_{ad} was enhanced, accelerating the overall HOR. Recently, Miller et al. [84] studied the effect of Pd loadings on the performance of Pd/C-CeO_2. The results from the single fuel-cell test showed that the Pd/C-CeO_2 with 10 wt.% Pd loading yielded the highest power density of 500 mW cm^{-2} with Pd/C-CeO_2 (0.3 mg cm^{-2}) as anode electrocatalyst and Ag (3 mg cm^{-2}) as cathode electrocatalyst when dry hydrogen was fed into the anode at a flow rate of 200 sccm and air was fed into the cathode at a flow rate of 1000 sccm. While 6 wt.% Pd and 20 wt. % Pd loadings in the single fuel cell exhibited 390 and 460 mW cm^{-2} under the same conditions, respectively. Meanwhile, the stability of Pd/C-CeO_2 was superior than Pd/C under harsh potential cycling.

In summary, great progress has been made in the development of HOR electrocatalysts with high catalytic activity and low cost to replace Pt in AAEMFCs. Although

numerous investigations have been reported in recent literature, the stability of non-platinum electrocatalysts is still the major limiting factor for the commercial applications, which is derived from the morphological changes during the process of electrocatalyst operation. Therefore, the future research direction could be focused on enhancing the durability of the newly synthesized electrocatalysts without sacrificing the HOR activity.

4. Electrocatalytic materials and mechanisms for oxygen reduction reaction in alkaline media

Extensive studies have been conducted on the oxygen reduction reaction in alkaline media. The electrocatalytic reduction of oxygen proceeds either two-electron pathway or four-electron pathway [85]. Fig. 3 (a) generally illustrated the ORR process in alkaline media. The subscripts of sa, a, b, and *denoted strongly adsorbed, weakly adsorbed, bulk, and the vicinity of the electrode, respectively. All reactions could be concluded as follows:

$$O_{2,a} + e^- \rightarrow O^-_{2,a} \quad (6)$$

$$O^-_{2,a} + H_2O + e^- \leftrightarrow HO^-_{2,a} + OH^- \quad (7)$$

$$O_{sa} + e^- \rightarrow O^-_{sa} \quad (8)$$

$$O^-_{2,sa} + H_2O + e^- \rightarrow HO^-_{2,sa} + OH^- \quad (9)$$

$$HO^-_{2,sa} + e^- \leftrightarrow O^-_{sa} + OH^- \quad (10)$$

$$O_{sa}^{-} + e^{-} + H_2O \rightarrow 2OH^{-} \quad (11)$$

$$2O_{2,a}^{-} + H_2O \rightarrow O_{2,a} + HO_{2,a}^{-} + OH^{-} \quad (12)$$

$$2HO_{2.a}^{-} \rightarrow 2OH^{-} + O_{2,a} \quad (13)$$

$$HO_{2,sa}^{-} \rightarrow OH^{-} + O_{sa} \quad (14)$$

$$O_{2,sa}^{-} \rightarrow O_{sa} + O_{sa}^{-} \quad (15)$$

It should note that only one electron was involved in the above mentioned reactions. In the direct four-electron pathway, the first step was the formation of weakly adsorbed species via the diffusion of bulk oxygen. Then the weakly adsorbed species became the strongly adsorbed species through chemisorption, which were the key intermediate in the process. As the strongly adsorbed species were chemisorbed, the reactions associated with them were mainly irreversible processes (k_3, k_4, k_{12}, k_{13},). In the two-electron pathway, the weakly adsorbed species were the critical intermediate. The difference of the strongly adsorbed species and the weakly adsorbed species lied on the ability to desorb directly and go into solution. Since the weakly adsorbed species were more likely to be physisorbed, adsorption-desorption equilibrium with corresponding species in solution was established as shown in k_2 and k_{-2}, k_{20} and k_{-20}, as well as k_{25} and k_{-25}. It was believed that a superoxide ion $HO_{2,a}^{-}$ could be formed after the oxygen molecule received an electron. Subsequently, as the weakly bound superoxide ion was unstable in aqueous solution, thus it could rapidly go through either a chemical pathway

decomposing into $HO_{2,a}^-$ and oxygen or a electrochemical pathway receiving an electron and a proton to form $HO_{2,a}^-$. Analogously, the $HO_{2,a}^-$ possessed two reaction routes: one was to be chemisorbed producing $HO_{2,sa}^-$, and the other was to diffuse into the bulk solution. It can be seen from Fig. 3 (b) that the formation of peroxide intermediate species, HO_2^- and H_2O_2, is more energetically favorable during the ORR due to the lower overpotential. Thus, the ORR kinetics are dramatically more sluggish in acid media than that in alkaline one, which can be explained by the stabilization effect of the peroxide intermediate of HO_2^- caused by the negative charge [86]. When the fuel cell is discharging, the cathode potential is higher than the potential of zero charge, resulting in the positive charge on the electrode Hence, it is HO_2^- rather than the neutral molecule of H_2O_2 that can be adsorbed on the cathode derived from the electrostatic attraction and further to be reduced on the active sites. As the ORR obstruction has been unveiled, a gate of synthesizing variety of electrodes has been opened. We herein summarize the property and performance of the electrocatalysts reported in recent literatures, including precious metal electrocatalysts, non-precious metal electrocatalysts, and non-metal electrocatalysts.

4.1. Precious metals

Undoubtedly, Pt/C is still the most commonly used electrocatalyst, which is also the performance criterion of newly developed materials. However, the high cost and rarity

have hindered the utilization of Pt in fuel cells, resulting in numerous research efforts led to the development of non-Pt noble metal electrocatalysts with high activity for AAEMFCs [55,87-93]. Fortunately, Ag- and Pd-based electrocatalysts, more abundant noble metals than Pt, have exhibited promising ORR activity via various modification methods, including dispersing nanoparticles evenly on functionalized support, establishing core-shell structure, and inserting other elements. Vinodh et al. [55] synthesized carbon supported silver (Ag/C) with different metal loadings via wet impregnation method. The schematic representation of cathode was illustrated in Fig. 4 (a). The characteristics of the electrocatalysts were investigated by XRD, thermogravimetric analysis (TGA), UV-visible diffuse reflectance spectra (DRS-UV), and Raman spectroscopy. The results indicated that the Ag particles in a range of 5 to 11 nm were well distributed and stable at 800^{o}C as well as the maximum cell voltage and power density of 0.69 V and 109 mW cm^{-2} were obtained with 10 wt.% metal electrocatalysts, respectively. The higher ORR activity was attributed to the larger surface area, enhanced electrical conductivities, and high densities of surface defects. Maheswari et al. [90] investigated the electrochemical kinetics of Pd/C, Pt/C, and Au/C as cathode electrocatalysts via steady-state performance test and linear sweep voltammetry (LSV). It was reported that the Pd/C showed higher performance (55 mW cm^{-2}) than Pt/C (40 mW cm^{-2}) and Au/C (1 mW cm^{-2}) with both humidified hydrogen

and oxygen fed at a rate of 500 sccm, resulting from the Pd surface exhibiting the optimum balance between the kinetics of O=O bond breaking and electrocatalytic reduction of the oxygenated intermediates or O-H formation. However, the carbon support will face two main challenges that interfere the performance of electrocatalysts. One is that carbon support may suffer from drastic corrosion and oxidation during fuel cell operation. The other is that the completion of four-electron ORR may be hindered due to the fact that the two-electron outer-sphere electron transfer is promoted. Hence, Zhang et al. [92] proposed that the graphene oxide (GO) had the potential to serve as support material due to the abundant oxygen containing functional groups that offer large surface area. Alloyed Pd-Au nanochains networks were uniformly anchored on reduced graphene oxide (Pd-Au NNs/RGO) via a one-pot wet-chemical co-reduction method with the assistance of caffeine. The results from cyclic voltammetry (CV) demonstrated that the Pd-Au NNs/RGO exhibited much more positive onset potential and half-wave potential than those achieved by using Pd black and Pd/C, indicating that the ORR activity was significantly improved. Meanwhile, it was shown from the ORR polarization curves that no obvious degradation occurred after the Pd-Au NNs/RGO modified electrode underwent 1000 times tests. It is worthy to note that there are various support materials for nanoparticles, including Ti, Ni foam, carbon nanotubes (CNTs), carbon nitride, and carbon nanofibers. Similarly, bimetallic core-shell nanostructures

possess the enhanced ORR activity, primarily due to the rough and porous surfaces. Recently, Fu et al. [93] synthesized Au@Pd core-shell nanothorns (CSNTs) via a facile co-chemical reduction method with poly(allylamine hydrochloride) (PAH) and ethylene glycol (EG) as agents at room temperature. The results from CV showed that the Au@Pd CSNTs had a positive shift of 34 mV and 30 mV of onset and half-wave potentials, respectively, compared with Pd black, demonstrating that the ORR activity was more competitive. It was concluded that the improved ORR activity could be attributed to: (1) the high electrochemically active surface area (ECSA) resulted in sufficient active sites, (2) the electron and oxygen transport was facilitated by the unique porous construction, (3) the coverage of the active sites by the hydroxyl and superhydroxyl groups was suppressed due to the core-shell structure. Inserting other elements into noble metal electrocatalysts is another way to improve the ORR performance of the alloy electrocatalysts. Generally, the 3d transition metals have been widely used as the alloying elements to promote the activity and stability of the electrocatalysts. Maheswari et al. [91] synthesized PdCo electrocatalysts in varying atomic ratios of Pd to Co, namely 1:1, 2:1, and 3:1, and investigated the structure, dispersion, electrochemical characterization and surface area of PdCo/C via XRD, TEM, and CV, respectively. It was confirmed that the alloy formation and lattice contraction existed between Pd and Co. The TEM images indicated that the nanoparticles were

crystallized and uniformly dispersed on carbon. It was also shown that when Co content in the alloy increased, the mean particle size decreased due to the increased average Pd-Pd bond distance. The results from the single fuel cell test indicated that Pd/Co (3:1) possessed higher performance (85 mW cm^{-2}) with both humidified H_2 and O_2 fed at rates of 500 sccm at atmospheric pressure than PdCo (2:1)/C (75 mW cm^{-2}), PdCo (1:1)/C (26 mW cm^{-2}) as well as Pd/C (56 mW cm^{-2}), which was attributed to the higher ORR activity and selectivity of PdCo (3:1)/C than PdCo (2:1)/C, PdCo (1:1)/C as well as Pd/C. In summary, the precious metal electrocatalysts show comparable ORR electrocatalytic activity with Pt. One of the future directions is to enhance the durability of the existing electrocatalysts, while the other is to excavate the potential precious electrocatalysts with high ORR activity.

4.2. Non-precious metals

Though the precious metal electrocatalysts catalyze the ORR efficiently, the high cost and insufficient durability shadow their future utilization. Hence, further to reduce the cost, tremendous efforts have been made to develop non-precious metal electrocatalysts [94-97]. However, the abundant 3d transition metals do not show ORR activity due to the affinities with oxygen. Fortunately, a breakthrough has been reported that metal macrocycle compounds exhibit promising ORR activity, in which the N-metal bond plays an essential role in the progress [94]. On one hand, the formidable anchoring

effect between the metal and surrounding N elevates the stability of the compounds. On the other hand, the redox potential can be relocated by the metal-N bond that serves as the bridge for the π-conjugated ligands on the outer periphery. Recently, Kruusenberg et al. [94] synthesized Co and Fe phthalocyanine electrocatalysts employing multi-walled carbon nanotubes (MWCNTs) as support materials via a simple thermal method. The results from the rotating disk electrode (RDE) tests showed that the onset potentials of CoPc/MWCNT and FePc/MWCNT electrocatalysts was -0.1 V and -0.15 V, respectively, indicating that the CoPc/MWCNT possessed high ORR electrocatalytic activity than FePc/MWCNT. The single fuel cell test demonstrated that the peak power densities were 100, 60, and 120 mW cm^{-2} with CoPc, FePc, and Pt (0.6 mg cm^{-2}) as cathode electrocatalysts and Pt (0.4 mg cm^{-2}) as anode electrocatalyst with humidified H_2 fed into the anode at a rate of 200 sccm and humidified O_2 fed into the cathode at a rate of 400 sccm at 45°C. Li et al. [95] synthesized non-precious metal electrocatalysts (denoted as CoFeN/C-H, CoFeN/C-HL, and CoFeN/C-HLH) consisting of carbon, nitrogen and transition metal via different post-treatment methods. They investigated the post-treatment methods on the performance of electrocatalysts for ORR in alkaline media via RDE technique. It was reported that the heat treatment played a crucial role in generating highly active catalytic sites. It was also shown that a peak power density of 177 mW cm^{-2} and open circuit voltage (OCV) of 0.97 V were obtained when

CoFeN/C-HLH (4 mg cm^{-2}) has been employed as cathode electrocatalyst and Pt (0.4 mg cm^{-2}) as anode electrocatalyst with humidified H_2 fed into the anode at a rate of 200 sccm and humidified O_2 fed into the cathode at a rate of 400 sccm at 50°C. While for Pt electrocatalyst, the peak power density was 196 mW cm^{-2} and the OCV was 1.04 V, showing that the CoFeN/C-HLH electrocatalyst had the possibility to replace expensive Pt. Song et al. [96] prepared carbon black based Fe-N_x/C electrocatalysts for the ORR. It was demonstrated that the activity order of different active sites is Fe-$N_{4/2}$-C > Fe_4-N-C > N-C >> Fe_4-C $\approx$ C and the one with Fe 10 wt. % and N 1.57 wt. % exhibited the best performance (107 mW cm^{-2}). In addition, the Fe-N/C electrocatalysts could be synthesized by direct pyrolysis of precursors, which was cost-efficient and batch manufacturing, giving the possibility of Fe-N/C electrocatalysts for large-scale commercial applications. He et al. [97] synthesized a new nanocomposite electrocatalyst containing high loading cobalt oxide (24.7 wt. %, Co) via incorporating CoO onto nitrogen-doped reduced GO as shown in Fig. 4 (b). They reported that a synergistic effect between rGO and CoO, resulting from the unique rGO(N)-Co(II)-O-Co(II)-rGO(N) structure, might facilitate the ORR in alkaline media and enhance the four-electron selectivity as well. Furthermore, abundant defects and nitrogen doping resulted in the accommodation of graphene-based supports for a high Co loading. The fuel cell test results showed that the performance of the CoO/rGO(N) did not exhibit

significant difference with Pt up to 400 mA cm^{-2}. While the power density of the CoO/rGO(N) experienced a large drop compared to Pt (248 mW cm^{-2} vs 387 mW cm^{-2}), which was ascribed to the relatively low electron conductivity. In conclusion, compared to precious electrocatalysts, the use of non-precious metal electrocatalysts has further reduced the cost. However, the electrocatalysts suffer severe corrosion and degradation during the fuel cell operation, especially at high current densities. Hence, the stability of the electrocatalysts in harsh environment needs to be enhanced.

4.3. Metal oxides

In recent years, great attention has been paid into a different class of metal oxides electrocatalysts so-called perovskite electrocatalysts for ORR, which are considered as alternatives to precious metal electrocatalysts due to the ORR activity and low cost [98-106]. Generally, the perovskite electrocatalysts can be denoted as $A_{1-x-y}A'_xA''_yB_{1-x-y}B'_xB''_yO_3$, in which A always represents rare-earth elements (La, Pr, and Gd) or alkaline earth metal elements (Sr and Ba) and B always refers to transition-metal elements (Mn, Co, Ni, and Fe). Suntivich et al. [98] indicated that the ORR activity of perovskite electrocatatlysts was primarily related to σ^*-orbital (e_g) occupation and the extent of B-site transition-metal-oxygen covalency, which could serve as the design principle for synthesizing perovskite electrocatalysts with promising ORR activity. The principle could be claimed that the perovskite electrocatalysts that possessed an e_g-filling (σ^*-

orbital occupation) close to 1 exhibited the highest ORR activity. Moreover, enhancing the covalency between the metal 3d and oxygen 2p orbitals also contributed to improving the ORR activity. In a recent publication by Sunarso et al. [99], the ORR activity of La-based perovskite electrocatalysts was investigated via a thin-film rotating ring-disk electrode test. The Fig. 4 (c) showed the results that $LaCrO_3$ performed largest ORR current density and most positive onset potential among the $LaMO_3$ (M=Ni, Co, Fe, Mn, and Cr). Notably, when half of the Ni in $LaNiO_3$ was substituted with Co, Fe, Mn, and Cr, a more positive shift of onset potential was observed for all the newly obtained electrocatalysts, which could be explained by the valence state change of transition-metal cation. The Koutecky-Levich analysis implied that the ORR proceeded for-electron pathway on all the perovskite electrocatalysts, which was consistent with that little hydroperoxide ion was detected during the negative scan from 0.5 V to -0.75 V. Jin et al. [100] prepared an urchin-like $La_{0.8}Sr_{0.2}MnO_3$ (LSM) perovskite oxide as electrocatalyst for both ORR and OER via a co-precipitation method with urea as a precipitator. The results from the SEM and BET analysis showed that the morphology was spherical particles with thorns radially distributed on the surface and the specific surface area was 48 $m^2 g^{-1}$. It was indicated that the four-electron pathway was dominant during ORR and a maximum cathodic current density was 5.2 mA cm^{-2} at -1.0 V vs. Ag/AgCl with 2500 rpm. Stoerzinger et al. [101] found that the (001)-oriented

$LaMnO_3$-based (LMO) perovskite films have intrinsic ORR activities comparable to those of high-surface-area LMO powder catalysts, which was attributed to (001) surface being the the activity dominant facet. When the thickness of LMO film grown on Nb-doped $SrTiO_3$ (NSTO) reduced, the ORR activity decreased. This phenomenon was explained by the barrier rooted in interfacial band bending that hindered electron transfer at the electrode-electrolyte junction and the increased e_g orbital occupancy due to the charge transfer from the NSTO to LMO. Recently, Risch et al. [102] utilized pulsed laser deposition to synthesize well-defined surfaces consisting of $Ba_{0.5}Sr_{0.5}Co_{0.8}Fe_{0.2}O_{3-\delta}$ (BSCF) on thin film $La_{0.8}Sr_{0.2}MnO_{3-\delta}$ (LSMO) grown on (001)-oriented NSTO as a bifunctional electrocatalyst. The combined overpotentials from both OER and ORR kinetics on BSCF|LSMO|NSTO could be as low as 0.7 V, which rivaled the intrinsic activities of state-of-the-art catalysts in the literature. Additionally, the surface stability of the LSMO|NSTO was promoted by the decoration of BSCF. A hybrid electrocatalyst composed of $NiCoMnO_4$ nanoparticles that were anchored on N-doped graphene nanosheets with high efficiency and low cost was proposed [103]. It was demonstrated that the $NiCoMnO_4$/N-rGO exhibited excellent ORR activity (E_{onset}= 1.5 V vs. RHE and high current density of 14 mA cm^{-2}) and catalyzed ORR mostly through four-electron process.

In summary, the unique perovskite structure provides a great flexibility to design and

497 synthesize a large amount of electrocatalysts with controlled electronic and geometric
498 structures for efficient ORR. It is believed that a near unity e_g orbital occupancy in
499 transition metal cation, closer transition metal d-band and oxygen p-band center relative
500 to the Fermi level, high covalency of the metal-oxygen bond, and oxygen deficiency
501 are favorable for the ORR activity of the perovskites. Future research direction can be
502 elucidating the active sites and the relevant ORR mechanism that are essential to
503 provide valid guidance to tune the structures of perovskite allowing enhanced O_2
504 adsorption and subsequent disassociation. In addition, the other research focus can be
505 integrating perovskite electrocatalysts with ORR-active nanocarbons to significantly
506 improve mass activity by increasing the active surface areas and enhance charge/mass
507 transport due to its low electrical conductivity [104].

508 **4.4. Non-metals**

509 A non-metal electrocatalyst, also called metal-free electrocatalyst, does not include any
510 metal element. To further reduce the cost and increase the ORR activity, considerable
511 progress has been made in the synthesis of metal-free electrocatalysts. Recently, it has
512 been reported that the carbon doped with nitrogen shows good ORR activity [107-113].
513 Higgins et al. [107] synthesized three types of nitrogen doped carbon nanotubes (N-
514 CNTs), denoted as ethylenediamine (ED-CNTs), 1,3 diaminopropane (DAP-CNTs),
515 and 1,4 diaminobutane (DAB-CNTs), via a simplistic single injection chemical vapor

516 deposition (CVD) setup. Then thin and free standing films, fabricated with the N-CNTs,
517 were tested as the ORR electrocatalyst in a single fuel cell with hydrogen and oxygen
518 both fed at a rate of 300 sccm. It was indicated that the ED-CNT film displayed the
519 significantly higher performance in alkaline media than commercial carbon supported
520 platinum (25.5 mW cm^{-2} vs 19.1 mW cm^{-2}), which was ascribed to the high extent of
521 nitrogen doping, resulting in the distinct structural properties of N-CNTs and enhanced
522 electronic properties. Similarly, Rao et al. [108] prepared nitrogen doped aligned carbon
523 nanotubes via an alumina template technique. It was depicted from microscopic images
524 that the nanotubes exhibited an outer diameter of 100 nm and length of 60 μm. The
525 OCV of the AAEMFC employing the N-CNT (5 mg cm^{-2}) as the cathode electrocatalyst
526 was ~0.87 V, which was comparable to that achieved by using the commercial Pt/C (0.5
527 mg cm^{-2}) as the cathode electrocatalyst. In addition, a peak power density of 37.3 mW
528 cm^{-2} was achieved with the humidified H_2 (95% RH, flow rate = 500 sccm) as fuel at
529 the anode and humidified O_2 (95% RH, flow rate = 1000 sccm) as oxidant at the cathode.
530 Though the performance was a little inferior in comparison to that of the AAEMFC
531 fabricated with Pt/C electrocatalyst (61.7 mW cm^{-2}), it exhibited potential to replace the
532 precious metal electrocatalysts. Ding et al. [109] proposed a novel method to synthesize
533 pyridinic- and pyrrolic-doped graphene for the ORR with the aid of layered
534 montmorillonite (MMT). A high yield of planar N that was catalytically active toward

535 the ORR was observed, as shown in Fig. 4 (d). The fuel cell fabricated with the
536 NG@MMT (4 mg cm^{-2}) as cathode electrocatalyst and Pt (0.3 mg cm^{-2}) as anode
537 electrocatalyst showed a peak power density of 320 mW cm^{-2} with hydrogen and
538 oxygen supplied to the anode and the cathode at flow rates of 150 and 200 sccm,
539 respectively. Notably, the performance, which was comparable to that of single fuel cell
540 employing commercial Pt as anode electrocatalyst (451 mW cm^{-2}), could be further
541 enhanced by reinforcing the oxygen transport. Lu et al. [113] synthesized nitrogen-
542 doped reduced graphene oxide (N-RGO) via facial treatment of grapheme employing
543 urea as agents at different temperatures. It could be seen from CV results that the N-
544 RGO based electrode showed a specific cathodic peak at -0.4 V in the presence of
545 oxygen, indicating that the N-RGO electrocatalyst possessed the excellent ORR activity.
546 In addition, it was demonstrated that the peak potential of the N-RGO was more positive
547 than the bare RGO, which means that the doped nitrogen plays an important role in
548 enhancing the ORR activity. Nevertheless, the reduction current reached the maximum
549 value when the mass ratio of urea and GRO was increased to 1:10.
550 In summary, the most attractive advantage of AAEMFCs is the absence of noble metal
551 electrocatalysts on the cathode, thereby reducing the cost. Though it has not been
552 practically realized, tremendous efforts have been made to develop substitute
553 electrocatalysts, including non-precious metal electrocatalysts, and non-metal

554 electrocatalysts for the ORR in alkaline media. The fuel cell, fabricated with Pt-based
555 anode and NG@MMT based cathode, results in the highest power density (320 mW
556 cm^{-2}). The future research direction is suggested to study the mechanisms of catalysis
557 and the structure of electrocatalysts and then to synthesize non-PGM catalysts with the
558 high ORR activity.

559 **5. Alkaline anion exchange membranes (AAEMs): Chemistries and performance**

560 Anion exchange membrane is typically composed of a polymer backbone onto which
561 fixed cationic sites are tethered. It is the cationic groups that contribute to the mobility
562 of hydroxide ions from cathode to anode through membrane. Recently, great attention
563 has been paid to the development of solid polymer electrolytes served as a thin
564 membrane of a few tens of micrometers in thickness, which alleviates the carbonate
565 problem caused by the use of alkaline aqueous electrolyte [26]. However, the carbonate
566 problem still cannot be completely eliminated, as the AAEMFCs are still sensitive to
567 the CO_2 atmosphere. Additionally, the AAEMs are also facing two more challenging
568 issues. One is to further promote the ionic conductivity, resulting in a better
569 performance. Since the diffusion coefficient of OH^- is much lower than H^+, a higher ion
570 exchange capacity (IEC) is needed so that a similar conductivity could be achieved.
571 Nevertheless, higher IEC leads to the sacrifice of mechanical properties due to the
572 excessive polymer swelling. The other is to continue to improve the stability of the

AAEMs in the harsh environment and at elevated temperatures. The polymer backbones and functional groups related to the conductivity, mechanical and chemical stability can be easily attacked by the OH^- and radicals [30]. Hence, tremendous research has been conducted on improving the conductivity as well as enhancing the thermal and chemical stability of AAEMs [114-118].

5.1. Polymer backbone

5.1.1. Poly(vinyl alcohol)

Poly(vinyl alcohol) (PVA) is a polyhydroxy polymer, which is very common in practical applications because of its easy preparation and biodegradability. Moreover, PVA shows a good chemical stability and hydrophilicity due to the hydroxyl groups. Qiao et al. and his group synthesized three types of polymer electrolyte membranes using PVA as matrix crosslinked with potassium hydroxide, poly(acrylamide-co-diallyldimethylammonium chloride), and poly(diallyldimethylammonium chloride), denoted as PVA-KOH [58], PVA–PAADDA–GA [119] and PVA/PDDA-OH^- [120,121], respectively. Analogously, all the prepared membranes exhibited excellent chemical and thermal stability, as well as good ionic conductivity. It was indicated that the hydroxide-ion conductivities of these membranes were substantially boosted from 2.75×10^{-4} S cm^{-1} to 0.02 S cm^{-1} at room temperature. Zhang et al. [115] investigated the effect of molecular weight on the performance of the membranes, which were

592 developed employing PVA as polymer matrix and poly(diallyldimethylammonium
593 chloride) (PDDA) as anion charge carriers. They claimed that PVA/PDDA-HMw
594 membrane possessed the maximum OH^- conductivity of 0.027 S cm^{-1}, the best
595 mechanical property, highest tensile strength of 15.3 MPa and tensile elongation of
596 16.8%, and excellent thermal stability, high onset degradation temperature above 170℃,
597 which was ascribed to the most compact and dense network structure. Peak power
598 densities of 35.1, 28.5, 23.4, and 18.2 mW cm^{-2} were obtained in a H_2/O_2 fuel cell
599 fabricated with Pt (0.5 mg cm^{-2}) both at anode and cathode with humidified hydrogen
600 fed at a rate of 100 sccm and humidified oxygen fed at a rate of 70 sccm at room
601 temperature employing PVA/PDDA-HMw, PVA/PDDA-MMw, PVA/PDDA-LMw,
602 and PVA/PDDA-ULMw, respectively. Merle et al. [114] fabricated AAEMs based on
603 PVA crosslinked with poly(ethylene glycol) diglycidyl ether (PEGDGE) for alkaline
604 fuel cells via simply blending the cheap materials. It was shown that the membranes
605 exhibited high long-term ionic conductivity and high chemical stability, as shown in
606 Figs. 5 (a) and 5 (b). In addtion, a maximum power density of 72 mW cm^{-2} was achieved
607 in an alkaline fuel cell fabricated with Pt (4 mg cm^{-2}) both at anode and cathode
608 employing PVA membrane with 15 wt. % acrylic acid, which was the only candidate
609 for the application due to the denser structure with hydrogen (RH=100%) supplied at a
610 flow rate of 40 sccm and oxygen supplied at a flow rate of 80 sccm. Lu et al. [122]

611 synthesized PVA-poly(vinylbenzyl chloride) (PVBC) membrane with a
612 macromolecular crosslinker, in which PVBC acted as conducting polymers and PVAc
613 containing dimethylamino groups worked as crosslinker and the supporting matrix
614 simultaneously. The results from Fourier transform infrared (FT-IR) and XPS showed
615 that the PVBC and PVAc were crosslinked successfully. In addition, it was indicated
616 that hydroxide-ion conductivity was larger than 0.01 S cm^{-1} at room temperature and
617 swelling ratio (SR) was suppressed when the temperature was elevated. A peak power
618 density of 124.7 mW cm^{-2} was obtained in an AAEMFC fabricated with Pt (0.4 mg cm^{-2})
619 both at anode and cathode employing the crosslinked membrane with hydrogen
620 (RH=100%) supplied at a flow rate of 40 sccm and oxygen supplied at a flow rate of
621 70 sccm at 40°C.

622 **5.1.2. Poly(arylene ether)s**

623 Poly(arylene ether)s possesses excellent stability and water resistance that are
624 preferable properties of AAEMs. Thus, some AAEMs based on poly(arylene ether)s
625 have been reported [116,117,123]. Tanaka et al. [123] synthesized aromatic multiblock
626 copolymer membrane, poly(arylene ether)s containing quaternized ammonio-
627 substituted fluorene groups, via block copolycondensation of fluorene-containing
628 hydrophilic oligomers and linear hydrophobic oligomers, chloromethylation,
629 quaternization, and ion-exchange reactions. It was reported that this membrane

630 exhibited considerably high hydroxide-ion conductivities, reaching 144 mS cm^{-1} at
631 80°C, and retained the high conductivity for 5000 h. They claimed that introducing
632 highly ionized hydrophilic blocks into multi-block structure was an efficient way to
633 promote the ionic conductivity. Jasti et al. [116] proposed a facial synthesis of aminated
634 multiblock poly(arylene ether)s with hydrophilic blocks via nucleophilic substitution
635 poly condensation followed by quaternization and alkalization reactions. It was shown
636 that hydrophilic/hydrophobic phase separation due to the interconnected ion transport
637 pathway, resulting in a high ionic conductivity of 150 mS cm^{-1} at 80°C. In the presence
638 of two vicinal quaternary ammonium groups, the membrane exhibited promising
639 alkaline stability, because nucleophilic attack was hindered, as well as the degradation
640 was avoided. Li et al. [117] prepared functionalized quaternary ammonium
641 poly(arylene ether)s (QBMPAEs) containing tetramethyl triphenyl methane moieties
642 via polycondensation, benzylic bromination, quaternization, and alkalization. It was
643 demonstrated that the IECs could be adjusted from 0.90 to 1.73 mmol g^{-1} by controlling
644 the conditions of the bromination reaction. In addition, the water uptake (WU) and SRs
645 of the QBMPAEs membranes were moderate and could be adjusted by controlling their
646 degree of bromination (DBM) values. One of the synthesized membranes, QBMPAE-d
647 membrane, possessed excellent long-term alkaline stability for 30 days. It was indicated
648 that the QBMPAE-d membrane resulted in the highest conductivity of 46.6 mS cm^{-1} at

649 80ºC and a peak power density of 20.1 mW cm^{-2} was achieved in a H_2/air single fuel
650 cell with hydrogen (RH=100%) supplied at a flow rate of 300 sccm and air supplied at
651 a flow rate of 800 sccm along with 0.1 mg cm^{-2} Pt on the anode and 0.2 mg cm^{-2} Pt on
652 the cathode at 70ºC.

653 **5.1.3. Poly(2,6-dimethyl-1,4-phenyleneoxide)**

654 Poly(2,6-dimethyl-1,4-phenyleneoxide) (PPO) has outstanding physical properties,
655 including high dimensional stability, excellent mechanical properties, high thermal
656 stability, low moisture uptake, low flammability, and exceptional electrical properties,
657 including a low dielectric constant and a low dielectric dissipation factor. Moreover,
658 another superiority of PPO is the safety. The toxicity of many other materials has
659 restricted their development for AAEMFC applications. In view of these characteristics,
660 PPO has been regarded as an excellent candidate for high-frequency substrates. Ong et
661 al. [124] synthesized PPO based membranes via bromination/amination serial reactions,
662 which reduced the number of involved toxic chemicals and reaction time. Though the
663 synthesis route was relatively simple, the obtained membrane, prepared from 5 wt%
664 PPO, bromine/PPO molar ratio at 10, nitrogen-free atmosphere, with hydroxylation
665 treatment and N-methyl-2-pyrrolidone (NMP) as the membrane casting solvent,
666 possessed competitive ionic conductivity of 1.64×10^{-2} S cm^{-1} at 60℃. The peak power
667 density increased from 3 mW cm^{-2} to 19.5 mW cm^{-2} with the temperature going up from

25°C to 70°C with hydrogen (RH=100%) supplied at a flow rate of 5 sccm and oxygen supplied at a flow rate of 10 sccm along with Pt (0.65 mg cm^{-2}) both at anode and cathode. Further increasing the temperature, a dramatic degradation occurred primarily due to the thermal degradation of AAEM. Lin et al. prepared PPO based AAEMs containing pendant guanidinium groups [125], benzimidazolium (BIm) groups [126], and 1,2-dimethylimidazolium (DIm) functional groups [127], denoted as GPPO, BImPPO, and DImPPO, respectively. It was indicated that the GPPO membrane possessed high anion conductivities resulting from the high basicity of guanidinium groups, and short-term thermal and long-term alkali stabilities due to the π electron conjugated system. Meanwhile, a peak power density of 16 mW cm^{-2} was achieved at 50°C when the GPPO membrane was fabricated into a H_2/O_2 fuel cell utilizing Pt (0.4 mg cm^{-2}) both at anode and cathode with both humidified hydrogen and oxygen fed at rates of 600 sccm. In comparison with the analogous PPO membranes containing the classical pendant quaternary ammonium and imidazolium cations, the BImPPO membrane showed advantages in ionic conductivity, dimensional, thermal, and mechanical stabilities. Furthermore, the peak power density was 13 mW cm^{-2} at 35°C in the case of the utilization of optimal BIm-PPO-0.54 AAEM. In addition, the DImPPO membrane also exhibited comparative conductivity, in the ranges of 10-40 mS cm^{-1} and 18-75 mS cm^{-1} at 30°C and 60°C, respectively. Nevertheless, the power density

employing DImPPO membrane was much higher than that of other PPO membrane, reaching 56 mW cm^{-2}, whereas it decreased dramatically to 31 mW cm^{-2} after three-time repetition of the test, suggesting the poorer stability. Li et al. [128] synthesized quaternized PPOs materials containing clicked 1,2,3-triazoles for AAEMs via Cu^{I}-catalyzed "click chemistry". It was shown that the obtained membranes possessed higher WU, hydroxide-ion diffusion coefficient and anion conductivities due to the formation of efficient and continuous hydrogen-bond networks. A hydroxide-ion conductivity of 27.8-62 mS cm^{-1} was achieved at 20°C in water, which was several times higher than that of a typical PPO-based AAEM (TMA-20). An improved peak power density of 188.7 mW cm^{-2} was obtained in a H_2/O_2 fuel cell fabricated with Pt (0.5 mg cm^{-2}) both at anode and cathode with hydrogen (RH=100%) supplied at a flow rate of 200 sccm and oxygen supplied at a flow rate of 200 sccm at 50°C employing the membrane with alkyne-functionalized quaternary ammonium (QA). A recent publication by Dang et al. [129] demonstrated that the position of QA cations in the polymer structure, ring size, the presence of an additional heteroatom, and ring substitution pattern played a crucial role in the performance of the PPO based AAEMs. The results are beneficial for selecting optimal QA groups to enhance the lifetime and performance of the AAEMs. Wang et al. [130] proposed a strategy of supramolecular modalities for strengthening the mechanical stability of the PPO based AAEMs

substantially. A secondary amide was introduced into the AAEMs to serve as a hydrogen-bonding crosslinking motif, which was evidenced by the 101% elongation at break, whereas the AAEMs without hydrogen-bonding crosslinking showed the elongation at break in the range of 10%~20%.

5.1.4. Poly(tetrafluoroethylene)

Poly(tetrafluoroethylene) (PTFE) has been widely used in chemical industry and other related industries due to its unique properties, which can be conclude as follows: (1) high chemical stability; (2) excellent thermal stability; (3) minimal water absorption; and (4) no toxicity. Due to the high thermal and chemical stability, as well as low WU, PTFE has been introduced to synthesize AAEMs [61,131-134]. Wang et al. [61] synthesized a thin (30 μm) composite membrane by impregnating quaternary 1,4-diazabicyclo-[2.2.2]-octane polysulfone (QDPSU) solution in PTFE. The results from the scanning electron microscope (SEM) exhibited that the obtained membrane possessed a dense and homogenous structure. It was shown that the composite membrane exhibited better mechanical strength (a 32 MPa maximum load), lower WU (61 ± 3%) and less swelling degree (17 ± 2%) than pristine QDPSU membrane. Furthermore, a considerable peak power density of 146 and 103 mW cm^{-2} were achieved with Pt (0.5 mg cm^{-2}) both at anode and cathode along with hydrogen (80 sccm, RH=100%) and oxygen or air (100 sccm, RH=100%) as oxidant, respectively.

Zhao et al. reported that the quaternized polyvinyl benzyl chloride (QPVBC) could provide sufficient ionic exchange group, but it became brittle after casting membrane [132]. Hence, they prepared quaternary ammonia polysulfone (QAPS)/PTFE composite membrane by employing porous PTFE membrane as the substrate and QAPS polymer as the anionic conductor [133]. It was indicated that the obtained membrane possessed better mechanical strength, lower SR and WU than the previous QAPS alkaline AAEM. The fuel cell fabricated with the 20 μm thickness membrane and Pt (0.4 mg cm^{-2}) both at anode and cathode with hydrogen (RH=100%) supplied at a flow rate of 100 sccm and oxygen supplied at a flow rate of 200 sccm resulted in a peak power density of 315 mW cm^{-2} at 50°C. Nevertheless, the QAPS was inclined to leach out gradually during the operation of the fuel cell, resulting from the poor interaction between the QAPS guest and the PTFE host. As consequence, Li et al. [134] proposed a new approach for making ultrathin composite membranes of alkaline polymer electrolytes (APEs), which could avoid the leach out problem. They impregnated the APE ionomer TQAPS into a porous PTFE film, followed by a self-crosslinking process, forming a semi-interpenetrating network. It was indicated that the obtained membrane (xQAPS@PTFE, 25 μm thick) showed low area resistance (0.09 Ω cm^2), a low swelling degree (3.1% at 60°C) and high mechanical strength (31 MPa). A peak power density of 550 mW cm^{-2} was achieved in a H_2/O_2 AAEMFC fabricated with Pt (0.4 mg cm^{-2}) both at anode and

744 cathode employing the membrane with both humidified hydrogen and oxygen fed at
745 rates of 120 sccm at 60ºC.

746 **5.1.5. Polysulfones**

747 Poly(arylene ether sulfone) exhibits promising mechanical and thermal stability, as well
748 as hydrolysis resistance. Recently, some attempts have been made to the synthesis of
749 membranes based on poly(arylene ether sulfone) [135-137]. Zhou et al. [135] prepared
750 the poly(arylene ether sulfone) based membranes, containing fluorenyl groups
751 (QAPSF), functionalized with benzyltrimethylammonium groups via the
752 polycondensation, chloromethylation, and amination reactions. It was reported that the
753 QAPSF membranes were stable at pH 11 and showed slow degradation at pH>14. A
754 peak power density of 4.1 mW cm^{-2} was obtained in an AAEMFC fabricated with Pt (1
755 mg cm^{-2}) both at anode and cathode operating on H_2 (6 sccm, RH=100%) supplied to
756 anode and O_2 (3 sccm, RH=100%) and CO_2 (6 sccm, RH=100%) supplied to cathode.
757 Surprisingly, the addition of CO_2 resulted in a promotion of power density, from 2.2 to
758 3.2 mW cm^{-2}, because CO_2 was involved in the chemical progress and transported
759 through the AAEM. Yang et al. [136] synthesized a series of poly(arylene ether sulfone)
760 containing bulky imidazole groups (PSf-Im-x) based on a novel monomer 2,2'-bis-(2-
761 ethyl-4-methyl-imidazole-1-ylmethyl)-biphenyl-4,4'-diol (EMIPO), followed
762 quaternization by n-bromobutane. The attached bulky groups around the imidazolium

763 ring reduced the access of OH^- to imidazolium, which leaded to the enhancement of
764 alkaline stability, showing an OH^- conductivity of 0.014 S cm^{-1} at 30℃ and retaining
765 the 80% of the conductivity for 144 h. It was revealed that some inorganic materials
766 could be added into polymer matrix, improving the mechanical, thermal and chemical
767 properties. Li et al. [137] synthesized a series of cross-linked multiblock copoly(arylene
768 ether sulfone) ionomer (CLQCPAES)/nano-ZrO_2 composite AAEMs via block
769 copolymerization, bromomethylation, ultrasonication blending, self-crosslinking,
770 quaternization, and alkalization. It was shown that the CLQCPAES/nano-ZrO_2
771 composite membranes were complex cross-linking networks of hydrophobic
772 domains/hydrophilic domains/nano-ZrO_2 with a clear zonal distribution of uniform
773 nano-sized particles in the hydrophilic domains. The WU, mechanical properties,
774 hydroxide conductivity, and alkaline stability were enhanced significantly by the
775 modification with block-ionomer structure, cross-link treatment and the introduction of
776 nano-ZrO_2 particles. Particularly, the CLQCPAES/7.5% ZrO_2 membrane showed an
777 IEC value of 1.23 mmol g^{-1}, hydroxide-ion conductivity of 55.2 mS cm^{-1} at 80ºC, and
778 tensile strength of 32.0 MPa, which possessed almost the best comprehensive properties.
779 Polysulfone membrane exhibits prime mechanical, biological, and chemical stability,
780 and has a wide operating range at temperature (>80°C), which attracts worldwide
781 attentions. Zhang et al. [138] prepared a porous polysulfone AAEM filled with (3-

782 acrylamidopropyl)trimethylammonium chloride and N,N'-methylenebisacrylamide
783 with a grid-plug microstructure via phase-inversion, interfacial diffusion, and in-situ
784 polymerization. It was indicated that the PSU-PATC(1.2) membrane with optimal
785 content of PATC performed best (55 mW cm^{-2}) in a single fuel cell fabricated with Pt
786 (2 mg cm^{-2}) both at anode and cathode with H_2 (800 sccm, RH=100%) supplied to
787 anode and O_2 (600 sccm, RH=100%) supplied to cathode due to the maximum ionic
788 conductivity. He et al. [139] suggested that one of the obstacles for the application of
789 AAEMs was the poor ionic conductivity, which was partially attributed to the poorly-
790 defined morphologies of AAEMs, resulting in the tortuous ion transport pathways. As
791 a consequence, they proposed a novel strategy, grafting hydrophilic poly(ethylene
792 glycol) side-chains along a model benzyltrimethylammonium polysulfone-based
793 AAEM to form nanoscale (5 to 10 nm diameter) anion transport channels, to enhance
794 the ionic conductivities of AAEM. It was indicated that the IEC-normalized hydroxide
795 conductivity increased by 100% from 20.2 to 40.3 mS g cm^{-1} $mmol^{-1}$ and the power
796 density increased by 50% from 118 mW cm^{-2} to 180 mW cm^{-2} in a fuel cell fabricated
797 with Pt (0.5 mg cm^{-2}) at anode and Pt (2 mg cm^{-2}) at cathode with humidified H_2
798 supplied to anode at a flow rate at 150 sccm and humidified O_2 supplied to cathode at
799 a flow rate at 200 sccm, simultaneously. Vinodh et al. [140] synthesized a quaternized
800 polysulfone/ZrO_2 composite membrane via solution casting method and determined its

characteristic properties via XRD, TGA, and electrochemical impedance spectroscopy (EIS). The results from the tests indicated that the ZrO_2 nano fillers were distributed homogeneously, showing no obvious agglomeration. In addition, the composite membrane exhibited long-term thermal and chemical stability. Typically, a peak power density of 250 mW cm^{-2} was obtained in a single H_2/O_2 fuel cell fabricated with Pt (0.375 mg cm^{-2}) at anode and Pt (0.125 mg cm^{-2}) at cathode at 60°C as the QPSU/10% ZrO_2 has been employed.

5.2. Functional groups

5.2.1. Quaternary ammonium (QA)

QA groups are more thermally and chemically stable than tertiary ammonium (TA) and primary ammonium (PA), resulting in the most common utilization of quaternary ammonium as hydroxide ions transfer carriers. Varcoe et al. [141] developed a novel alkaline polymer, employing N,N,N',N'-tetramethylhexane-1,6-diamine as the cross-linking agent and poly-(vinylbenzyl chloride) as the polymer backbone. After the treatment of KOH exchange, the obtained polymer was coated on the electrodes working as the AAEM, which not only increased the power density of a single fuel cell using Pt (0.5 mg cm^{-2}) both at anode and cathode with H_2 (2000 sccm, RH=100%) fed to anode and O_2 (2000 sccm, RH=100%) fed to cathode from 1.6 to 55 mW cm^{-2} at 50°C, but also avoided undesirable carbonate precipitation. Pan et al. [142] replaced a

820 part of the QA in QAPS with a TA, and the two substances crosslinked two nearest
821 neighboring chains generating xTQAPS membrane upon solidification. It was found
822 that the self-crosslinked membrane did not show any obvious degradation of
823 mechanical stability and IEC in pure water at 90^{o}C for 500h, which suggested the
824 membrane exhibited extraordinary both physical and chemical stability, breaking the
825 contradiction between the IEC and dimensional stability. This phenomenon could be
826 attributed to the stereo-hindrance effect of the two benzyl groups in proximity
827 suppressing the Hofmann elimination reaction. Zhou et al. [143] prepared AAEMs with
828 varying amounts of QA groups (0.51, 0.70, and 0.90 mmol g^{-1}) grafted onto a SEBS
829 block copolymer and investigated the impacts of AAEMs with various IECs on the
830 performance of H_2/O_2 fuel cells. The peak power density of the AAEMFCs utilizing Pt
831 (0.5 mg cm^{-2}) both at anode and cathode with H_2 (200 sccm, RH=100%) supplied to
832 anode and O_2 (200 sccm, RH=100%) supplied to cathode employing these AAEMs with
833 IEC of 0.51, 0.70, and 0.90 mmol g^{-1} were 169, 222, and 285 mW cm^{-2}, respectively. It
834 was indicated that a higher content of QA groups in the membranes leaded to higher
835 ionic conductivity, resulting in the lower overpotential and higher power density. They
836 revealed that the transportation resistance of the OH^- ions was a controlling factor when
837 fewer functional groups were contained in the membrane or the cell voltage was higher.
838 Li et al. [144] reported highly stable, anion conductive and comb-shaped copolymers

containing long alkyl side chains pendant to the nitrogen-centered cation via a Menshutkin reaction to form comb-shaped structures. It showed that the membrane with long alkyl chain of up to 16 carbon atoms, which had the longest hexadecyl chain, exhibited higher hydroxide-ion conductivity, more distinct ionic domains, and lower WU than that with a hexyl side chain. The peak power density of fuel cell fabricated with Pt (0.5 mg cm^{-2}) both at anode and cathode using both humidified H_2 O_2 fed at flow rates at 200 sccm with C16D40 membrane was 77 mW cm^{-2}, which was slightly higher than that using C6D60 (67 mW cm^{-2}). Increasing the flow rates of hydrogen and oxygen, the peak power density of C6D60 could reach 145 mW cm^{-2} when the flow rates of anode and cathode were both at 2000 sccm. However, the C16 membrane was inferior in the film-forming ability due to the poor compatibility between long alkyl side chain and polymer backbone. Ren et al. [145] reported highly conductive AAEM with styrenic diblock copolymer, a quaternary ammonium-functionalized hydrophilic block and a cross-linkable hydrophobic block, which possessed high ionic conductivity at 98 mS cm^{-1} and controlled membrane swelling with WU at 117 wt. % at 22°C. It was ascribed to the reduced tortuosity of the ionic conduction pathways. Moreover, excessive WU was suppressed because the mechanical integrity of the membrane was maintained due to the hydrophobic network. A peak power density of 168 mW cm^{-2} was obtained in a H_2/air fuel cell fabricated with Pt (1 mg cm^{-2}) both at anode and cathode

858 using newly developed AAEM (C30D70-1.7) with H_2 (250 sccm, RH=95%) supplied
859 to anode and air (250 sccm, RH=95%) supplied to cathode at 50ºC.

860 **5.2.2. Imidazolium**

861 Though the QA groups are more thermally and chemically stable than TA and PA groups,
862 the AAEMs with QA groups are still facing the facile degradation and excessive
863 swelling problems. Hence, a resurgence of exploring substituted functional groups has
864 occurred. Imidazolium salts (IMSs) are well-known as a type of ionic liquid, which can
865 act as electrolytes due to their high chemical stability and low vapor pressure. It seems
866 that imidazolium chemistry is more amenable to AAEM fabrication through post-
867 functionalization, resulting in the formation of ion clusters for efficient transport of OH^-.
868 Recently, Lu et al. [146] synthesized imidazolium-functionalized AAEMs via
869 functionalization of chloromethylated poly(ether sulfone) (PES) with 1-alkylimidazole.
870 It was revealed that the WU, SR and solubility of AAEMs increased but the OH^-
871 conductivity decreased with the increment of the alkyl line length on the imidazolium
872 group. They claimed that the ionic conductivity was determined by the ionic
873 concentration, which was affected by IEC and SR. Accordingly, the quotient of IEC
874 divided by SR (IEC/SR) could be regarded as an indirect indicator of the ionic
875 concentration. Moreover, a peak power density of ~30 mW cm^{-2} was obtained in a
876 H_2/O_2 AAEMFC fabricated with Pt (0.4 mg cm^{-2}) both at anode and cathode employing

877 the fabricated AAEM and anion exchange ionomers (AEIs) with H_2 (50 sccm,
878 RH=100%) supplied to anode and air (100 sccm, RH=100%) supplied to cathode at
879 45°C. Zhang et al. [147] reported a polysulfone-imidazolium AAEM (PSf-ImOH) via
880 functionalization of chloromethylated polysulfone with methylimidazole, added
881 different degrees of chloromethylation of PSf to control the membrane properties. They
882 found that the membranes possessed comparable IEC, conductivity, and thermal
883 stability with the conventional AAEMs. In spite of the low power density (16 mW cm^{-2}),
884 a new route for non-QA AAEM design and fabrication was offered. Ran et al. [148]
885 developed imidazolium-type AAEMs (Im-AAEM) based on bromomethylated
886 poly(2,6-dimethyl-1,4-phenyleneoxide) (BPPO) polymer chains via solution casting of
887 NMP solutions. Additionally, a favorable conductivity up to 100 mS cm^{-1} was obtained
888 at 80°C, resulting from the nano-scale phase-separated construction by the solution
889 casting method. It was indicated that different IECs ranging from 1.1 to 2.4 mmol g^{-1}
890 could be obtained by tuning the molar ratio of 1-methylimidazole to CH_2Br groups in
891 the starting polymer. A peak power density of 30 mW cm^{-2} was achieved in a single fuel
892 cell using Pt (0.5 mg cm^{-2}) both at anode and cathode with Im-AAEM with both
893 humidified hydrogen and air fed at flow rates of 600 sccm at 50°C.

894 **5.3. Other chemistries**

895 In addition to the above-mentioned AAEMs, extensive other types of AAEMs based on

various materials have been synthesized and reported [149-163]. Xing et al. [149] found that the conductivity of KOH-doped polybenzimidazole (PBI) was remarkable, reaching to 9×10^{-2} S cm^{-1} at 25ºC, which was much higher than that of preciously obtained on acid-doped PBI. In addition, the H_2/O_2 fuel cell using this polymer electrolyte exhibited the same performance as those based on Nafion 117 membrane. Li et al. [150] reported that grafting long side-chain cations onto PBI was an effective way to improve the OH^- conductivity, mechanical and thermal stability, as well as reduce swelling ratio. Wan et al. [151] synthesized different solid polymer electrolyte membranes using chitosan as matrices incorporated with potassium hydroxide as ionic carrier. After hydration for 1 h, the conductivity of the membrane was about 10 mS cm^{-1}. When being integrated into the fuel cells, the maximum current density reached 35 mA cm^{-2} and the open circuit voltage of 1 V was achieved. Additionally, they also proposed two approaches to improve the fuel cell performance [152]. One was to add an alkaline and ionic-conductive interfacial gel, and the other was to decrease the thickness of the membrane. Luo et al. [153] synthesized a novel high molecular weight copolymer quaternized poly(methyl methacrylate-co-butyl acrylate-co-vinyl benzylchloride) (denoted as QPMBV) composed of methyl methacrylate (MMA), butyl acrylate (BA), and VBC. It was reported that polymer electrolytes could be designed bottom-up through mini-emulsion polymerization by selecting desirable monomer

915 [154]. Furthermore, the conductivity reached 8.2 mS cm^{-1} at 80°C. The results from the
916 fuel cell performance evaluation demonstrated that the peak power density of 25 mW
917 cm^{-2} was achieved in a single fuel cell fabricated with Pt (0.5 mg cm^{-2}) both at anode
918 and cathode with H_2 (80 sccm, RH=80%) supplied to anode and air (80 sccm, RH=80%)
919 supplied to cathode at 60°C, suggesting that the preparation concept of these
920 membranes was feasible [155]. Moreover, the conductivity and the mechanical strength
921 were balanced by utilizing the designed hydrophobic and hydrophilic segments [154].
922 Hence, they concluded the membrane properties as follows [156]: (1) higher molecular
923 weight resulted in the improvement of the mechanical strength as well as reduction of
924 the WU; (2) higher concentration of the conductive sites resulted in the enhancement
925 of conductivity but simultaneously impairment of the mechanical properties; (3) higher
926 glass transition temperature resulted in the promotion of the membrane durability; and
927 (4) the water hydrophilicity of the mechanical support played an important role in the
928 WU. Wu et al. [157] prepared a high ion-conduction alkaline membrane by sulfonation
929 with lower cost using non-woven polypropylene/polyethylene (PP/PE). It was shown
930 that the ionic conductivity was improved from 8.8 to 17.5 mS cm^{-1}, while the decline
931 of thermal resistance (4%) and mechanical strength (21%) was reduced. Sollogoub et
932 al. [158] developed an AAEM using a poly(epichlorhydrin) as matrix and incorporated
933 two cyclic diamines, namely 1,4-diazabicyclo-[2,2,2]-octane (DABCO) and 1-

934 azabicyclo-[2,2,2]-octane (Quinuclidine), into the matrix to ensure anionic conduction
935 properties. They illustrated that the transport number is usually 0.99 and the peak power
936 density was nearly 100 mW cm^{-2} when the membrane was assembled in a H_2/O_2 fuel
937 cell utilizing Pt (0.17 mg cm^{-2}) as both anode and cathode electrocatalysts. Hibino et al.
938 [159] developed a series of hydroxide-ion conducting antimony (V)-doped Tin
939 pyrophosphate electrolyte, $Sn_{1-x}A_xP_2O_7$ (A=V, Nb, Ta, and Sb) compounds, for
940 intermediate-temperature alkaline fuel cells. It was indicated that $Sn_{0.92}Sb_{0.08}P_2O_7$
941 exhibited the highest electrical conductivity in the temperature range of 50-200°C.
942 Additionally, the peak power densities of 76 mW cm^{-2}, 94 mW cm^{-2}, 114 mW cm^{-2}, 130
943 mW cm^{-2}, 132 mW cm^{-2} and 147 mW cm^{-2} were obtained with Pt (2 mg cm^{-2}) both at
944 anode and cathode and humidified hydrogen and air at rates of 50 sccm at 75°C, 100°C,
945 125°C, 150°C, 175°C, and 200°C, respectively [160]. Zhao et al. [161] reported a series
946 of pore-filled AAEMs via thermal polymerization of chloromethyl monomer in a
947 porous PE substrate followed by amination with trimethylamine. It was indicated that
948 a hydroxide conductivity of 0.057 S cm^{-1} was obtained at 30°C, in deionized water and
949 the synthesized membrane possessed long term alkaline stability. A peak power density
950 of 370 mW cm^{-2} was achieved in a H_2/O_2 fuel cell utilizing Pt (0.5 mg cm^{-2}) both at
951 anode and cathode with hydrogen (100 sccm, RH=100%) fed to anode and oxygen (200
952 sccm, RH=100%) fed to cathode at 50°C. Kim et al. [162] fabricated

953 pentamethylguanidinium functionalized perfluorinated hydroxide-ion conducting
954 ionomers for AAEM. It was shown that the alkaline stability of the ionomers largely
955 depended on the adjacent group that connected the cation. Meanwhile, the
956 phenylguanidinium functionalized ionomer exhibited better stability than sulfone
957 guanidinium functionalized ionomer due to the charge delocalization of the formed
958 resonance structure. When the membrane was fabricated into a H_2/O_2 fuel cell using Pt
959 (3.4 mg cm^{-2}) on the anode and Pt (6.5 mg cm^{-2}) on the cathode with supplied
960 humidified hydrogen and oxygen, a peak power density of 577 mW cm^{-2} was obtained.
961 Recently, Chen et al. [163] found that both introducing ionic liquids and adding nano-
962 TiO_2 into the AAEMs contributed to improving the OH^- conductivity. The ionic liquids
963 dispersed in the membrane functioned active sites for secondary OH^- conduction, and
964 the nano-TiO_2 particles could significantly alleviate the ionic liquid loss and stabilize
965 the ionic liquid monomer in the membrane.
966 The effects of the cations chemistries, the length of alkyl chain of the diamines, the
967 reaction conditions of chloromethylation, and the parameters of polymers on the
968 AAEMs have been extensively investigated [164-169]. Einsla et al. [164] tested the
969 stability of cations for anion exchange membrane fuel cells and illustrated that the
970 stability of benzyltrimethylammonium hydroxides was much better than that of
971 phenyltrimethylammonium hydroxides under similar conditions. Furthermore, they

showed the degradation of stability of the cation when the concentration of the ammonium hydroxides was increased. Arges et al. [165] studied the influence of different cation chemistries, 1,4-dimethylpiperazinium (DMP+), trimethylammonium (TMA+), and trimethylphosphonium (TMP+), on ionic conductivity and alkaline stability of AAEMs. They concluded from the obtained experimental evidence as follows: (1) phosphonium cations with similar or greater basicity degraded more rapidly than ammonium cations; (2) phosphonium cations degraded through a fundamentally different mechanism (ylide formation) than ammonium cations (direct nucleophilic substitution); (3) as long as the issue of significant WU did not come into play, the fuel cell performance was enhanced with higher IEC AAEMs. Park et al. [166] investigated the effect of the length of alkyl chain of the diamines on ionic conductivity and thermal characteristics via employing TMA as a monoamine and N,N,N',N'-tetramethylmethanediamine (TMMDA), N,N,N',N'-tetramethylethylenediamine (TMEDA), N,N,N',N'-tetramethyl-1,3-propandiamine (TMPDA), N,N,N',N'-tetramethyl-1,4-butanediamine (TMBDA) and N,N,N',N'-tetramethyl-1,6-hexanediamine (TMHDA) as various diamines. The results showed that the mixture of TMA and TMHDA had a better hydroxyl ion conductivity and thermal stability than others, suggesting that a longer alkyl chain resulted in higher performance. Wang et al. [167] demonstrated that the parameters, including reaction time, reaction temperature,

991 concentration of polymer, concentration of chloromethylation agent, and the amount of
992 catalyst, possessed significant impacts on chloromethylation. When these parameters
993 were well controlled, the gelation could be avoided. Among the parameters, the
994 concentration of the chloromethylation agent played a dominant role in enhancing the
995 attachment of chloromethyl functional group onto the polymer. Luo et al. [168]
996 investigated the effects of polymer composition drift, molecular weight, and polymer
997 crosslinking on the properties of quaternized poly(methylmethacrylate-co-vinylbenzyl
998 chloride) (QPMV)-based AAEM. It was indicated that the initial monomer ratio and the
999 resulted copolymer composition could influence the hydrophobic/hydrophilic portions
1000 in the membrane. They demonstrated that decreasing initiator potassium persulfate
1001 (KPS) and increasing surfactant sodium dodecyl sulfate (SDS) could increase the
1002 molecular weight, simultaneously improving the mechanical properties. It was believed
1003 that crosslinking method could alleviate the WU problem due to the less distinct phase
1004 separation feature. Pan et al. [169] proposed two strategies for developing advanced
1005 APEs which were highly resistant to swelling and showed conductivities comparable
1006 with Nafion: self-crosslinking and self-aggregating designs. It was indicated that a
1007 short-range cross-linker, tertiary amino groups, was grafted onto the QAPS and the
1008 membrane swelled by less than 3% at 80^{o}C. In self-aggregating design, long alkyl side-
1009 chains were attached to the QAPS, which produced enlarged and aggregated ionic

channels.

5.4. AAEM performance

5.4.1. Effect of pre-treatment

Before being integrated into the fuel cell, the membrane would be immersed into water or alkaline electrolyte to improve the conductivity. Under pure water operation, the characterization of membrane has been extensively conducted [170,171]. Li et al. [170] prepared AAEMs with significant ionic conductivities over the order of 10^{-2} S cm^{-1} in DI water at room temperature. The fuel cell using Pt (0.5 mg cm^{-2}) both at anode and cathode yielded an OCV of 1.028 V and a peak power density of 33 mW cm^{-2} with hydrogen (50 sccm, RH=100%) supplied on the anode and oxygen (100 sccm, RH=100%) supplied on the cathode in the absence of liquid electrolyte, such as KOH and NaOH, at 30°C, suggesting the possibility of the membrane for AAEMFCs application. Mamlouk et al. [171] studied the effect of anion functional groups on the conductivity and performance of AAEMs. It showed that TMA functionalized membrane possessed the highest conductivity among amine/sulphide-based functional groups with conductivities values up to 0.25 and 0.043 S cm^{-1} in plane and through plane, respectively. The highest power density of 478 mW cm^{-2} was achieved when TMA functionalized electrodes fabricated with Pt (0.4 mg cm^{-2}) were employed, followed by the second highest power density of 236 mW cm^{-2} achieved by the

1029 TMHDA electrodes. Trimethylamine (TEA) and DABCO electrodes showed analogous
1030 power densities of 100 and 116 mW cm^{-2}, respectively. Finally, the dimethyl sulfide
1031 (DMS) functionalized electrodes performed the lowest power density of 58 mW cm^{-2}.
1032 As a consequence, it was demonstrated that the ionomer functional groups affected the
1033 oxygen permeability, the activation energy and the exchange current density for oxygen
1034 reduction and anode flooding. Thus, the type of functional groups used for the ionomer
1035 can severely restrict cell performance.
1036 When the pure water changes to alkaline electrolyte, the performance has also been
1037 studied [58,119,121]. Fu et al. [58] demonstrated that the ionic conductivity of the
1038 membrane was promoted to 0.473 mS cm^{-1} after alkali (2-4 M) doping due to the KOH
1039 penetrated into the polymer. However, there was no significant contribution to the
1040 conductivity when the concentration of the KOH was larger than 4 M, which was
1041 attributed to the weak ionic mobility. Similarly, Zhang et al. [121] found that the
1042 conductivity of the AAEM reached to a maximum value of 0.025 S cm^{-1} after the KOH
1043 (2 M) doping. Qiao et al. [119] claimed that this phenomenon could be explained by
1044 the two following reasons: one was that the QA groups would decompose in such harsh
1045 basic environment, and the other was that the ionic mobility became weak due to the
1046 increase of the viscosity or the formation of ion-pairs. Jiang et al. [172] designed an air-
1047 breathing cell for fast screening of electrolytes as shown in Figs. 6 (a) and 6 (b), which

1048 was suitable for using various liquid electrolytes, thus reproducible data could be
1049 obtained. Subsequently, the effects of different electrolytes, i.e. 1.0 M
1050 tetramethylammonium hydroxide (TMAOH), 1.0 M tetraethylammonium hydroxide
1051 (TEAOH), 1.0 M tetrapropylammonium hydroxide (TPrAOH), 1.0 M KOH, and 0.5 M
1052 H_2SO_4, on the performance of fuel cells were investigated. First, the inorganic
1053 electrolytes were evaluated at various temperatures. The results showed that the
1054 performance of the fuel cell utilizing Pt (0.5 mg cm^{-2}) both at anode and cathode with
1055 1.0 M KOH increased from 13 to 29 mW cm^{-2} with the temperature rising from 20 to
1056 80ºC when hydrogen (250 sccm, RH=95%) was fed on the anode and air (250 sccm,
1057 RH=95%) was fed on the cathode. In contrast, the fuel cell employing 0.5 M H_2SO_4
1058 yielded an increasing power density of 17 to 28 mW cm^{-2} with temperature elevating
1059 from 20ºC to 60ºC. Further increasing the temperature to 80ºC, there was no obvious
1060 performance promotion occurring, which was probably attributed to the electrocatalyst
1061 passivation in H_2SO_4 at high temperatures. Second, it could be seen from the
1062 performance tests that the peak power densities of fuel cells employing 0.5 M H_2SO_4,
1063 1.0 M TMAOH, and 1.0 M KOH as electrolytes were 17, 14, and 13 mW cm^{-2} at 20ºC,
1064 respectively. It was suggested that electrolyte concentration could change the cell
1065 impedance, resulting in the change of cell performance. Finally, the effects of organic
1066 molecular size on the performance have been studied [172]. It was shown that the

smaller organic molecular size resulted in the higher power density due to the more active sites on the electrode surface. Moreover, when the organic alkaline electrolyte was used, the cell performance decreased significantly caused by CO_2 and acid.

5.4.2. Effect of carbonate

The absorption of the CO_2 on the membrane, denoted as carbonate effect, has negative effects on the performance of the AAEMFCs. Due to the formation of carbonates within the CL and AAEM, the conductivity will decrease significantly, resulting in a large performance drop [173,174]. Hence, the carbonate effect has been extensively studied [175-182]. Fukuta et al. [175] found that the maximum power density of the alkaline fuel cell in the case of pure air was 290 mW cm^{-2}, which was as twice as that in the case of ambient air. It was determined that the OH^- form membrane could easily absorb CO_2, change to HCO_3^- form, then through the self-purging phenomenon, finally return to OH^- form. Vega et al. studied the effects of CO_2, HCO_3^-, and CO_3^{2-} on the AAEMFC operation [176-179]. They found that a 26% conductivity decrease occurred when the membrane was exposed to hydroxide ions due to the nucleophilic attack degradation mechanisms and Hofmann elimination, while the effect of exposure to carbonate environments was not significant because the carbonate was weaker nucleophiles. However, the overall conductivity of the membrane exposed to hydroxide ions was higher, which was attributed to the carbonate adsorption on the electrode, reducing the

active area. Inaba et al. [180] and Matsui et al. [181] showed that the membrane resistance decreased due to the self-purging mechanism at high current densities, while the cell voltage was reduced significantly. It was demonstrated that a high anodic overpotential occurred because of the accumulation of carbonate/bicarbonate ions at the anode, while the overpotential of the cathode was hardly changed, suggesting that it was important to suppress the accumulation. Suzuki et al. [182] investigated the effect of CO_2 dissolution into anion exchange membrane on fuel cell performance. They found that the conductivity of AAEM and potential difference decreased with an increase in carbonate ion species. It was indicated that the increment of ohmic resistance was noticeable by the supply of CO_2 to cathode, but not obvious by the supply of CO_2 to anode. They demonstrated that the formation and exclusion of carbonate ion species and/or carbonic acid in the vicinity of TPB played the dominant role for the electrode overpotential.

5.4.3. Effect of radiation

Recently, the radiation-grafted AAEMs have attracted worldwide attention, which is attributed to several advantages [183,184]: (1) Radiation grafting is one of the most versatile techniques for preparing membrane materials; (2) No film formation process is required due to the use of pre-formed polymer films; (3) The degree of monomer grafting is tunable, which can be achieved by optimizing the grafting parameters; and

(4) Simple preparation procedures and absence of highly reactive chemical initiators and catalysts result in reduction of cost. Hence, a large amount of radiation-grafted AAEMs have been synthesized [185-191]. Varcoe et al. [185] synthesized an alkaline AAEM based on ethylene-co-tetrafluoroethylene (ETFE), which was physically strong, quaternary-ammonium-functionalized, and radiation-grafted. The results from H_2/O_2 fuel cell fabricated with Pt (0.5 mg cm^{-2}) both at anode and cathode showed that a peak power density of 130 mW cm^{-2} has been achieved with both humidified hydrogen and oxygen fed at flow rates of 2000 sccm at 60°C. They stated that the performance was substantially limited by the mass transport in the electrodes. In addition, Poynton et al. [186] synthesized various ETFE AAEMs via e-beam irradiation. Afterwards, it was found that the conductivities of the thinnest membrane (17 μm, denoted as S20) reached to 60 mS cm^{-1}, and the fuel cell fabricated with S20 membrane and Pt (0.5 mg cm^{-2}) both at anode and cathode yielded a peak power density of 230 $mWcm^{-2}$ along with both humidified hydrogen and oxygen at flow rates at 2000 sccm at 50°C. The improvement in the performance was attributed to the better mass transport. Similarly, Nikolic et al. [187] prepared three different types of modified PVA based membranes, namely plain PVA, γ-PVA cross-linked using gamma irradiation, and PVA doped with Mo (PVA-Mo). The results from the power output tests showed that the peak power density of the fuel cell fabricated with Pt (0.2 mg cm^{-2}) both at anode and cathode

employing modified γ-PVA and PVA-Mo membranes were 6.4 and 6.8 mW cm^{-2}, which were better than that using plain PVA membrane (5.0 mW cm^{-2}) due to larger absorption of alkaline solution. Deavin et al. [188] prepared radiation-grafted alkaline AAEMs containing pendent groups with either benzyltrimethylammonium (BTM) or benzylmethylimidazolium (BMI) and made comparison of two AAEMs. It was indicated that, though the BMI-AAEM possessed comparable conductivity to the BTM-benchmark AAEM, the BMI-AAEM showed severe *in-situ* degradation due to the intrinsically poor chemical stability in strong alkaline media. It was demonstrated that there was no real advantage in using anion-exchange polymer electrolytes containing pendent imidazolium groups in strong alkaline systems. Fang et al. [189] developed radiation-grafted ETFE-based membrane via quaternization and crosslinking with DABCO, alkylation with p-Xylylenedichloride (DCX), and quaternization again with TMA, of which the ionic conductivity is 3.9 × 10^{-2} S cm^{-1} at 20℃ in DI water. Importantly, the conductivity increases to 7.4 × 10^{-2} S cm^{-1} at 80ºC. Meanwhile, the conductivity could be retained for 120 h after being treated in KOH solution at 60ºC. An OCV of 1.034 V and a peak power density of 48 mW cm^{-2} were obtained under 100% relative humidity with H_2 and O_2 both fed at rates of 100 mL min^{-1}. The performance was derived from good leak tightness of electrodes and enhanced electrochemical reaction kinetics. Recently, Wang et al. [190] utilized 30 kGy absorbed dose, 5 vol%

1143 VBC monomer, and water as diluent to synthesize a ETFE-based radiation-grafted
1144 AAEM. When comparing to the prior state-of-the-art protocol, this new method was
1145 closer to a commercially-relevant roll-to-roll process. The obtained AAEM exhibited a
1146 similar IEC of 2.1 mmol g^{-1}, a higher Cl^- anion-conductivity of 68 mS cm^{-1} *vs*. 48 mS
1147 cm^{-1} at 80ºC, and a better mechanical stability. Meanwhile, they employed a non-
1148 fluorinated polymer film (low-density polyethylene (LDPE)) as precursor to prepare
1149 radiation-drafted AAEM [191]. As a result, the LDPE-AAEM showed a OH^- anion
1150 conductivity of 145 mS cm^{-1} at 80ºC with 95% RH and a Cl^- anion conductivity of 76
1151 mS cm^{-1} at 80ºC when fully hydrated. It was indicated that the LDPE-AAEM
1152 outperformed the ETFE-AAEM in an AAEMFC, which was attributed to higher anion
1153 conductivity and enhanced *in situ* water transport. It was worthwhile to note that the
1154 LDPE-AAEM was more mechanically robust than ETFE-AAEM, resulting in the
1155 ability to routinely evaluate them in fuel cells at 80ºC, whereas the ETFE-AAEM was
1156 limited to operation at 60ºC.
1157 In summary, various materials based AAEMs have been synthesized, and the
1158 performance of the fabricated MEAs have been evaluated in H_2/O_2 fuel cells
1159 subsequently. Meanwhile, novel structures in the MEA have been proposed, which
1160 possess superior properties than conventional MEAs. Though significant progress has
1161 been made in developing AAEMs with high performance as well as low cost, it should

be noted that the AAEMs are still facing variety of challenges, including hydroxide-ion conductivity, as well as mechanical, chemical, and thermal stability.

6. Single-cell: Designs and performance

6.1. Effect of anode ionomers

In the anode, novel ionomers and fine microstructures have been proposed for the enhancement of the mass transport and current collection [192-196]. Recently, Sun et al. [192] prepared pendant quaternary ammonium-based ionomers employing styrene-ethylene/butylene-styrene (SEBS) as the starting material, which were dimensionally stable without drastic sacrifice of the ionic conductivity as compared to the polysulfone (PSf)-based ionomers. It was indicated that a peak power density of 210 mW cm^{-2} was obtained in a single cell using Pt (1.28 mg cm^{-2}) both at the anode and cathode with hydrogen (RH=100%) and oxygen (RH=100%) fed at a rate of 200 sccm at 50ºC. They demonstrated that the superior performance of the ionomers was attributed to the lower internal resistance and charge transfer resistance owing to the excellent dimensional stability and the balanced conductivity-hydrophobicity. Matsumoto et al. [193] described a novel structure composed of CNTs and KOH-doped PBI, forming a nanometer thickness wrapping layer, on which the Pt nanoparticles were loaded, as shown in Figs. 7 (a) and 7 (b). It was shown that the CNTs and the KOH-doped PBI layer functioned as electron and hydroxide conductive pathways, respectively. The

1181 sufficient formation of the interfacial structure resulted in the excellent mass transport
1182 around the TPBs. A peak power density of 256 mW cm^{-2} was achieved with the newly
1183 developed electrode fabricated with Pt (0.45 mg cm^{-2}) both at the anode and cathode
1184 when hydrogen (RH=95%) and oxygen (RH=95%) were supplied at flow rates of 100
1185 and 200 sccm, respectively, which is much higher than that of the AS-4 cell primarily
1186 due to the better mass transport. Yang et al. [194] reported that the ionomer content
1187 played an important role in the cell activation, ohmic and concentration losses and
1188 resulted in a high-performance electrode with fine microstructure synthesized by 20
1189 wt. % ionomer content and the proper dispersion solvent, including solutions and
1190 colloid. It was indicated when the n-butyl acetate (NBA) worked as solvent and ionomer
1191 content was kept at 20 wt.%, the colloidal electrode increased the pore volume and pore
1192 diameter, serialized ionomer networks and decreased ohmic and concentration losses,
1193 resulting in a peak power density of 407 mW cm^{-2} in an AAEMFC fabricated with Pt
1194 (0.4 mg cm^{-2}) both at anode and cathode with hydrogen (RH=100%) fed at a flow rate
1195 of 100 sccm and oxygen (RH=100%) fed at a flow rate of 200 sccm at 50°C. Ewing et
1196 al. [195] synthesized dendritic nano-sized nickel nanoparticles via a hydrazine
1197 reduction method in ethylene glycol from a nickel chloride precursor. They
1198 characterized the resulting particles by XRD, TEM, and SEM. The results showed that
1199 the single nickel particles gradually connected to form nickel chains, and subsequently

the chains connected to form the dendritic structures. Furthermore, the nickel particle was amorphous, which provided more active sites. In addition, they used the dendritic nickels with a network structure as the anode for an AAEMFC, resulting in a current density of 11.5 mA cm^{-2}. Kucernak et al. [196] proposed porous silver membranes as potential substrates for gas transport electrodes in alkaline fuel cells. The silver membrane possessed three integrated functions, including electrocatalytic function, mechanical support and current collection. An OCV of 1.05 V and a maximum power density of 60 mW cm^{-2} were obtained in an alkaline AAEMFC constructed with these electrodes with Pt (0.05 mg cm^{-2}) both at anode and cathode with hydrogen (RH=75%) and oxygen (RH=75%) at 50°C. It was indicated that the gas transport layers were as three times expensive as carbon-based layers, but especially considering their significantly reduced thickness, 700-fold superior electrical conductance, and thermal conductivity, the Ag electrode still had the potential to be used in AAEMFCs.

In summary, the ionomers play an important role in enhancing the mass transport and lowering internal resistance that further leads to superior power output. In addition, the well-dispersed electrocatalysts result in the sufficient TPBs, which is beneficial to improving the cell performance.

6.2. Effect of cathode ionomers

In the cathode, novel ionomers and structures have been reported recently [197-202].

Ünlü et al. [197] synthesized AEIs with different quaternary ammonium density and evaluated the performance via impedance spectroscopy and voltammetry. The obtained results indicated that the limited cell performance on the cathode was the low catalyst utilization, which was primarily attributed to the low ionic conductivities and high WUs of the AEIs. Hence, tremendous efforts have been devoted into synthesizing various ionomers with high hydroxide ions conductivity and low WU for promoting the mass transport in order to enhance the catalyst utilization. Gu et al. [198] reported a phosphonium based ionomer (TPQPOH) and simply used it to prepare the catalyst layer with Ag. The Ag-phosphonium ionomer interface yielded a high peak power density of 208 mW cm^{-2}, which was more than double of that of the Ag-ammonium ionomer interface and slightly higher than that of the Pt based electrode. Ünlü et al. [199] used an ionomer impregnation method to elevate the performance by tailoring the ionomer distribution and balancing the ionic, electronic, and reactant transport within the catalyst layer as shown in Figs. 8 (a) and 8 (b). It was shown that the maximum power density was promoted from 44 mW cm^{-2} to 120 mW cm^{-2} via the ionomer impregnation method, and further increased to 315 mW cm^{-2} via adding hydrophobic additive with Pt (0.5 mg cm^{-2}) both at anode and cathode at 70^{o}C due to the higher catalyst utilization and free volumes close to diffusion layer. Zhou et al. [200] prepared a series of partially fluorinated copoly(arylene ether) alkaline ionomers (QAPAE) via chloromethylation of

1238 copoly(arylene ether) followed by amination with trimethylamine. The WU of QAPAE
1239 was significantly reduced because of the presence of the hydrophobic octafluoro-
1240 biphenyl groups in the backbone. It was demonstrated that the QAPAE-4 and QAPSF
1241 ionomers employed as cathode in a hybrid AAEM/PEM fuel cell fabricated with Pt (0.5
1242 mg cm^{-2}) both at anode and cathode utilizing humidified hydrogen as fuel and oxygen
1243 as oxidant yielded the peak power density of 315 mW cm^{-2} and 215 mW cm^{-2} at 60°C,
1244 respectively. The interfacial adhesion of MEAs still remained a challenge because the
1245 hydrocarbon ionomer possessed low binding ability. Kubo et al. [201] reported the
1246 effect of hydroxide-ion conducting layered double hydroxides (LDHs) on the ORR.
1247 Two types of LDH were prepared, denoted as Ni-Al CO_3^{2-} LDH and Mg-Al CO_3^{2-} LDH.
1248 It was indicated that the addition of LDHs to the catalyst layer increased the reduction
1249 current for ORR due to the introduced OH^- conducting paths and the increased TPB
1250 region. In addition, the Ni-Al CO_3^{2-} LDH possessed better performance than the Mg-
1251 Al CO_3^{2-} LDH. Tamain et al. [202] came up with a hypothesis that the limited power
1252 output was mainly attributed to limitation of the mass transport of reactant water to the
1253 cathode reaction sites, which kept the membrane hydrated for sufficient conductivity.
1254 Hence, the hydrophobic binder, PTFE, was replaced by Toray carbon paper, aiming at
1255 improving the characteristics of the water transport. The H_2/O_2 fuel cell with the
1256 cathode fabricated from Toray carbon paper and Pt/C catalyst (20 wt. % Pt on Vulcan

XC-72R carbon support) resulted in a peak power density of 125 mW cm^{-2}, which was 25% to 36% more than the power output compared to the that of the fuel cells fabricated with the PTFE-containing cathodes.

In summary, the ionomers on the cathode play an important role in the property of the cathode. It should be noted that lower WUs, higher ionic conductivities, and higher catalyst utilizations result in the improvement of the power output. In addition, since water is consumed in cathode, humidification of oxygen is necessary in cathode. Otherwise, the ORR is difficult to proceed in the absence of water at the cathode.

6.3. Effect of structural designs

The performance of the AAEMFC lies on three primary parameters as follows: (1) the electrocatalysts for HOR and ORR that determine the electrochemical kinetics; (2) the structure of MEA that influences the transport of mass, ions, and electrons; and (3) the operation conditions that affect the electrochemical and transport behaviors and thus the power output.

In addition to the development of novel electrocatalysts for the HOR and ORR, the effects of structural designs also have been investigated [16,203,204]. It is widely believed that a superior design of flow field, anode, and cathode leads to a better performance, resulting from the enhanced mass transport and the sufficient TPBs. It should be noted that the mass transport also plays an important role in the fuel cell

performance. For the mass transport in the anode, it is vitally important to design the flow field and diffusion layer to lead hydrogen to distribute as even as possible, maximizing the cell voltage. On the cathode, the critical mass transport issues can be concluded as follows: (1) it is necessary to design the flow field and diffusion layer; (2) it is critical to enhance the transport of oxygen in the through-plane direction; (3) in the in-plane direction, the distribution of oxygen needs to be uniform over the CL. For the mass transport through the membrane, the key issue is to suppress the hydrogen crossover so that the mixed potential problem can be alleviated and hydrogen will not be wasted. The reduction of crossover can be achieved when the design of the MEA is optimal, particularly the cathode backing layer and microporous layer. Mamlouk et al. [203] studied the effects of ionomer content, anode and cathode CL thicknesses, and membrane thickness on the performance of an AAEMFC. It was indicated that an optimum ionomer content depended on a balance between the OH^- ion/water mobility and the oxygen solubility/diffusivity through it. When the ionomer content in the CL was too high, the mass transport through the ionomer could be impeded. Moreover, the electrocatalyst and carbon particles could be electron-isolated. When too low, the insufficient ECSA resulted in the lower utilization of the electrocatalysts. In addition, the limiting OH^- mobility leaded to the larger ohmic loss. It was suggested that thick anode CL was necessary because the flooding problem could be avoided when the fuel

cell was operated at high current densities, meaning that more water was produced in the anode CL. Meanwhile, the effect of the cathode CL on the performance have been studied. It was indicated that an optimum of the cathode CL thickness depended on the operating conditions, including oxygen partial pressure and ionomer used. A thicker CL with smaller particle size might suffer from the oxygen starvation problem, when the oxygen supply was inadequate. While a thinner layer with larger particle size might not possess the enough ECSA. The AAEM, the key component of the AAEMFC, worked as the barrier separating the anode and cathode, as well as the pathway for OH^- transport. Thus, the optimal membrane thickness lay on the equilibrium of the OH^- transport and gas permeability. The single fuel cell tests showed that the membrane with hydrated thickness of 57 μm resulted in a peak power density of 337 mW cm^{-2} with the air at 60°C.

6.4. Effect of water flooding

Additionally, water management is critical to achieve better performance and durability. In AAEMFCs, water is produced in the anode and consumed in the cathode. Therefore, the flooding problem that limits the cell performance is more likely to arise in the anode. To achieve a better power output, it is essential to undertake water management to mitigate the flooding problem. Zhang et al. [16] confirmed that the direction of water movement was from the anode to the cathode via a water collection method, which

indicated the diffusion water was much larger than the electro-osmosis water. At high current densities, much more water moved from the anode to cathode, which not only alleviates the flooding problem at the anode but also reduces membrane resistance. Oshiba et al. [204] proposed two methods to suppress the anode flooding. One was to increase the anode flow rate: when the RH at the anode outlet reached 100%, the current density increased with the anode flow rate, indicating that the anode flooding problem was alleviated. The other was to reduce the membrane thickness: when the membrane became thinner, the water produced in the anode was easily permeated to the cathode. Recently, Omasta et al. [205] pointed out that the amount and balance of water was a critical issue to obtain high performance that could be achieved by tuning the cell water to optimize the dynamic balance between membrane hydration and electrode flooding/dry-out. It was indicated that the cell water was able to be actively manipulated via several variables, including gas feed dew points, catalyst layer hydrophobicity, anode and cathode gas flow rates, flow channel design, catalyst layer engineering, and the physicochemical properties of the AAEM and AEIs.

6.5. Single-cell durability

Durability of fuel cells is one of the critical issues in realizing the commercialization [206-208]. Hence, Slade et al. [206] demonstrated that the AAEMs must be evaluated in H_2/O_2, H_2/air, and methanol/air fuel cells for several thousand hours to ensure

adequate *in-situ* membrane stability. Though some synthesized AAEMs exhibited exceptional fuel cell performance, the poor durability has still not been solved yet. Luo et al. [207] proposed two strategies to improve the durability of QPMBV membranes. The first was to increase glass transition temperature and molecular weight via eliminating butyl acrylate from the monomers. The second was to reduce the WU and SR via crosslinking to lock the functionalized QPMV into a poly (divinylbenzene) (PDVB) polymer network. It was indicated that the fuel cell employing crosslinked QPMV-PDVB AAEM could continuously work for 420 h at 50°C and 146 h at 70°C, which was eight and three times longer than that in previous study, respectively, as shown in Figs. 9 (a) and 9 (b). Fujimoto et al. [208] investigated the backbone stability of benzyl-trimethyl ammonium (BTMA) functionalized polyaromatics in two structurally differing polymer architectures: quaternized poly(aryleneether) (PAE) and PP. It was indicated that the cleavage of aryl-ether linkages substantially impacted the mechanical properties and moderately the hydroxide conductivity. The results showed that the PAE MEA experienced failure at 55 h due to the degraded mechanical stability while the PP MEA exhibited stable performance during 300-h operation.

6.6. Single-cell performance

Herein, we summarize the peak power densities reported in the recent literatures. Tables 1-4 show the selected hydrogen/oxygen fuel cell performance with different HOR

electrocatalysts, ORR electrocatalysts, AAEMs, and MEA structures, respectively. It can be seen from Tables that power density has been boosted from ~0.4 mW cm^{-2} to 1450 mW cm^{-2} in recent years, suggesting that the AAEMFC is a promising energy technology and tremendous efforts have been paid into this field [70,74,97,190,191,194,205,209,210]. Hu et al. [74] fabricated an AAEMFC, which exhibited the highest power density of 40 mW cm^{-2} with humidified hydrogen and oxygen both at a flow rate of 50 sccm at 60ºC, when Ni-W (17.5 mg cm^{-2}), CoPPY/C (2 mg cm^{-2}), and xQAPS were employed as anode electrocatalyst, cathode electrocatalyst and AAEM, respectively. Carmo et al. [209] developed an AAEMFC with 20 wt. % Pt/C (0.8 mg cm^{-2}) and 25% FAA-3 ionomer in the catalyst layer for both the cathode and anode. It was indicated that a peak power density of 223 mW cm^{-2} was obtained using hydrogen (100% humidity) as fuel at 200 sccm and oxygen (100% humidity) as oxidation at 200 sccm. In addition, the platinum requirement could be decreased to 0.5 mg cm^{-2} without sacrificing the performance. Recently, Ohyama et al. [70] developed a fuel cell employing 0.5 mg cm^{-2} Ru/C (3 nm) as anode electrocatalyst, 0.5 mg cm^{-2} Pt/C as cathode electrocatalyst, and an AAEM (Tokuyama A201), resulting in an excellent peak power density of 250 mW cm^{-2}. The significant enhancement was substantially attributed to the larger surface area per unit weight of Ru/C, which resulted in the higher limiting current density. He et al. [97] reported a novel cathode

electrocatalyst, CoO/rGO(N). The results from the fuel cell tests showed that the peak power density reached 387 mW cm^{-2} with the hydrogen (62% RH) fed to the anode at a rate of 250 sccm and the oxygen (100% RH) fed to the cathode at a rate of 200 sccm, when the Pt and CoO/rGO(N) are employed as anode electrocatalyst and cathode electrocatalyst, respectively, as well as an AAEM (Tokuyama A201). Yang et al. [194] fabricated high-performance electrodes with fine microstructure by changing the content of the ionomer and selecting the appropriate dispersion solvent. A maximum power density of 358 mW cm^{-2} was achieved when the ionomer content is 20 wt. % (CCM-I20) with humidified H_2 in the anode at a rate of 100 sccm and humidified O_2 in the cathode at a rate of 200 sccm at 50°C, which is three and five times of CCM-I25 and CCM I10, respectively. Importantly, the peak power density increased remarkably to 407 mW cm^{-2} when the dispersion solution changed to NBA. Recently, Wang et al. [210] found that the highest power density of 1000 mW cm^{-2} was obtained when Pt-Ru (0.4 mg cm^{-2}) is utilized as anode electrocatalyst, Pt (0.4 mg cm^{-2}) is used as cathode electrocatalyst, and H_2 and O_2 were fed at flow rates at 400 sccm at 60°C, which was 400 mW cm^{-2} higher than the performance of a fuel cell running under the same conditions apart from the unitary anode electrocatalyst Pt as shown in Fig. 9 (c). It has been revealed that the enhancement in the kinetics of the HOR was attributed to weakening the Pt-H_{ad} interaction rather than the ever reported oxophilic effect.

Breakthroughs in power output has been reported vary recently [190,191,205], as shown in Figs. 9 (d) (e) and (f). A peak power density of 1.4 Wcm^{-2} was achieved with hydrogen and oxygen both at a flow rate of 1000 sccm at 60ºC, when PtRu (0.67 mg cm^{-2}) and Pt (0.53 mg cm^{-2}) were employed as anode electrocatalyst and cathode electrocatalyst, respectively [205]. More importantly, the dew points for the electrode configuration was optimized to 54/57ºC, which was the same thing as RHs equal to 75%/85%. The spectacular performance was primarily attributed to the optimal balance between necessary membrane hydration and electrode flooding/dry-out. To date, 1.4 W cm^{-2} was the highest peak power density at 60ºC. As Wang et al. [191] developed a LDPE-AAEM that possessed the ability to be routinely evaluated in fuel cells at 80ºC, the H_2/O_2 AAEMFC fabricated with this AAEM, a PtRu/C anode (0.4 mg cm^{-2}), and a Pt/C cathode (0.4 mg cm^{-2}) exhibited a peak power density as high as 1.45 W cm^{-2}. It was claimed that avoiding anode flooding and enhancing supply of H_2O to the cathode reaction sites contributed to the splendid power output. Since the reactant diffusion limitations in anode and cathode at high current densities were more serious at 80ºC than 60ºC, the effects of the water management on the performance were more significant.

7. Innovative system designs

7.1. Hybrid fuel cells

Recently, some innovative structures have been proposed with the purpose of improving the fuel cell performance [211-216]. Ünlü et al. [211] developed a novel hybrid polymer electrolyte fuel cell, as shown in Fig. 10 (a), in which the hybrid membrane was composed of a proton exchange membrane sandwiched by two AAEMs, denoted as AAEM/PEM/AAEM fuel cell, simplifying water management and avoiding CO poisoning. The hybrid fuel cell fabricated with Pt (0.5 mg cm^{-2}) both at anode and cathode exhibited a peak power density of 55.6 mW cm^{-2} with H_2 (RH = 100%) and O_2 (RH = 100%) supplied at a rate of 360 and 480 sccm, respectively. The peak power density increased to 78.3 mW cm^{-2} at 0% RH under the same conditions. They claimed that the unpredictable phenomenon was attributed to the superior water management configuration. However, Shen et al. [212] developed a type of non-flooding hybrid polymer fuel cell, in which a PEM and an AAEM were pressed together. They found that the performance was improved with increasing the temperature and relative humidity, which was opposed to the results reported by Ünlü et al [211]. Zhang et al. [213] developed a hybrid system consisting of an alkaline fuel cell and a heat-driven cycle as shown in Fig. 10 (b), which reused the waste heat to improve the maximum equivalent power output. The hybrid system showed superior performance, which was 1.4 times higher than that achieved by a single AAEMFC. Ünlü et al. [214] proposed a novel hybrid anion and proton exchange membrane fuel cell, denoted as AAEM

cathode/PEM anode and PEM anode/AAEM cathode, as shown in Fig. 10 (c), which exploited the electrochemical advantages of the high-pH operation due to at least one electrode being at high pH. They illustrated that the AAEM cathode/PEM anode junction failed at high current densities resulting from the inadequate flux of water to the AAEM/PEM interface where water dissociated into hydrogen ions (which migrates to the cathode) and hydroxide ions (which migrates to the anode). On the contrary, the PEM anode/AAEM cathode junction was shown to be an available configuration. Despite the modest power density, the type of structure exhibited steady performance with 0% relative humidity at 65ºC for a three-day continuous operation, whereas the conventional fuel cell experienced severe degradation over the same time without humidification. They also evaluated the effect of RH, ionomer content in the anion-conductive electrode and the inlet gas flow rates on the performance of the hybrid fuel cells, as shown in Fig. 10 (d) [215]. The results showed that the ionomer fraction of the high-pH cathode played an important role in the performance, which was limited by the availability of oxygen in the active sites resulting from the flooding in the cathode. When the gases were fed at high flow rates, the water removal from cathode was enhanced and the flooding problem was eliminated. Fukuta et al. [216] tested the optimization of MEA construction employing newly developed membrane and ionomer by Tokuyama, which was one of the leading developers of electrolyte materials for

AAEMFCs, to improve the power density. They suggested that the optimized MEA was fabricated with ionomer: AS-X (Pt/C:AS-X = 70:30), membrane: A901, and Pt (0.5 mg cm^{-2}) both at the anode and cathode, exhibiting a peak power density of 450 mW cm^{-2} with humidified hydrogen at a flow rate of 1000 sccm and pure oxygen at a flow rate of 2000 sccm. In summary, several novel structure designs that are mainly associated with the MEA construction have been proposed. As a result, the performance is promoted due to the superior water management, the use of preferable pH value, and the low degradation rate of membrane.

7.2. Regenerative fuel cells

Regenerative fuel cell (RFC) is not only an energy conversion device, but an energy storage machine, which typically employs hydrogen as a flexible energy carrier, as shown in Fig. 11. It is the concept that the fabricated electrodes, which exhibit catalytic activities for both ORR and oxygen evolution reaction (OER), can be used as either electrolyzer or a fuel cell. When the AAEM-RFC is working as an electrolyzer, water reacts with electrons to produce hydrogen and hydroxide ions at the cathode according to:

$$4H_2O+4e^-\rightarrow 4OH^-+2H_2 \quad (16)$$

The hydroxide ions are transported through the AAEM to the anode catalyst layer where the hydroxide ions are oxidized to release electrons, oxygen and water according to:

$$4OH^- \rightarrow 2H_2O + 4e^- + O_2 \quad (17)$$

Hence, the Eq. (16) and the Eq. (17) result in the overall reaction:

$$2H_2O \rightarrow 2H_2 + O_2 \quad (18)$$

The produced hydrogen is stored on site after the electrolysis, and can be used as fuel in the fuel cell anode subsequently when the electricity is needed. The reactions of the fuel cell mode have been mentioned earlier take place. Though the RFC is a particular candidate for storing renewable electricity, the high cost still is the primary impediment for the commercialization. The main reason for the high cost is ascribed to the use of platinum group metal catalysts. Ng et al. [217] developed a bifunctional Ni based on carbon black (Ni/C) electrocatalyst for the H_2 electrode because the Ni possessed catalytical activity for the hydrogen evolution reaction (HER) and the HOR. It was shown that the Ni/C electrocatalyst exhibited comparable activity to the Pt/C electrocatalyst at low potentials, while the activity began to decrease at high potential due to the Ni oxidation. Meanwhile, they synthesized a precious-metal free and carbon-free O_2 electrode via electrodeposition of manganese oxide (MnO_x) on a stainless steel (SS) substrate followed by high-temperature calcination at 480ºC [218]. It was revealed that the fabricated electrode possessed comparable oxygen reduction and water oxidation activities and durability to the precious-metal based electrode, which was attributed to avoiding the carbon corrosion. Wu et al. [219] prepared four nanometer

size $Cu_xMn_{0.9-x}Co_{2.1}O_4$ samples (x = 0, 0.3, 0.6, and 0.9) as a non-precious metal based bifunctional oxygen electrode for the use in regenerative fuel cells and studied their characteristics with XRD, SEM, TEM, and cyclic voltammetry. It was indicated that the $Cu_xMn_{0.9-x}Co_{2.1}O_4$ electrode exhibited promising ORR activity which was similar to Pt/C electrode and a peak power density of 80 mW cm^{-2} was obtained. Meanwhile, in electrolyzer mode, the prepared electrode showed better OER catalytic activity, with 100 mV more negative onset potentials. Matsushima et al. [220] investigated the three-phase interfacial phenomena in alkaline regenerative fuel cell by a charge-coupled device (CCD) and confocal laser microscopy. It was shown from the results that the hydroxide ions reduced the surface tension, resulting in the spread of the three-phase interface. Consequently, the ORR was promoted as a result of the obvious enlargement of the reaction surface and the short diffusion path of dissolved oxygen. On the other hand, the OER was enhanced by the convectional factor of gas evolution. In summary, to develop a cost-effective energy storage technology that is for grid-scale applications, it is crucial to realize the utilization of renewable energy sources such as wind and solar. Undoubtedly, the RFCs using solar and wind are composed the idea of circulation and the concept of sustainable. Although great progress has been made, one issue needs to be addressed. Currently, the precious metals are mainly the electrocatalysts both in anode and cathode, leading to the high cost of the RFCs. As a result, the

commercialization is shadowed. Hence, it is urgent to develop non-precious metal electrocatalysts to reduce the cost. However, the non-precious metal electrocatalysts in one electrode are generally not effective enough to catalyze the two reactions. Hence, future direction is to synthesize cost-efficient electrocatalysts with highly catalytic activity.

8. Mathematical modeling

As an economical and useful tool, mathematical modeling can play a significant role in the quantification of the intricate physicochemical processes in AAEMFCs. Hence, various models have been conducted on predicting the hydroxyl anion conductivity [221], analyzing the concentration profile of carbonate ions [222], and studying the effect of design and operating parameters on the fuel cell performance [223-232]. Jiao et al. [223] developed a three-dimensional multiphase model to investigate the effect of design and operating parameters on the heat and mass transfer characteristics and performance. It was indicated the power output was improved sharply with more anode humidification at the range of 50% to 80%, whereas the enhancement was less significant at higher humidification levels. Moreover, the cathode humidification played a more important role than that of anode, showing a positive effect on performance, especially at high current densities. When the liquid water volume fraction on the cathode reached 0.02, the liquid water began to move from channels to

1523 the CL. With the liquid water volume fraction increasing to 0.08, a balance was formed
1524 between the anode and the cathode. The performance was promoted with the decrease
1525 of the membrane thickness due to the reduction of the mass transport loss between the
1526 anode and the cathode. Deng et al. [226] developed a 3-D multiphase non-isothermal
1527 model for the whole hydrogen-fed AAEMFC. It was shown from the results that the
1528 insertion of anode MPL, increment of anode back pressure and decrement of membrane
1529 thickness generally improved the cell performance. In addition, the water behavior was
1530 also studied and it was found that at high current densities, no water was observed in
1531 the cathode due to the electro-osmotic drag by ion transport and consumption as the
1532 reactant; while, at low current densities, liquid water may exist in cathode arising from
1533 improving the anode back diffusion or reducing the membrane thickness. When anode
1534 back pressure increased and membrane thickness decreased, the water transport from
1535 anode to cathode was changed from diffusion dominated to diffusion/hydraulic
1536 permeation dominated. Huo et al. [227] developed a numerical model to investigate the
1537 water transport in the anode. Fig. 12 (a) depicted the distributions of liquid water in
1538 anode catalyst layer and gas diffusion layer. It was indicated that the current density and
1539 temperature were two crucial parameters influencing the liquid water transport. Since
1540 the current density increased from 0.05 to 1.45 A cm^{-2}, the liquid water volume fraction
1541 in the anode increased due to more water produced and dragged to the anode. In addition,

1542 the liquid water volume fraction in the anode decreased with the temperature due to
1543 more water evaporated, suggesting that the anode flooding was suppressed. Shiau et al.
1544 [228] developed a two-dimensional nonisothermal multiphase model to investigate the
1545 effects of operation condition on the performance. When the gases were fully
1546 humidified, the current density was higher than that of partially humidified, which was
1547 ascribed to enhanced ORR kinetics and ion/water transport through the membrane. The
1548 performance was also improved with increasing temperature due to the same reasons.
1549 A theoretical analysis conducted by Deng et al. [229] showed that a higher ionomer
1550 content resulted in a better performance under various gas relative humidity due to the
1551 improved membrane hydration and enhanced ionic conductivity. As the cathode might
1552 suffer from large performance losses resulting from the lack of water, properly
1553 increasing the water amount in cathode could effectively reduce mass transport and
1554 ohmic losses. Moreover, slight anode pressurization and insertion of MPL were
1555 preferred. However, Huo et al. [230] argued that the best configuration was only
1556 inserting MPL in anode rather than placing MPLs both in anode and cathode as shown
1557 in Fig. 12 (b). It was explained that the MPL implemented in anode forced the liquid
1558 water to back-diffuse to the cathode and MPL eliminated in cathode enhanced the water
1559 transport to the cathode CL, both of which led to a high reaction rate and membrane
1560 conductivity. Besides, decreasing the cathode CL contact angle improves the

performance because more water could be kept in the cathode CL decreasing polarization losses. Nevertheless, attention should be paid into the possibility of cathode flooding problem. Recently, Niu et al. [231] took the two-phase turbulent flow in fuel cell flow channel into consideration, which was largely ignored in previous studies. They developed a direct numerical simulation (DNS) model with modified volume-of-fluid (VOF) approach for tracking the air/water interface. It could be seen from Fig. 12 (c) that the water droplet was deformed asymmetrically and became water films spreading on the GDL surface, which was advantageous for reducing the flow resistance. Whereas such water films were difficult to be removed, therefore, the reactant supply was suppressed. Subsequently, the DNS model was used to investigate the behavior of two droplets and three droplets in turbulent and laminar flows [232]. Fig. 12 (d) depicted the proccess. In the two-droplet case, the front droplet firstly became flat and moved towards the other one. Eventually, they were merged in turbulent flow. In the laminar flow, the two droplets were also merged and the finally merged droplet was higher. In the three-droplet case, the two droplets downstream were merged firstly, followed by combining with the front droplet in turbulent flow. It was similar that the three droplets were merged and the finally merged droplet was higher in the laminar flow. Since the liquid films formed on the GDL surface moved slowly, a hydrophobic GDL surface was required for water removal enhancement.

In summary, along with the experiments, modeling and simulation play a critical role in providing detailed insights concerning the complex mass, heat and charged particle transport in an AAEMFC. Modeling is especially important when an experiment is either too expensive to conduct or unable to capture the detailed underlying physics. As the modeling studies are conducted on investigating the mass transport phenomenon in the AAEMFCs, particularly on the water management, the results can be expressed: anode flooding can be a critical issue at 100% RH, whereas at lower RH high ionic transport resistance in the cathode dominates due to dehydrated ionomer phase at high current, where the impact of water-consuming ORR kinetic polarization is also crucial.

9. Remaining challenges and perspectives

Platinum has been widely used as electrocatalyst both in anode and cathode due to its desirable electrochemical activities. However, the high cost becomes the main constraint, which makes the AAEMFC less attractive.

For the anode electrocatalysts, although the HOR is the simplest electrochemical reaction, high activity catalysts are in urgent need due to the less active HOR in basic media than that in acid media. Thus, the Pt alloys and hybrid structures with high activity and low cost have been proposed. However, there are still several problems needed for further investigation, which can be concluded as follows: (1) synthesizing highly active non-PGM electrocatalysts; (2) improving the durability of the

electrocatalysts in hash alkaline media; (3) studying the HOR process on electrocatalysts.

For the cathode electrocatalysts, considerable improvements have been made to synthesize novel ORR electrocatalysts to replace the Pt recently, but there are still remaining some problems unsolved, i.e. the low stability, the high overpotential, and the low reactivity. The proposed alternative non-PGM electrocatalysts are supposed to enhance the direct four-electron pathway and inhibit the formation of hydrogen peroxide, resulting in the promotion of the catalytic activity. Although many non-platinum electrocatalysts showing comparable activity to Pt have been prepared, as mentioned earlier, the durability and stability problems still should be addressed.

As the key component of the MEA, the AAEM is directly related to the fuel cell performance. Hence, it should be pointed out the future research direction for the synthesis of the membrane as well as the ionomer. Tang et al. [233] and Slade et al. [206] have indicated that the dissoluble ionomer is essential because the ionomer can be impregnated into the pores of the porous electrodes, working as a binder that can significantly decrease the interfacial resistance. Zeng et al. [234] found that the fundamental improvement of the fuel cell performance was attributed to the water removal from the surface of catalyst. Hence, a low swelling ionomer film with a highly hydrophilic surface is recommended. In addition, for the application of the AAEMFCs,

the AAEM is expected to work normally at a wider range of temperature. Consequently, the AAEMs are required to be thermally stable. On the other hand, the thin films also need to be mechanically stable, being both flexible and strong.

As an economical and useful tool, mathematical modeling can play a significant role in the quantification of the intricate physicochemical processes in AAEMFCs. However, as composed to the extensive experiment research on the AAEMFCs, mathematical modeling has not received similar attention. Moreover, the limited modeling studies are conducted on investigating the mass transport phenomenon in the AAEMFCs, particularly on the water management. Although water management has been verified to have vital effects on the fuel cell performance, the modeling research on the electrochemical process on the CLs is still deficient. Herein, we suggest that more attention should be focused on the modeling and mathematical analysis.

10. Concluding remarks

As the promising emerging energy technology, the AAEMFC has attracted worldwide attention recently due to the significant reduction of the cost. Consequently, great progress has been made in promoting the power density, enhancing the durability, as well as reducing the cost. Generally, the peak power density is related to temperature, DL porosity, tuned ionomer carbon ratios, electrocatalyst loadings, and carefully controlled RHs. Typically, the performance increases with the increasing temperature

due to the enhanced electrode reaction kinetics. Whereas, too high temperature is harmful to those components that are not stable enough, resulting in the performance degradation. Besides, higher DL porosity a lower mass/charge transport resistance, which is advantageous for improving power output. Nevertheless, a DL also functions as an electron transmitter and a CL supporter. Too high porosity is unfavorable for electron transport and mechanical support. Hence, an optimal DL porosity can be determined by taking these three aspects into consideration. The ionomer content has synergetic effects on the electrode microstructure and kinetic properties in terms of the active, ohmic, and mass diffusion polarizations. A deficient ionomer content in the CLs leads to non-continuous network for aiding the hydroxide transport, correspondingly lessening the reactive TPBs, and reducing the electrocatalyst utilization. However, an overloading ionomer content results in high shielding of electrocatalysts and heavy blocking of surface pores, which impedes the H_2 and O_2 in the process of diffusing to the electrocatalyst particles for carrying out the electrode reactions. Within an appropriate range, increasing electrocatalyst loading is beneficial for promoting peak power density, but too much loading will cause the agglomeration of electrocatalyst and decrease of active sites. Notably, humidifying both hydrogen and oxygen is obligatory. Considering the best performance to date, the RHs are 75% on anode and 85% on cathode. Too high RHs will result in electrode flooding problem, and too low RHs will

result in low ORR kinetics and sluggish OH^- conductivity.

This review provides an overview of the recent development on the AAEMFC, in terms of the physical and chemical processes, the electrocatalysts toward the HOR and ORR, the system designs and performance, as well as the remaining challenges and perspectives. Although promising, there is still plenty room for substantially increasing the power output before the widespread application. Further development of the AAEMFC may concentrate on, but not be limited to the following: (1) synthesize high activity, high durability, and non-PGM electrocatalysts for both hydrogen oxidation reaction and oxygen reduction reaction; (2) identify the active sites of the electrocatalysts, which is critical for understanding the catalytic mechanism and designing new electrocatalysts; (3) develop the high hydroxide-ion conductivity, low water uptake, and high durability polymer electrolyte membrane; (4) optimize the electrode design for high transport rates of mass, ions and electrons, including the ionomers and structures; (5) optimize the operating conditions for the maximum power output.

Acknowledgements

This work was supported by a grant from the Research Grants Council of the Hong Kong Special Administrative Region, China (HKUST9/CRF/11G) and a grant from the Natural Science Foundation of China (No. 51506039).

References

[1] L. An, T.S. Zhao, J.B. Xu, A bi-functional cathode structure for alkaline-acid direct ethanol fuel cells, Int. J. Hydrogen Energy 36 (2011) 13089-13095.

[2] L. An, T.S. Zhao, S.Y. Shen, Q.X. Wu, R. Chen, An alkaline direct oxidation fuel cell with non-platinum catalysts capable of converting glucose to electricity at high power output, J. Power Sources 196 (2011) 186-190.

[3] M. Mamlouk, J.A. Horsfall, C. Williams, K. Scott, Radiation grafted membranes for superior anion exchange polymer membrane fuel cells performance, Int. J. Hydrogen Energy 37 (2012) 11912-11920.

[4] L. An, T.S. Zhao, X.L. Zhou, X.H. Yan, C.Y. Jung, A low-cost, high-performance zinc-hydrogen peroxide fuel cell, J. Power Sources 275 (2015) 831-834.

[5] L. An, T.S. Zhao, X.L. Zhou, L. Wei, X.H. Yan, A high-performance ethanol-hydrogen peroxide fuel cell, RSC Adv. 4 (2014) 65031-65034.

[6] J.R. Varcoe, P. Atanassov, D.R. Dekel, A.M. Herring, M.A. Hickner, P.A. Kohl, A.R. Kucernak, W.E. Mustain, K. Nijmeijer, K. Scott, T.W. Xu, L. Zhuang, Anion-exchange membranes in electrochemical energy systems, Energy Environ. Sci. 7 (2014) 3135-3191.

[7] L. An, R. Chen, Mathematical modeling of direct formate fuel cells, Applied Thermal Engineering 124 (2017) 232-240.

[8] Y.S. Li, T.S. Zhao, Ultra-low catalyst loading cathode electrode for anion exchange

membrane fuel cells, Int. J. Hydrogen Energy 37 (2012) 15334-15338.

[9] J.R. Varcoe, M. Beillard, D.M. Halepoto, J.P. Kizewski, S.D. Poynton, R.C.T. Slade, Membrane and electrode materials for alkaline membrane fuel cells, ECS Transactions 16 (2008) 1819-1834.

[10] E.H. Yu, X. Wang, U. Krewer, L. Li, K. Scott, Direct oxidation alkaline fuel cells: from materials to systems, Energy Environ. Sci. 5 (2012) 5668-5680.

[11] L. An, T.S. Zhao, Z.H. Chai, L. Zeng, P. Tan, Modeling of the mixed potential in hydrogen peroxide-based fuel cells, Int. J. Hydrogen Energy 39 (2014) 7407-7416.

[12] Y.S. Li, Y.L. He, Layer reduction method for fabricating Pd-coated Ni foams as high-performance ethanol electrode for anion-exchange membrane fuel cells, RSC Adv. 4 (2014) 16879-16884.

[13] C.C. Duan, D. Hook, Y.C. Chen, J.H. Tong, R. O'Hayre, Zr and Y co-doped perovskite as a stable, high performance cathode for solid oxide fuel cells operating below 500oC, Energy Environ. Sci. 10 (2017) 176-182.

[14] L. An, T.S. Zhao, L. Zeng, X.H. Yan, Performance of an alkaline direct ethanol fuel cell with hydrogen peroxide as oxidant, Int. J. Hydrogen Energy 39 (2014) 2320-2324.

[15] L. An, T.S. Zhao, Performance of an alkaline-acid direct ethanol fuel cell, Int. J. Hydrogen Energy 36 (2011) 9994-9999.

1714 [16] H. Zhang, H. Ohashi, T. Tamaki, T. Yamaguchi, Direction and management of
1715 water movement in solid-state alkaline fuel cells, J. Phys. Chem. C 116 (2012) 7650-
1716 7657.
1717 [17] L. An, T.S. Zhao, L. Zeng, Agar chemical hydrogel electrode binder for fuel-
1718 electrolyte-fed fuel cells, Applied Energy 109 (2013) 67-71.
1719 [18] L. An, C.Y. Jung, Transport phenomena in direct borohydride fuel cells, Applied
1720 Energy 205 (2017) 1270-1282.
1721 [19] I. Gunasekara, M. Lee, D. Abbott, S. Mukerjee, Mass transport and oxygen
1722 reduction kinetics at an anion exchange membrane interface: microelectrode studies on
1723 effect of carbonate exchange, ECS Electrochemistry Letters 1 (2012) F16-F19.
1724 [20] L. An, R. Chen, Recent progress in alkaline direct ethylene glycol fuel cells for
1725 sustainable energy production, J. Power Sources 329 (2016) 484-501.
1726 [21] L. An, T.S. Zhao, X.H. Yan, X.L. Zhou, P. Tan, The dual role of hydrogen peroxide
1727 in fuel cells, Science Bulletin 60 (2015) 55-64.
1728 [22] Y.S. Li, J.H. Lv, Y.L. He, A monolithic carbon foam-supported pd-based catalyst
1729 towards ethanol electro-oxidation in alkaline media, J. The Electrochemical Society 163
1730 (2016) F424-F427.
1731 [23] H.Y. Hou, Recent research progress in alkaline polymer electrolyte membranes
1732 for alkaline solid fuel cells, Acta Phys. -Chim. Sin. 30 (2014) 1393-1407.

1733 [24] L. An, L. Zeng, T.S. Zhao, An alkaline direct ethylene glycol fuel cell with an
1734 alkali-doped polybenzimidazole membrane, Int. J. Hydrogen Energy 38 (2013) 10602-
1735 10606.
1736 [25] L. An, T.S. Zhao, An alkaline direct ethanol fuel cell with a cation exchange
1737 membrane, Energy Environ. Sci. 4 (2011) 2213-2217.
1738 [26] G. Merle, M. Wessling, K. Nijmeijer, Anion exchange membranes for alkaline fuel
1739 cells: A review, J. Membrane Science 377 (2011) 1-35.
1740 [27] E. Gülzow, M. Schulze, Long-term operation of AFC electrodes with CO2
1741 containing gases, J. Power Sources 127 (2004) 243-251.
1742 [28] G.F. McLean, T. Niet, S. Prince-Richard, N. Djilali, An assessment of alkaline fuel
1743 cell technology, Int. J. Hydrogen Energy 27 (2002) 507-526.
1744 [29] P. Gouérec, L. Poletto, J. Denizot, E. Sanchez-Cortezon, J.H. Miners, The
1745 evolution of the performance of alkaline fuel cells with circulating electrolyte, J. Power
1746 Sources 129 (2004) 193-204.
1747 [30] Y.J. Wang, J.L. Qiao, R. Baker, J.J. Zhang, Alkaline polymer electrolyte
1748 membranes for fuel cell applications, Chem. Soc. Rev. 42 (2013) 5768-5787.
1749 [31] Y.S. Li, T.S. Zhao, R. Chen, Cathode flooding behaviour in alkaline direct ethanol
1750 fuel cells, J. Power Sources 196 (2011) 133-139.
1751 [32] L. An, T.S. Zhao, Y.S. Li, Carbon-neutral sustainable energy technology: Direct

1752 ethanol fuel cells, Renew. Sustain. Energy Rev. 50 (2015) 1462-1468.

1753 [33] L. An, T.S. Zhao, Y.S. Li, Q.X. Wu, Charge carriers in alkaline direct oxidation

1754 fuel cells, Energy Environ. Sci. 5 (2012) 7536-7538.

1755 [34] L. An, T.S. Zhao, Transport phenomena in alkaline direct ethanol fuel cells for

1756 sustainable energy production, J. Power Sources 341 (2017) 199-211.

1757 [35] D.L. Yang, H.M. Yu, G.F. Li, W. Song, Y.X. Liu, Z.G. Shao, Effect of gas diffusion

1758 electrode parameters on anion exchange membrane fuel cell performance, Chinese

1759 Journal of Catalysis 35 (2014) 1091-1097.

1760 [36] Y.S. Li, Y.L. He, W.W. Yang, Performance characteristics of air-breathing anion-

1761 exchange membrane direct ethanol fuel cells, Int. J. Hydrogen Energy 38 (2013) 13427-

1762 13433.

1763 [37] L. An, T.S. Zhao, Q.X. Wu, L. Zeng, Comparison of different types of membrane

1764 in alkaline direct ethanol fuel cells, Int. J. Hydrogen Energy 37 (2012) 14536-14542.

1765 [38] L. An, R. Chen, Direct formate fuel cells: A review, J. Power Sources 320 (2016)

1766 127-139.

1767 [39] N. Follain, S. Roualdes, S. Marais, J. Frugier, M. Reinholdt, J. Durand, Water

1768 transport properties of plasma-modified commercial anion-exchange membrane for

1769 solid alkaline fuel cells, J. Phys. Chem. C 116 (2012) 8510-8522.

1770 [40] Y.S. Li, A liquid-electrolyte-free anion-exchange membrane direct formate-

1771 peroxide fuel cell, Int. J. Hydrogen Energy 41 (2016) 3600-3604.

1772 [41] Y.S. Li, T.S. Zhao, Understanding the performance degradation of anion-exchange

1773 membrane direct ethanol fuel cells, Int. J. Hydrogen Energy 37 (2012) 4413-4421.

1774 [42] S. Kabir, K. Lemire, K. Artyushkova, A. Roy, M. Odgaard, D. Schlueter, A.

1775 Oshchepkov, A. Bonnefont, E. Savinova, D.C. Sabarirajan, P. Mandal, E.J. Crumlin,

1776 I.V. Zenyuk, P. Atanassov, A. Serov, Platinum group metal-free NiMo hydrogen

1777 oxidation catalysts: high performance and durability in alkaline exchange membrane

1778 fuel cells, J. Mater. Chem. A 5 (2017) 24433-24443.

1779 [43] E.F. Holby, P. Zelenay, Linking structure to function: The search for active sites in

1780 non-platinum group metal oxygen reduction reaction catalysts, Nano Energy 29 (2016)

1781 54-64.

1782 [44] Y.S. Li, H. Wu, Y.L. He, Y. Liu, L. Jin, Performance of direct formate-peroxide

1783 fuel cells, J. Power Sources 287 (2015) 75-80.

1784 [45] Y.S. Li, T.S. Zhao, Z.X. Liang, Performance of alkaline electrolyte-membrane-

1785 based direct ethanol fuel cells, J. Power Sources 187 (2009) 387-392.

1786 [46] Z.F. Pan, R. Chen, L. An, Y.S. Li, Alkaline anion exchange membrane fuel cells

1787 for cogeneration of electricity and valuable chemicals, J. Power Sources 365 (2017)

1788 430-445.

1789 [47] Y.S. Li, Y. Feng, X.D. Sun, Y.L. He, A sodium-ion-conducting direct formate fuel

cell: generating electricity and producing base, Angew. Chem. 129 (2017) 5828-5831.

[48] Y.S. Li, X.D. Sun, Y. Feng, Hydroxide self-feeding high-temperature alkaline direct formate fuel cells, ChemSusChem 10 (2017) 2135-2139.

[49] X.Y. Chen, T.C. Li, J.N. Shen, Z.L. Hu, From structures, packaging to application: A system-level review for micro direct methanol fuel cell, Renewable and Sustainable Energy Reviews 80 (2017) 669-678.

[50] Y.S. Li, T.S. Zhao, A passive anion-exchange membrane direct ethanol fuel cell stack and its applications, Int. J. Hydrogen Energy 41 (2016) 20336-20342.

[51] Y.S. Li, Y.L. He, W.W. Yang, A high-performance direct formate-peroxide fuel cell with palladium-gold alloy coated foam electrodes, J. Power Sources 278 (2015) 569-573.

[52] Z. Zakaria, S.K. Kamarudin, S.N. Timmiati, Membranes for direct ethanol fuel cells: An overview, Applied Energy 163 (2016) 334-342.

[53] I. Bakosa, A. Paszternák, D. Zitoun, Pd/Ni synergestic activity for hydrogen oxidation reaction in alkaline conditions, Electrochimica Acta 176 (2015) 1074-1082.

[54] S.F. Lu, J. Pan, A.B. Huang, L. Zhuang, J.T. Lu, Alkaline polymer electrolyte fuel cells completely free from noble metal catalysts, PNAS 105 (2008) 20611-20614.

[55] R. Vinodh, D. Sangeetha, Carbon supported silver (Ag/C) electrocatalysts for alkaline membrane fuel cells, J. Mater Sci 47 (2012) 852-859.

1809 [56] M. Mamlouk, S.M.S. Kumar, P. Gouerec, K. Scott, Electrochemical and fuel cell
1810 evaluation of Co based catalyst for oxygen reduction in anion exchange polymer
1811 membrane fuel cells, J. Power Sources 196 (2011) 7594-7600.
1812 [57] Y. Ogihara, H. Yano, T. Matsumoto, D.A. Tryk, A. Liyama, H. Uchida, In situ FTIR
1813 analysis of co-tolerance of a Pt-Fe alloy with stabilized Pt skin layers as a hydrogen
1814 anode catalyst for polymer electrolyte fuel cells, Catalysts 7 (2017) 8.
1815 [58] J. Fu, J.L. Qiao, X.Z. Wang, J.X. Ma, T. Okada, Alkali doped poly(vinyl alcohol)
1816 for potential fuel cell applications, Synthetic Metals 160 (2010) 193-199.
1817 [59] M. Tanaka, K. Fukasawa, E. Nishino, S. Yamaguchi, K. Yamada, H. Tanaka, B.
1818 Bae, K. Miyatake, M. Watanabe, Anion conductive block poly(arylene ether)s:
1819 synthesis, properties, and application in alkaline fuel cells, J. Am. Chem. Soc. 133 (2011)
1820 10646-10654.
1821 [60] J.L. Yan, L. Zhu, B.L. Chaloux, M.A. Hickner, Anion exchange membranes by
1822 bromination of tetramethylbiphenol-based poly(sulfone)s, Polym. Chem. 8 (2017)
1823 2442-2449.
1824 [61] X. Wang, M.Q. Li, B.T. Golding, M. Sadeghi, Y.C. Cao, E.H. Yu, K. Scott, A
1825 polytetrafluoroethylene-quaternary 1,4-diazabicyclo- [2.2.2]-octane polysulfone
1826 composite membrane for alkaline anion exchange membrane fuel cells, Int. J. Hydrogen
1827 Energy 36 (2011) 10022-10026.

1828 [62] X.H. Li, J.X. Tao, G.H. Nie, L.C. Wang, L.H. Li, S.J. Liao, Cross-linked multiblock
1829 copoly(arylene ether sulfone) ionomer/nano-ZrO2 composite anion exchange
1830 membranes for alkaline fuel cells, RSC Adv. 4 (2014) 41398-41410.
1831 [63] M.S. Cha, J.Y. Lee, T.H. Kim, H.Y. Jeong, H.Y. Shin, S.G. Oh, Y.T. Hong,
1832 Preparation and characterization of crosslinked anion exchange membrane (AAEM)
1833 materials with poly(phenylene ether)-based short hydrophilic block for use in
1834 electrochemical applications, J. Membrane Science 530 (2017).
1835 [64] Y.S. Li, Y.L. He, An all-in-one electrode for high-performance liquid-feed micro
1836 polymer electrolyte membrane fuel cells, J. The Electrochemical Society 163 (2016)
1837 F663-F667.
1838 [65] W.C. Sheng, H.A. Gasteiger, Y. Shao-Horn, Hydrogen oxidation and evolution
1839 reaction kinetics on platinum: acid vs alkaline electrolytes, J. The Electrochemical
1840 Society 157 (2010) B1529-B1536.
1841 [66] J. Durst, A. Siebel, C. Simon, F. Hasche, J. Herranz, H.A. Gasteiger, New insights
1842 into the electrochemical hydrogen oxidation and evolution reaction mechanism, Energy
1843 Environ. Sci. 7 (2014) 2255-2260.
1844 [67] W.C. Sheng, Z.B. Zhuang. M.R. Gao, J. Zheng, J.G.G. Chen, Y.S. Yan, Correlating
1845 hydrogen oxidation and evolution activity on platinum at different pH with measured
1846 hydrogen binding energy, Nat. Commun. 6 (2015) 5848-5853.

1847 [68] I. Ledezma-Yanez, W.D.Z. Wallace, P. Sebastián-Pascual, V. Climent, J.M. Feliu,
1848 M.T.M. Koper, Interfacial water reorganization as a pH-dependent descriptor of the
1849 hydrogen evolution rate on platinum electrodes, Nature Energy (2017) 2 17031-17037.
1850 [69] M. Alesker, M. Page, M. Shviro, Y. Paska, G. Gershinsky, D.R. Dekel, D. Zitoun,
1851 Palladium/nickel bifunctional electrocatalyst for hydrogen oxidation reaction in
1852 alkaline membrane fuel cell, J. Power Sources 304 (2016) 332-339.
1853 [70] J. Ohyama, T. Sato, A. Satsuma, High performance of Ru nanoparticles supported
1854 on carbon for anode electrocatalyst of alkaline anion exchange membrane fuel cell, J.
1855 Power Sources 225 (2013) 311-315.
1856 [71] S.F. Lu, J. Pan, A.B. Huang, L. Zhuang, J.T. Lu, Alkaline polymer electrolyte fuel
1857 cells completely free from noble metal catalysts, PNAS 105 (2008) 20611-20614.
1858 [72] S.Q. Lu, Z.B. Zhuang, Electrocatalysts for hydrogen oxidation and evolution
1859 reactions, Sci China Mater 59 (2016) 217-238.
1860 [73] H.A. Miller, A. Lavacchi, F. Vizza, M. Marelli, F.D. Benedetto, F. D'Acapito, Y.
1861 Paska, M. Page, D.R. Dekel, A Pd/C-CeO2 anode catalyst for high-performance
1862 platinum-free anion exchange membrane fuel cells, Angew. Chem. Int. Ed. 55 (2016)
1863 6004-6007.
1864 [74] Q.P. Hu, G.W. Li, J. Pan, L.S. Tan, J.T. Lu, L. Zhuang, Alkaline polymer electrolyte
1865 fuel cell with Ni-based anode and Co-based cathode, Int. J. Hydrogen Energy 38 (2013)

16264-16268.

[75] W.C. Sheng, A.P. Bivens, M. Myint, Z.B. Zhuang, R.V. Forest, Q.R. Fang, Ji.G.G. Chen, Y.S. Yan, Non-precious metal electrocatalysts with high activity for hydrogen oxidation reaction in alkaline electrolytes, Energy Environ. Sci. 7 (2014) 1719-1724.

[76] Z.B. Zhuang, S.A. Giles, J. Zhang, G.R. Jenness, S. Caratzoulas, D.G. Vlachos, Y.S. Yan, Nickel supported on nitrogen-doped carbon nanotubes as hydrogen oxidation reaction catalyst in alkaline electrolyte, Nat. Commun. 7 (2016) 10141-10148.

[77] S.M. Alia, B.S. Pivovar, Y.S. Yan, Platinum-coated copper nanowires with high activity for hydrogen oxidation reaction in base, J. Am. Chem. Soc. 135 (2013) 13473-13478.

[78] N.A. Maiorova, A.A. Mikhailova, O.A. Khazova, V.A. Grinberg, Thin-film rotating disk electrode as a tool for comparing the activity of catalysts in the hydrogen oxidation reaction, Russ. J. Electrochem. 42 (2006) 331-338.

[79] C. Gabrielli, P.P. Grand, A. Lasia, H. Perrot, Investigation of hydrogen adsorption and absorption in palladium thin films II. Cyclic voltammetry, J. Electrochem. Soc. 151 (2004) A1937-A1942.

[80] P.N. Bartlett, B. Gollas, S. Guerin, J. Marwan, The preparation and characterisation of H1-e palladium films with a regular hexagonal nanostructure formed by electrochemical deposition from lyotropic liquid crystalline phases, Phys. Chem. Chem.

1885 Phys. 4 (2002) 3835-3842.

1886 [81] M.S. Rau, P.M. Quiano, M.R. Gennero de Chialvo, A.C. Chialvo, Hydrogen

1887 oxidation reaction: Evidences of different electrocatalytic activity between α and β Pd-

1888 H, Electrochem. Commun. 10 (2008) 208-212.

1889 [82] Z.L.A. Feng, E.E. Gabaly, X.F. Ye, Z.X. Shen, W.C. Chueh, Fast vacancy-mediated

1890 oxygen ion incorporation across the ceria-gas electrochemical interface, Nat. Commun.

1891 5 (2014) 4374.

1892 [83] T. Skála, F. Šutara, M. Škoda, K.C. Prince, V. Matolín, Palladium interaction with

1893 CeO2, Sn-Ce-O and Ga-Ce-O layers, J. Phys. Condens. Matter 21 (2009) 055005.

1894 [84] H.A. Miller, F. Vizza, M. Marelli, A. Zadick, L. Dubau, M. Chatenet, S. Geiger, S.

1895 Cherevko, H. Doan, R.K. Pavlicek, S. Mukerjee, D.R. Dekel, Highly active

1896 nanostructured palladium-ceria electrocatalysts for the hydrogen oxidation reaction in

1897 alkaline medium, Nano Energy 33 (2017) 293-305.

1898 [85] N.A. Anastasijevic, V. Vesovic, R.R. Adzic, Determination of the kinetic

1899 parameters of the oxygen reduction reaction using the rotating ring-disk electrode, J.

1900 Electroanal. Chem. 229 (1987) 305-316.

1901 [86] Q.G. He, E.J. Cairns, Review-recent progress in electrocatalysts for oxygen

1902 reduction suitable for alkaline anion exchange membrane fuel cells, J. The

1903 Electrochemical Society 162 (2015) F1504-F1539.

1904 [87] J.R. Varcoe, R.C.T. Slade, G.L. Wright, Y.L. Chen, Steady-state dc and impedance
1905 investigations of H2/O2 alkaline membrane fuel cells with commercial Pt/C, Ag/C, and
1906 Au/C cathodes, J. Phys. Chem. B 110 (2006) 21041-21049.
1907 [88] L.M. Dai, Y.H. Xue, L.T. Qu, H.J. Choi, J.B. Baek, Metal-free catalysts for oxygen
1908 reduction reaction, Chem. Rev. 115 (2015) 4823-4892.
1909 [89] S.D. Poynton, J.P. Kizewski, R.C.T. Slade, J.R. Varcoe, Novel electrolyte
1910 membranes and non-Pt catalysts for low temperature fuel cells, Solid State Ionics 181
1911 (2010) 219-222.
1912 [90] S. Maheswari, G. Selvarani, P. Sridhar, S. Pitchumani, A. Shukla, Oxygen
1913 reduction catalysts for alkaline polymer electrolyte fuel cells, ECS Transactions 33
1914 (2010) 1795-1807.
1915 [91] S. Maheswari, S. Karthikeyan, P. Murugan, P. Sridhar, S. Pitchumani, Carbon-
1916 supported Pd-Co as cathode catalyst for APEMFCs and validation by DFT, Phys. Chem.
1917 Chem. Phys. 14 (2012) 9683-9695.
1918 [92] Q. Zhang, J.X. Feng, A.J. Wang, J. Wei, J.J Feng, Simple synthesis of bimetallic
1919 alloyed Pd-Au nanochain networks supported on reduced graphene oxide for enhanced
1920 oxygen reduction reaction, Rsc Adv. 4 (2014) 52640-52646.
1921 [93] G.T. Fu, Z.Y. Liu, Y. Chen, J. Lin, Y.W. Tang, T.H. Lu, Synthesis and
1922 electrocatalytic activity of Au@Pd core-shell nanothorns for the oxygen reduction

reaction, Nano Res. 7 (2014) 1205-1214.

[94] I. Kruusenberg, L. Matisen, Q. Shah, A.M. Kannan, K. Tammeveski, Non-platinum cathode catalysts for alkaline membrane fuel cells, Int. J. Hydrogen Energy 37 (2012) 4406-4412.

[95] X.G. Li, B.N. Popov, T. Kawahara, H. Yanagi, Non-precious metal catalysts synthesized from precursors of carbon, nitrogen, and transition metal for oxygen reduction in alkaline fuel cells, J. Power Sources 196 (2011) 1717-1722.

[96] P. Song, Y.W. Zhang, J. Pan, L. Zhuang, W.L. Xu, Cheap carbon black-based high-performance electrocatalysts for oxygen reduction reaction, Chem. Commun. 51 (2015) 1972-1975.

[97] Q.G. He, Q. Li, S. Khene, X.M. Ren, F.E. López-Suárez, D. Lozano-Castelló, A. Bueno-López, G. Wu, High-loading cobalt oxide coupled with nitrogen-doped graphene for oxygen reduction in anion-exchange-membrane alkaline fuel cells, J. Phys. Chem. C 117 (2013) 8697-8707.

[98] J. Suntivich, H.A. Gasteiger, N. Yabuuchi, H. Nakanishi, J.B. Goodenough, Y. Shao-Horn, Design principles for oxygen-reduction activity on perovskite oxide catalysts for fuel cells and metal–air batteries, Nature Chemistry 3 (2011) 546-550.

[99] J. Sunarso, A.A.J. Torriero, W. Zhou, P.C. Howlett, M. Forsyth, Oxygen reduction reaction activity of la-based perovskite oxides in alkaline medium: a thin-film rotating

1942 ring-disk electrode study, J. Phys. Chem. C 116 (2012) 5827-5834.

1943 [100] C. Jin, X.C. Cao, L.Y. Zhang, C. Zhang, R.Z. Yang, Preparation and

1944 electrochemical properties of urchin-like $La_{0.8}Sr_{0.2}MnO_3$ perovskite oxide as a

1945 bifunctional catalyst for oxygen reduction and oxygen evolution reaction, J. Power

1946 Sources 241 (2013) 225-230.

1947 [101] K.A. Stoerzinger, M. Risch, J. Suntivich, W.M. Lu, J.G. Zhou, M.D. Biegalski,

1948 H.M. Christen, Ariando, T. Venkatesan, Y. Shao-Horn, Oxygen electrocatalysis on

1949 (001)-oriented manganese perovskite films: Mn valency and charge transfer at the

1950 nanoscale, Energy Environ. Sci. 6 (2013) 1582-1588.

1951 [102] M. Risch, K.A. Stoerzinger, S. Maruyama, W.T. Hong, I. Takeuchi, Y. Shao-Horn,

1952 $La_{0.8}Sr_{0.2}MnO_{3-\delta}$ decorated with $Ba_{0.5}Sr_{0.5}Co_{0.8}Fe_{0.2}O_{3-\delta}$: A bifunctional surface for

1953 oxygen electrocatalysis with enhanced stability and activity, J. Am. Chem. Soc. 136

1954 (2014) 5229-5232.

1955 [103] A. Pendashteh, J. Palma, M. Anderson, R. Marcilla, $NiCoMnO_4$ nanoparticles on

1956 N-doped graphene: Highly efficient bifunctional electrocatalyst for oxygen

1957 reduction/evolution reactions, Applied Catalysis B: Environmental 201 (2017) 241-252.

1958 [104] S. Gupta, W. Kellogg, H. Xu, X.E. Liu, J. Cho, G. Wu, Bifunctional perovskite

1959 oxide catalysts for oxygen reduction and evolution in alkaline media, Chem. Asian J.

1960 11 (2016) 10-21.

[105] Y. Nie, L. Li, Z.D. Wei, Recent advancements in Pt and Pt-free catalysts for oxygen reduction reaction, Chem. Soc. Rev. 44 (2015) 2168-2201.

[106] Y.Q. Zhang, H.B. Tao, J. Liu, Y.F. Sun, J. Chen, B. Hua, T. Thundat, J.L. Luo, A rational design for enhanced oxygen reduction: Strongly coupled silver nanoparticles and engineered perovskite nanofibers, Nano Energy 38 (2017) 392-400.

[107] D.C. Higgins, Z.W. Chen, Nitrogen doped carbon nanotube thin films as efficient oxygen reduction catalyst for alkaline anion exchange membrane fuel cell, ECS Transactions 28 (2010) 63-68.

[108] C.V. Rao, Y. Ishikawa, Activity, selectivity, and anion-exchange membrane fuel cell performance of virtually metal-free nitrogen-doped carbon nanotube electrodes for oxygen reduction reaction, J. Phys. Chem. C 116 (2012) 4340-4346.

[109] W. Ding, Z.D. Wei, S.G. Chen, X.Q. Qi, T. Yang, J.S. Hu, D. Wang, L.J. Wan, S.F. Alvi, L. Li, Space-confinement-induced synthesis of pyridinic- and pyrrolic-nitrogen-doped graphene for the catalysis of oxygen reduction, Angew. Chem. Int. Ed. 52 (2013) 11755-11759.

[110] J.L. Shui, M. Wang, F. Du, L.M. Dai, N-doped carbon nanomaterials are durable catalysts for oxygen reduction reaction in acidic fuel cells, Sci. Adv. 1 (2015) e1400129.

[111] B. Xu, S.S. Hou, G.P. Cao, F. Wu, Y.S. Yang, Sustainable nitrogen-doped porous carbon with high surface areas prepared from gelatin for supercapacitors, J. Mater.

Chem. 22 (2012) 19088-19093.

[112] H.W. Liang, Z.Y. Wu, L.F. Chen, C. Li, S.H. Yu, Bacterial cellulose derived nitrogen-doped carbon nanofiber aerogel: An efficient metal-free oxygen reduction electrocatalyst for zinc-air battery, Nano Energy 11 (2015) 366-376.

[113] Z.J. Lu, M.W. Xu, S.J. Bao, K. Tan, H. Chai, C.J. Cai, C.C. Ji, Q. Zhang, Facile preparation of nitrogen-doped reduced graphene oxide as a metal-free catalyst for oxygen reduction reaction, J. Mater Sci. 48 (2013) 8101-8107.

[114] G. Merle, S.S. Hosseiny, M. Wessling, K. Nijmeijer, New cross-linked PVA based polymer electrolyte membranes for alkaline fuel cells, J. Membrane Science 409-410 (2012) 191-199.

[115] J. Zhang, T.C. Zhou, J.L. Qiao, Y.Y. Liu, J.J. Zhang, Hydroxyl anion conducting membranes poly(vinyl alcohol)/poly(diallyldimethylammonium chloride) for alkaline fuel cellapplications: Effect of molecular weight, Electrochimica Acta 111 (2013) 351-358.

[116] A. Jasti, V.K. Shahi, A facile synthesis of highly stable multiblock poly(arylene ether)s based alkaline membranes for fuel cells, J. Power Sources 267 (2014) 714-722.

[117] X.H. Li, S.S. Cheng, L.C. Wang, Q. Long, J.X. Tao, G.H. Nie, S.J. Liao, Anion exchange membranes by bromination of benzylmethyl-containing poly(arylene ether)s for alkaline membrane fuel cells, RSC Adv. 4 (2014) 29682-29693.

1999 [118] Y.S. Li, T.S. Zhao, W.W. Yang, Measurements of water uptake and transport
2000 properties in anion-exchange membranes, Int. J. Hydrogen Energy 35 (2010) 5656-
2001 5665.
2002 [119] J.L. Qiao, J. Fu, L.L. Liu, J. Zhang, J. Xie, G. Li, Synthesis and properties of
2003 chemically cross-linked poly(vinyl alcohol)–poly(acrylamide-co-
2004 diallyldimethylammonium chloride) (PVA–PAADDA) for anion-exchange membranes,
2005 Solid State Ionics 214 (2012) 6-12.
2006 [120] J.L. Qiao, J. Zhang, J.J. Zhang, Anion conducting poly(vinyl
2007 alcohol)/poly(diallyldimethylammonium chloride) membranes with high durable
2008 alkaline stability for polymer electrolyte membrane fuel cells, J. Power Sources 237
2009 (2013) 1-4.
2010 [121] J. Zhang, J.L. Qiao, G.P. Jiang, L.L. Liu, Y.Y. Liu, Cross-linked poly(vinyl
2011 alcohol)/poly (diallyldimethylammonium chloride) as anion-exchange membrane for
2012 fuel cell applications, J. Power Sources 240 (2013) 359-367.
2013 [122] W.T. Lu, Z.G. Shao, G. Zhang, Y. Zhao, B.L. Yi, Crosslinked poly(vinylbenzyl
2014 chloride) with a macromolecular crosslinker for anion exchange membrane fuel cells,
2015 J. Power Sources 248 (2014) 905-914.
2016 [123] M. Tanaka, K. Fukasawa, E. Nishino, S. Yamaguchi, K. Yamada, H. Tanaka, B.
2017 Bae, K. Miyatake, M. Watanabe, Anion conductive block poly(arylene ether)s:

2018 synthesis, properties, and application in alkaline fuel cells, J. Am. Chem. Soc. 133 (2011)
2019 10646-10654.
2020 [124] A.L. Ong, S. Saad, R. Lan, R.J. Goodfellow, S.W. Tao, Anionic membrane and
2021 ionomer based on poly(2,6-dimethyl-1,4-phenylene oxide) for alkaline membrane fuel
2022 cells, J. Power Sources 196 (2011) 8272-8279.
2023 [125] X.C. Lin, L. Wu, Y.B. Liu, A.L. Ong, S.D. Poynton, J.R. Varcoe, T.W. Xu, Alkali
2024 resistant and conductive guanidinium-based anion-exchange membranes for alkaline
2025 polymer electrolyte fuel cells, J. Power Sources 217 (2012) 373-380.
2026 [126] X.C. Lin, X.H. Liang, S.D. Poynton, J.R. Varcoe, A.L. Ong, J. Ran, Y. Li, Q.H.
2027 Li, T.W. Xu, Novel alkaline anion exchange membranes containing pendant
2028 benzimidazolium groups for alkaline fuel cells, J. Membrane Science 443 (2013) 193-
2029 200.
2030 [127] X.C. Lin, J.R. Varcoe, S.D. Poynton, X.H. Liang, A.L. Ong, J. Ran, Y. Li, T.W.
2031 Xu, Alkaline polymer electrolytes containing pendant dimethylimidazolium groups for
2032 alkaline membrane fuel cells, J. Mater. Chem. A 1 (2013) 7262-7269.
2033 [128] N.W. Li, M.D. Guiver, W.H. Binder, Towards high conductivity in anion-
2034 exchange membranes for alkaline fuel cells, ChemSusChem 6 (2013) 1376-1383.
2035 [129] H.S. Dang, P. Jannasch, A comparative study of anion-exchange membranes
2036 tethered with different hetero-cycloaliphatic quaternary ammonium hydroxides, J.

2037 Mater. Chem. A 5 (2017) 21965-21978.

2038 [130] X.J. Wang, P. Wang, Y.Y. Sun, J.L. Wang, H.G. Fang, S.Z. Yang, H.B. Wei, Y.S.

2039 Ding, A mechanically strong and tough anion exchange membrane engineered with

2040 non-covalent modalities, Chem. Commun. 53 (2017) 12369-12372.

2041 [131] N. Benipal, J. Qi, J.C. Gentile, W.Z. Li, Direct glycerol fuel cell with

2042 polytetrafluoroethylene (PTFE) thin film separator, Renewable Energy 105 (2017) 647-

2043 655.

2044 [132] Y. Zhao, H.M. Yu, D.L. Yang, J. Li, Z.G. Shao, B.L. Yi, High-performance

2045 alkaline fuel cells using crosslinked composite anion exchange membrane, J. Power

2046 Sources 221 (2013) 247-251.

2047 [133] Y. Zhao, J. Pan, H.M. Yu, D.L. Yang, J. Li, L. Zhuang, Z.G. Shao, B.L. Yi,

2048 Quaternary ammonia polysulfone-PTFE composite alkaline anion exchange membrane

2049 for fuel cells application, Int. J. Hydrogen Energy 38 (2013) 1983-1987.

2050 [134] G.W. Li, J. Pan, J.J. Han, C. Chen, J.T. Lu, L. Zhuang, Ultrathin composite

2051 membrane of alkaline polymer electrolyte for fuel cell applications, J. Mater. Chem. A

2052 1 (2013) 12497-12502.

2053 [135] J.F. Zhou, M. Unlu, J.A. Vega, P.A. Kohl, Anionic polysulfone ionomers and

2054 membranes containing fluorenyl groups for anionic fuel cells, J. Power Sources 190

2055 (2009) 285-292.

2056 [136] Y.Q. Yang, J. Wang, J.F. Zheng, S.H. Li, S.B. Zhang, A stable anion exchange
2057 membrane based on imidazolium salt for alkaline fuel cell, J. Membrane Science 467
2058 (2014) 48-55.
2059 [137] X.H. Li, J.X. Tao, G.H. Nie, L.C. Wang, L.H. Li, S.J. Liao, Cross-linked
2060 multiblock copoly(arylene ether sulfone) ionomer/nano-ZrO2 composite anion
2061 exchange membranes for alkaline fuel cells, RSC Adv. 4 (2014) 41398-41410.
2062 [138] X.H. Zhang, S.W. Tay, Z.L. Liu, L. Hong, Alkaline anion-exchange polymer
2063 membrane with grid-plug microstructure for hydrogen fuel cell application, J. Power
2064 Sources 196 (2011) 5494-5498.
2065 [139] S.S. He, C.W. Frank, Facilitating hydroxide transport in anion exchange
2066 membranes via hydrophilic grafts, J. Mater. Chem. A 2 (2014) 16489-16497.
2067 [140] R. Vinodh, M. Purushothaman, D. Sangeetha, Novel quaternized
2068 polysulfone/ZrO_2 composite membranes for solid alkaline fuel cell applications, Int. J.
2069 Hydrogen Energy 36 (2011) 7291-7302.
2070 [141] J.R. Varcoe, R.C.T. Slade, E.L.H. Yee, An alkaline polymer electrochemical
2071 interface: a breakthrough in application of alkaline anion-exchange membranes in fuel
2072 cells, Chem. Commun. 13 (2006) 1428-1429.
2073 [142] J. Pan, Y. Li, L. Zhuang, J.T. Lu, Self-crosslinked alkaline polymer electrolyte
2074 exceptionally stable at 90℃, Chem. Commun. 46 (2010) 8597-8599.

2075 [143] J. Zhou, J.S. Guo, D. Chu, R.R. Chen, Impacts of anion-exchange-membranes
2076 with various ionic exchange capacities on the performance of H2/O2 fuel cells, J. Power
2077 Sources 219 (2012) 272-279.
2078 [144] N. Li, Y. Leng, M.A. Hickner, C.Y. Wang, Highly stable, anion conductive, comb-
2079 shaped copolymers for alkaline fuel cells, J. Am. Chem. Soc. 135 (2013) 10124-10133.
2080 [145] X.M. Ren, S.C. Price, A.C. Jackson, N. Pomerantz, F.L. Beyer, Highly conductive
2081 anion exchange membrane for high power density fuel-cell performance, ACS Appl.
2082 Mater. Interfaces 6 (2014) 13330-13333.
2083 [146] W.T. Lu, Z.G. Shao, G. Zhang, Y. Zhao, J. Li, B.L. Yi, Preparation and
2084 characterization of imidazoliumfunctionalized poly (ether sulfone) as anion exchange
2085 membrane and ionomer for fuel cell application, Int. J. Hydrogen Energy 38 (2013)
2086 9285-9296.
2087 [147] F.X. Zhang, H.M. Zhang, C. Qu, Imidazolium functionalized polysulfone anion
2088 exchange membrane for fuel cell application, J. Mater. Chem. 21 (2011) 12744-12752.
2089 [148] J. Ran, L. Wu, J.R. Varcoe, A.L. Ong, S.D. Poynton, T.W. Xu, Development of
2090 imidazolium-type alkaline anion exchange membranes for fuel cell application, J.
2091 Membrane Science 415-416 (2012) 242-249.
2092 [149] B. Xing, O. Savadogo, Hydrogenroxygen polymer electrolyte membrane fuel
2093 cells (PEMFCs) based on alkaline-doped polybenzimidazole (PBI), Electrochemistry

2094 Communications 2 (2000) 697-702.

2095 [150] S. Li, X.L. Zhu, D.Z. Liu, F. Sun, A highly durable long side-chain

2096 polybenzimidazole anion exchange membrane for AEMFC, J. Membrane Science 546

2097 (2018) 15-21.

2098 [151] Y. Wan, K.A.M. Creber, B. Peppley, V.T. Bui, E. Halliop, New solid polymer

2099 electrolyte membranes for alkaline fuel cells, Polym. Int. 54 (3005) 5-10.

2100 [152] Y. Wan, B. Peppley, K.A.M. Creber, V.T. Bui, E. Halliop, Preliminary evaluation

2101 of an alkaline chitosan-based membrane fuel cell, J. Power Sources 162 (2006) 105-

2102 113.

2103 [153] Y.T. Luo, J.C. Guo, C.S. Wang, D. Chu, Quaternized poly(methyl methacrylate-

2104 co-butyl acrylate-co-vinylbenzyl chloride) membrane for alkaline fuel cells, J. Power

2105 Sources 195 (2010) 3765-3771.

2106 [154] Y.T. Luo, J.C. Guo, C.S. Wang, D. Chu, An acrylate-polymer-based electrolyte

2107 membrane for alkaline fuel cell applications, ChemSusChem 4 (2011) 1557-1560.

2108 [155] Y. Luo, J. Guo, C. Wang, K.Y. Choi, D. Chu, High molecular weight copolymer

2109 alkaline fuel cell membrane via miniemulsion polymerization, ECS Transactions 33

2110 (2010) 1893-1902.

2111 [156] Y.T. Luo, J.C. Guo, C.S. Wang, D. Chu, Tunable high-molecular-weight anion-

2112 exchange membranes for alkaline fuel cells, Macromol. Chem. Phys. 212 (20110 2094-

2102.

[157] G.M. Wu, S.J. Lin, C.C. Yang, Preparation and characterization of high ionic conducting alkaline non-woven membranes by sulfonation, J. Membrane Science 284 (2006) 120-127.

[158] C. Sollogouba, A. Guinault, C. Bonnebat, M. Bennjima, L. Akrour, J.F. Fauvarque, L. Ogier, Formation and characterization of crosslinked membranes for alkaline fuel cells, J. Membrane Science 335 (2009) 37-42.

[159] T. Hibino, Y. Shen, M. Nishida, M. Nagao, Hydroxide ion conducting antimony(v)-doped tin pyrophosphate electrolyte for intermediate-temperature alkaline fuel cells, Angew. Chem. Int. Ed. 51 (2012) 10786-10790.

[160] T. Hibino, K. Kobayashi, An intermediate-temperature alkaline fuel cell using an $Sn_{0.92}Sb_{0.08}P_2O_7$-based hydroxide-ion-conducting electrolyte and electrodes, J. Mater. Chem. A 1 (2013) 1134-1140.

[161] Y. Zhao, H.M. Yu, F. Xie, Y.X. Liu, Z.G. Shao, B.L. Yi, High durability and hydroxide ion conducting pore-filled anion exchange membranes for alkaline fuel cell applications, J. Power Sources 269 (2014) 1-6.

[162] D.S. Kim, C.H. Fujimoto, M.R. Hibbs, A. Labouriau, Y.K. Choe, Y.S. Kim, Resonance stabilized perfluorinated ionomers for alkaline membrane fuel cells, Macromolecules 46 (2013) 7826-7833.

2132 [163] Y.N. Chen, Z.M. Li, N.J. Chen, R. Li, Y.J. Zhang, K. Li, F.H. Wang, H. Zhu, A
2133 new method for improving the conductivity of alkaline membrane by incorporating
2134 TiO_2- ionic liquid composite particles, Electrochimica Acta 255 (2017) 335-346.
2135 [164] B.R. Einsla, S. Chempath, L.R. Pratt, J.M. Boncella, J. Rau, C. Macomber, B.S.
2136 Pivovar, Stability of cations for anion exchange membrane fuel cells, ECS Transactions
2137 11 (2007) 1173-1180.
2138 [165] C.G. Arges, J. Parrondo, G. Johnson, A. Nadhan, V. Ramani, Assessing the
2139 influence of different cation chemistries on ionic conductivity and alkaline stability of
2140 anion exchange membranes, J. Mater. Chem. 22 (2012) 3733-3744.
2141 [166] J.S. Park, S.H. Park, S.D. Yim, Y.G. Yoon, W.Y. Lee, C.S. Kim, Performance of
2142 solid alkaline fuel cells employing anion-exchange membranes, J. Power Sources 178
2143 (2008) 620-626.
2144 [167] G.G. Wang, Y.M. Weng, J. Zhao, D. Chu, D. Xie, R.R. Chen, Developing a novel
2145 alkaline anion exchange membrane derived from poly(ether-imide) for improved ionic
2146 conductivity, Polym. Adv. Technol. 21 (2010) 554-560.
2147 [168] Y.T. Luo, J.C. Guo, Y.H. Liu, Q. Shao, C.S. Wang, D. Chu, Copolymerization of
2148 methyl methacrylate and vinylbenzyl chloride towards alkaline anion exchange
2149 membrane for fuel cell applications, J. Membrane Science 423-424 (2012) 209-214.
2150 [169] J. Pan, C. Chen, L. Zhuang, J.T. Lu, Designing advanced alkaline polymer

2151 electrolytes for fuel cell applications, Accounts of Chemical Research 45 (2012) 473-
2152 481.
2153 [170] W. Li, J. Fang, M. Lv, C.X. Chen, X.J. Chi, Y.X. Yang, Y.M. Zhang, Novel anion
2154 exchange membranes based on polymerizable imidazolium salt for alkaline fuel cell
2155 applications, J. Mater. Chem. 21 (2011) 11340-11346.
2156 [171] M. Mamlouk, K. Scott, Effect of anion functional groups on the conductivity and
2157 performance of anion exchange polymer membrane fuel cells, J. Power Sources 211
2158 (2012) 140-146.
2159 [172] R.Z. Jiang, D. Chu, An air-breathing H_2/air cell design suitable for fast screening
2160 of electrolytes, Electrochimica Acta 56 (2011) 8365-8370.
2161 [173] J.L. Yan, M.A. Hickner, Anion exchange membranes by bromination of
2162 benzylmethyl-containing poly(sulfone)s, Macromolecules 43 (2010) 2349-2356.
2163 [174] J.F. Zhou, M. Ünlü, J.A. Vega, P.A. Kohl, Anionic polysulfone ionomers and
2164 membranes containing fluorenyl groups for anionic fuel cells, J. Power Sources 190
2165 (2009) 285-292.
2166 [175] K. Fukuta, H. Inoue, S. Watanabe, H. Yanagi, In-situ observation of CO2 through
2167 the self-purging in alkaline membrane fuel cell (AMFC), ECS Transactions 19 (2009)
2168 23-27.
2169 [176] J.A. Vega, S. Smith, C. Chartier, W.E. Mustain, Effect of carbonate on anion

2170 exchange membrane conductivity and hydrogen oxidation for AAEMFCs, ECS
2171 Transactions 28 (2010) 103-109.
2172 [177] J.A. Vega, C. Chartier, S. Smith, W.E. Mustain, Effect of carbonate on oxygen
2173 reduction, hydrogen oxidation and anion exchange membrane chemical stability, ECS
2174 Transactions 33 (2010) 1735-1749.
2175 [178] J.A. Vega, W.E. Mustain, Effect of CO2, HCO3- and CO3-2 on oxygen reduction
2176 in anion exchange membrane fuel cells, Electrochimica Acta 55 (2010) 1638-1644.
2177 [179] J.A. Vega, C. Chartier, W.E. Mustain, Effect of hydroxide and carbonate alkaline
2178 media on anion exchange membranes, J. Power Sources 195 (2010) 7176-7180.
2179 [180] M. Inaba, Y. Matsui, M. Saito, A. Tasaka, K. Fukuta, S. Watanabe, H. Yanagi,
2180 Effects of carbon dioxide on the performance of anion-exchange membrane fuel cells,
2181 Electrochemistry 79 (2011) 322-325.
2182 [181] Y. Matsui, M. Saito, A. Tasaka, M. Inaba, Influence of carbon dioxide on the
2183 performance of anion-exchange membrane fuel cells, ECS Transactions 25 (2010) 105-
2184 110.
2185 [182] S. Suzuki, H. Muroyama, T. Matsui, K. Eguchi, Influence of CO2 dissolution into
2186 anion exchange membrane on fuel cell performance, Electrochimica Acta 88 (2013)
2187 552-558.
2188 [183] L. Gubler, Polymer design strategies for radiation-grafted fuel cell membranes,

2189 Adv. Energy Mater. 4 (2014) 1300827.

2190 [184] M.M. Nasef, Radiation-grafted membranes for polymer electrolyte fuel cells:

2191 current trends and future directions, Chem. Rev. 114 (2014) 12278-12329.

2192 [185] J.R. Varcoe, R.C.T. Slade, An electron-beam-grafted ETFE alkaline anion-

2193 exchange membrane in metal-cation-free solid-state alkaline fuel cells,

2194 Electrochemistry Communications 8 (2006) 839-843.

2195 [186] S.D. Poynton, J.P. Kizewski, R.C.T. Slade, J.R. Varcoe, Novel electrolyte

2196 membranes and non-Pt catalysts for low temperature fuel cells, Solid State Ionics 181

2197 (2010) 219-222.

2198 [187] V.M. Nikolic, D.L. Zugic, A.D. Maksic, D.P. Saponjic, M.P.M. Kaninski,

2199 Performance comparison of modified poly(vinyl alcohol) based membranes in alkaline

2200 fuel cells, Int. J. Hydrogen Energy 36 (2011) 11004-11010.

2201 [188] O.I. Deavin, S. Murphy, A.L. Ong, S.D. Poynton, R. Zeng, H. Herman, J.R.

2202 Varcoe, Anion-exchange membranes for alkaline polymer electrolyte fuel cells:

2203 comparison of pendent benzyltrimethylammonium- and benzylmethylimidazolium-

2204 head-groups, Energy Environ. Sci. 5 (2012) 8584-8597.

2205 [189] J. Fang, Y.X. Yang, X.H. Lu, M.L. Ye, W. Li, Y.M. Zhang, Cross-linked, ETFE-

2206 derived and radiation grafted membranes for anion exchange membrane fuel cell

2207 applications, Int. J. Hydrogen Energy 37 (2012) 594-602.

2208 [190] L.Q. Wang, E. Magliocca, E.L. Cunningham, W.E. Mustain, S.D. Poynton, R.
2209 Escudero-Cid, M.M. Nasef, J. Ponce-González, R. Bance-Souahli, R.C.T. Slade, D.K.
2210 Whelligan, J.R. Varcoe, An optimised synthesis of high performance radiation-grafted
2211 anion-exchange membranes, Green Chem. 19 (2017) 831-843.
2212 [191] L.Q. Wang, J.J. Brink, Y. Liu, A.M. Herring, J. Ponce-González, D.K. Whelligan,
2213 J.R. Varcoe, Non-fluorinated pre-irradiation-grafted (peroxidated) LDPE-based anion-
2214 exchange membranes with high performance and stability, Energy Environ. Sci. 2017.
2215 [192] L. Sun, J.S. Guo, J. Zhou, Q.M. Xu, D. Chu, R.R. Chen, Novel nanostructured
2216 high-performance anion exchange ionomers for anion exchange membrane fuel cells,
2217 J. Power Sources 202 (2012) 70-77.
2218 [193] K. Matsumoto, T. Fujigaya, H. Yanagi, N. Nakashima, Very high performance
2219 alkali anion-exchange membrane fuel cells, Adv. Funct. Mater. 21 (2011) 1089-1094.
2220 [194] D.L. Yang, H.M. Yu, G.F. Li, Y. Zhao, Y.X. Liu, C.K. Zhang, W. Song, Z.G. Shao,
2221 Fine microstructure of high performance electrode in alkaline anion exchange
2222 membrane fuel cells, J. Power Sources 267 (2014) 39-47.
2223 [195] S. J. Ewing, R. Lan, X. X. Xu, S.W. Tao, Synthesis of dendritic nano-sized nickel
2224 for use as anodematerial in an alkaline membrane fuel cell, Fuel Cells 10 (2010) 72-76.
2225 [196] A. Kucernak, F. Bidault, G. Smith, Membrane electrode assemblies based on
2226 porous silver electrodes for alkaline anion exchange membrane fuel cells,

2227 Electrochimica Acta 82 (2012) 284-290.

2228 [197] M. Ünlü, J.F. Zhou, I. Anestis-Richard, P.A. Kohl, Characterization of anion

2229 exchange ionomers in hybrid polymer electrolyte fuel cells, ChemSusChem 3 (2010)

2230 1398-1402.

2231 [198] S. Gu, W.C. Sheng, R. Cai, S.M. Alia, S.Q. Song, K.O. Jensen, Y.S. Yan, An

2232 efficient Ag-ionomer interface for hydroxide exchange membrane fuel cells, Chem.

2233 Commun. 49 (2013) 131-134.

2234 [199] M. Ünlü, J.F. Zhou, I. Anestis-Richard, H. Kim, P.A. Kohl, Improved gas

2235 diffusion electrodes for hybrid polymer electrolyte fuel cells, Electrochimica Acta 56

2236 (2011) 4439-4444.

2237 [200] J.F. Zhou, M. Ünlü, I. Anestis-Richard, H. Kim, P.A. Kohl, Solvent processible,

2238 high-performance partially fluorinated copoly(arylene ether) alkaline ionomers for

2239 alkaline electrodes, J. Power Sources 196 (2011) 7924-7930.

2240 [201] D. Kubo, K. Tadanaga, A. Hayashi, M. Tatsumisago, Improvement of

2241 electrochemical performance in alkaline fuel cell by hydroxide ion conducting Ni-Al

2242 layered double hydroxide, J. Power Sources 222 (2013) 493-497.

2243 [202] C. Tamain, S.D. Poynton, R.C.T. Slade, B. Carroll, J.R. Varcoe, Development of

2244 cathode architectures customized for H2/O2 metal-cation-free alkaline membrane fuel

2245 cells, J. Phys. Chem. C 111 (2007) 18423-18430.

2246 [203] M. Mamlouk, K. Scott, J.A. Horsfall, C. Williams, The effect of electrode
2247 parameters on the performance of anion exchange polymer membrane fuel cells, Int. J.
2248 Hydrogen Energy 36 (2011) 7191-7198.
2249 [204] Y. Oshiba, J. Hiura, Y. Suzuki, T. Yamaguchi, Improvement in the solid-state
2250 alkaline fuel cell performance through efficient water management strategies, J. Power
2251 Sources 345 (2017) 221-226.
2252 [205] T.J. Omasta, L. Wang, X. Peng, C.A. Lewis, J.R. Varcoe, W.E. Mustain,
2253 Importance of balancing membrane and electrode water in anion exchange membrane
2254 fuel cells, J. Power Sources xxx (2017) 1-9.
2255 [206] R.C.T. Slade, J.P. Kizewski, S.D. Poynton, R. Zeng, J.R. Varcoe, Fuel Cells:
2256 Selected Entries from the Encyclopedia of Sustainability Science, Springer, 2012
2257 (Chapter 2).
2258 [207] Y.T. Luo, J.C. Guo, C.S. Wang, D. Chu, Fuel cell durability enhancement by
2259 crosslinking alkaline anion exchange membrane electrolyte, Electrochemistry
2260 Communications 16 (2012) 65-68.
2261 [208] C. Fujimoto, D.S. Kim, M. Hibbs, D. Wrobleski, Y.S. Kim, Backbone stability of
2262 quaternized polyaromatics for alkaline membrane fuel cells, J. Membrane Science 423-
2263 424 (2012) 438-449.
2264 [209] M. Carmo, G. Doubek, R. C. Sekol, M. Linardi, A.D. Taylor, Development and

2265 electrochemical studies of membrane electrode assemblies for polymer electrolyte
2266 alkaline fuel cells using FAA membrane and ionomer, J. Power Sources 230 (2013)
2267 169-175.
2268 [210] Y. Wang, G.W. Wang, G.W. Li, B. Huang, J. Pan, Q. Liu, J.J. Han, L. Xiao, J.T.
2269 Lu, L. Zhuang, Pt–Ru catalyzed hydrogen oxidation in alkaline media: oxophilic effect
2270 or electronic effect?, Energy Environ. Sci. 8 (2014) 177-181.
2271 [211] M. Ünlü, J.F. Zhou, P.A. Kohl, Hybrid polymer electrolyte fuel cells: alkaline
2272 electrodes with proton conducting membrane, Angew. Chem. Int. Ed. 49 (2010) 1299-
2273 1301.
2274 [212] W.D. Shen, F.Y. Zhang, A. Prasad, J. Hertz, Non-flooding hybrid polymer fuel
2275 cell, ECS Transactions 33 (2010) 2011-2016.
2276 [213] X.Q. Zhang, J.C. Chen, Maximum equivalent power output and performance
2277 optimization analysis of an alkaline fuel cell/heat-driven cycle hybrid system, J. Power
2278 Sources 196 (2011) 10088-10093.
2279 [214] M. Ünlü, J.F. Zhou, P.A. Kohl, Hybrid anion and proton exchange membrane fuel
2280 cells, J. Phys. Chem. C 113 (2009) 11416-11423.
2281 [215] M. Ünlü, J.F. Zhou, P.A. Kohl, Self-humidifying hybrid anion-cation membrane
2282 fuel cell operated under dry conditions, Fuel Cells 10 (2010) 54-63.
2283 [216] K. Fukuta, H. Inoue, Y. Chikashige, H. Yanagi, Improved maximum power

density of alkaline membrane fuel cells (AMFCs) by the optimization of mea construction, ECS Transactions 28 (2010) 221-225.

[217] J.W.D Ng, Y. Gorlin, T. Hatsukade, T.F. Jaramillo, A precious-metal-free regenerative fuel cell for storing renewable electricity, Adv. Energy Mater. 3 (2013) 1545-1550.

[218] J.W.D. Ng, M. Tang, T.F. Jaramillo, A carbon-free, precious-metal-free, high performance O2 electrode for regenerative fuel cells and metal-air batteries, Energy Environ. Sci. 7 (2014) 2017-2024.

[219] X. Wu, K. Scott, A non-precious metal bifunctional oxygen electrode for alkaline anion exchange membrane cells, J. Power Sources 206 (2012) 14-19.

[220] H. Matsushima, W. Majima, Y. Fukunaka, Three-phase interfacial phenomena in alkaline unitized regenerative fuel cell, Electrochimica Acta 114 (2013) 509-513.

[221] K.N. Grew, W.K.S. Chiu, A dusty fluid model for predicting hydroxyl anion conductivity in alkaline anion exchange membranes, J. The Electrochemical Society 157 (2010) B327-B337.

[222] Z. Siroma, S. Watanabe, K. Yasuda, K. Fukuta, H. Yanagib, Mathematical modeling of the concentration profile of carbonate ions in an anion exchange membrane fuel cell, J. The Electrochemical Society 158 (2011) B682-B689.

[223] K. Jiao, P. He, Q. Du, Y. Yin, Three-dimensional multiphase modeling of alkaline

anion exchange membrane fuel cell, Int. J. Hydrogen Energy 39 (2014) 5981-5995.

[224] H. Deng, J.X. Chen, K. Jiao, X.R. Huang, An analytical model for alkaline membrane direct methanol fuel cell, Int. J. Heat and Mass Transfer 74 (2014) 376-390.

[225] Z.L.A. Feng, E.E. Gabaly, X.F. Ye, Z.X. Shen, W.C. Chueh, Fast vacancy-mediated oxygen ion incorporation across the ceria-gas electrochemical interface, Nat. Commun. 5 (2014) 4374.

[226] H. Deng, D.W. Wang, X. Xie, Y.B. Zhou, Y. Yin, Q. Du, K. Jiao, Modeling of hydrogen alkaline membrane fuel cell with interfacial effect and water management optimization, Renewable Energy 91 (2016) 166-177.

[227] S. Huo, H. Deng, Y.F. Chang, K. Jiao, Water management in alkaline anion exchange membrane fuel cell anode, Int. J. Hydrogen Energy 37 (2012) 18389-18402.

[228] H.S. Shiau, I.V. Zenyuk, A.Z. Weber, Water management in an alkaline-exchange-membrane fuel cell, ECS Transactions 69 (2015) 985-994.

[229] H. Deng, D.W. Wang, R.F. Wang, X. Xie, Y. Yin, Q. Du, K. Jiao, Effect of electrode design and operating condition on performance of hydrogen alkaline membrane fuel cell, Applied Energy 183 (2016) 1272-1278.

[230] S. Huo, J.W. Park, P. Hu, D.W. Wang, K. Jiao, Analytical modeling of liquid saturation jump effect for hydrogen alkaline anion exchange membrane fuel cell, Int. J. Heat and Mass Transfer 112 (2017) 891-902.

[231] Z.Q. Niu, K. Jiao, F. Zhang, Q. Du, Y. Yin, Direct numerical simulation of two-phase turbulent flow in fuel cell flow channel, Int. J. hydrogen energy 41 (2016) 3147-3152.

[232] Z.Q. Niu, R.F. Wang, K. Jiao, Q. Du, Y. Yin, Direct numerical simulation of low Reynolds number turbulent air-water transport in fuel cell flow channel, Science Bulletin 62 (2017) 31-39.

[233] D.P. Tang, J. Pan, S.F. Lu, L. Zhuang, J.T. Lu, Alkaline polymer electrolyte fuel cells: Principle, challenges, and recent progress, Sci China Chem 53 (2010) 357-164.

[234] R. Zeng, J. Handsel, S.D. Poynton, A.J. Roberts, R.C.T. Slade, H. Herman, D.C. Apperley, J.R. Varcoe, Alkaline ionomer with tuneable water uptakes for electrochemical energy technologies, Energy Environ. Sci. 4 (2011) 4925-4928.

Table captions:

Table 1 Selected hydrogen/oxygen fuel cell performance with different HOR electrocatalysts reported in open literature.

Table 2 Selected hydrogen/oxygen fuel cell performance with different ORR electrocatalysts reported in open literature.

Table 3 Selected hydrogen/oxygen fuel cell performance with different AAEMs reported in open literature.

Table 4 Selected hydrogen/oxygen fuel cell performance with different MEA structures reported in open literature.

Figure captions:

Figure 1. Schematic of a typical alkaline anion exchange membrane fuel cell (AAEMFC).

Figure 2. AFM images of the Pd/Ni surfaces and size distribution of the grains observed for (A) 17% Pd coverage and (B) 35% Pd coverage [53]. Reproduced with permission from Elsevier.

Figure 3. (a) General scheme of oxygen reduction reaction. [85]. Reproduced with permission from Elsevier. (b) Modified form of Pourbaix diagram [86]. Reproduced with permission from The Electrochemical Society.

Figure 4. (a) Schematic of cathode side in the MEA using Ag/C as a catalyst [55]. Reproduced with permission from Springer. (b) Optimal structure of rGO(N)-Co(II)-

2360 O-Co(II)-rGO(N) [97]. (c) ORR current densities of thin film of (I) $LaNiO_3$, $LaCoO_3$,

2361 $LaFeO_3$, $LaMnO_3$, and $LaCrO_3$ and (II) $LaNi_{0.5}Co_{0.5}O_3$, $LaNi_{0.5}Fe_{0.5}O_3$, $LaNi_{0.5}Mn_{0.5}O_3$,

2362 and $LaNi_{0.5}Cr_{0.5}O_3$. (III) (IV) Magnified portion to pinpoint the onset ORR potentials

2363 on panels I and II, respectively. Reproduced with permission from American Chemical

2364 Society [99]. (d) Schematic of the selectivity inside and outside of MMT during NG

2365 synthesis [109]. Reproduced with permission from Wiley.

2366 Figure 5. Effect of (a) the temperature and (b) the time on ionic conductivity [114].

2367 Reproduced with permission from Elsevier.

2368 Figure 6. Schematic of (a) an air-breathing cell and (b) the electrode configuration [172].

2369 Reproduced with permission from Elsevier.

2370 Figure 7. Schematic of (a) the preparation of the MWNT/PyPBI/Pt samples and (b)

2371 TEM image of the MWNT/PyPBI/Pt [193]. Reproduced with permission from Wiley.

2372 Figure 8. Schematic of the electrode structures made by (a) thin-film and (b) ionomer

2373 impregnation methods [199]. Reproduced with permission from Elsevier.

2374 Figure 9. (a) Durability tests of uncrosslinked QPMV and 10% crosslinked QPMV-

2375 PDVB AAEMs at 70ºC, (b) Durability test of 10% crosslinked AAEM at 50ºC [207].

2376 Reproduced with permission from Elsevier. (c) Cell performance of the AAEMFC

2377 using the PtRu anode or Pt anode [210]. Reproduced with permission from The Royal

2378 Society of Chemistry. (d) Performance of H_2/O_2 AAEMFC test data at 60 °C for E-R

(squares) and E-6 (circles) using PtRu/C anodes and Pt/C cathodes and with no gas back-pressurization of the fully humidified gases [190]. (e) Performance of the AAEMFC with different hypothesized distribution of water across the AAEM and electrodes in an AAEMFC [205]. (f) Performance of H_2/O_2 AAEMFC at 80°C with the LDPE-AAEM with Pt/C (circles) or Ag/C (squares) as cathodes as well as PtRu/C anode [191]. Reproduced with permission from Elsevier.

Figure 10. (a) Schematic of a hybrid fuel cell comprising high pH AAEM electrodes and a PEM [211]. Reproduced with permission from Wiley. (b) Schematic of an AFC/heat-driven cycle hybrid system [213]. Reproduced with permission from Elsevier. (c) Schematic of the depletion region at the junction of the AAEM and PEM in contact [214]. Reproduced with permission from American Chemical Society. (d) Schematic of hybrid fuel cells comprising low pH anode/high pH cathode [215]. Reproduced with permission from Wiley.

Figure 11. Schematic of an AAEM-URFC as an energy storage device for grid applications [217]. Reproduced with permission from Wiley.

Figure 12. (a) Distributions of liquid water in anode catalyst layer and gas diffusion layer at different current densities [227]. (b) Effect of MPL configurations on (I) cell voltage and power density and (II) activation and ohmic overpotential with 100% cathode inlet humidification [230]. (c) Phase boundary of the water droplet in the DNS

model of turbulent two-phase flow at different time instances [231]. (d) Iso-surface of the water phase fraction for two-droplet case and three-droplet case at different time instances [232]. Reproduced with permission from Elsevier.

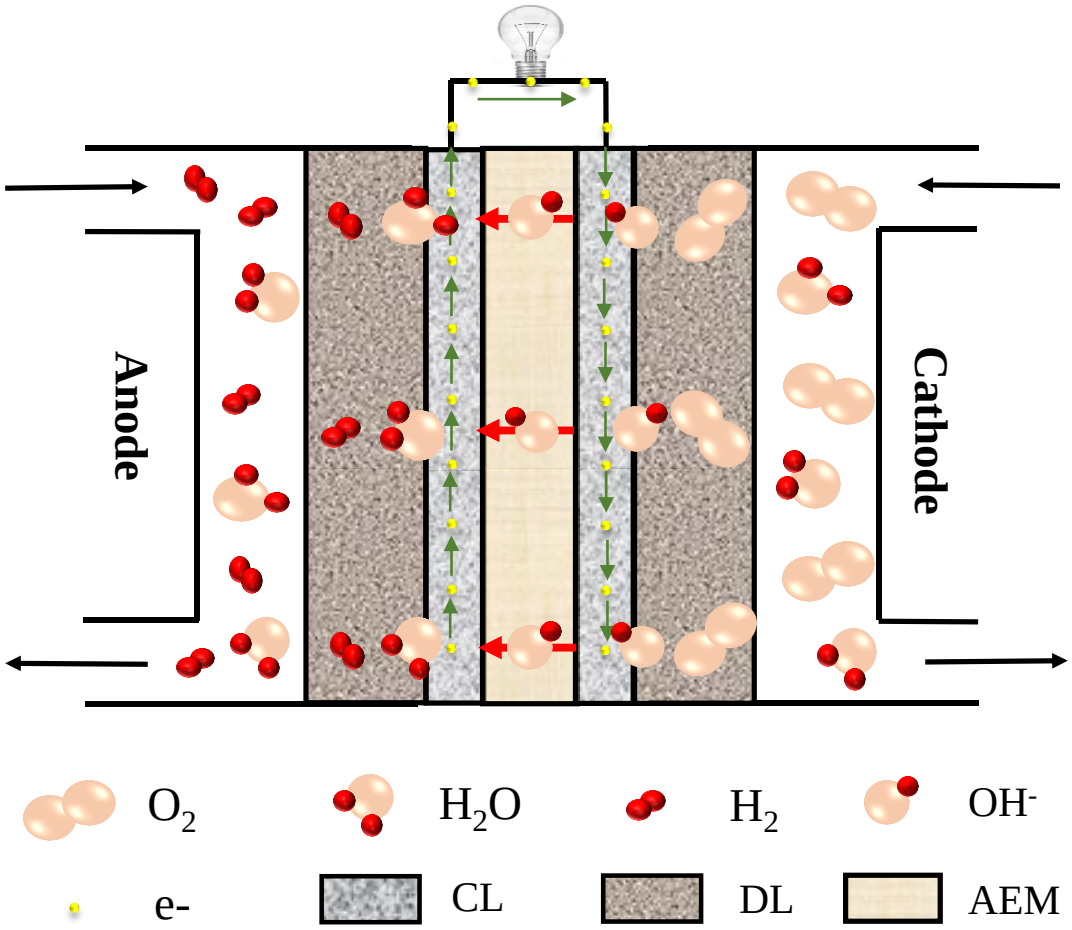

Figure 1. Schematic of a typical alkaline anion exchange membrane fuel cell (AAEMFC).

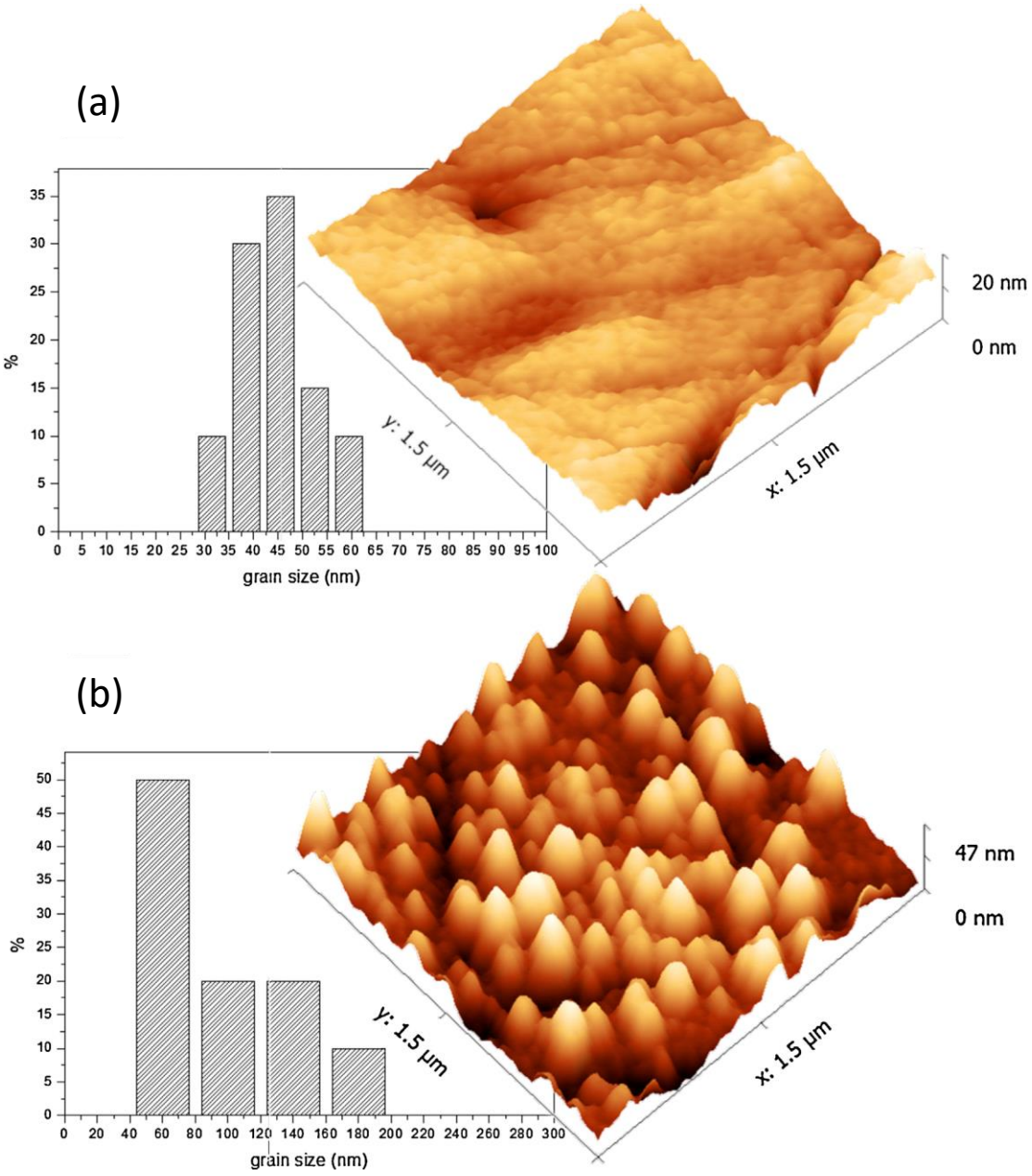

Figure 2. AFM images of the Pd/Ni surfaces and size distribution of the grains observed for (A) 17% Pd coverage and (B) 35% Pd coverage [53]. Reproduced with permission from Elsevier.

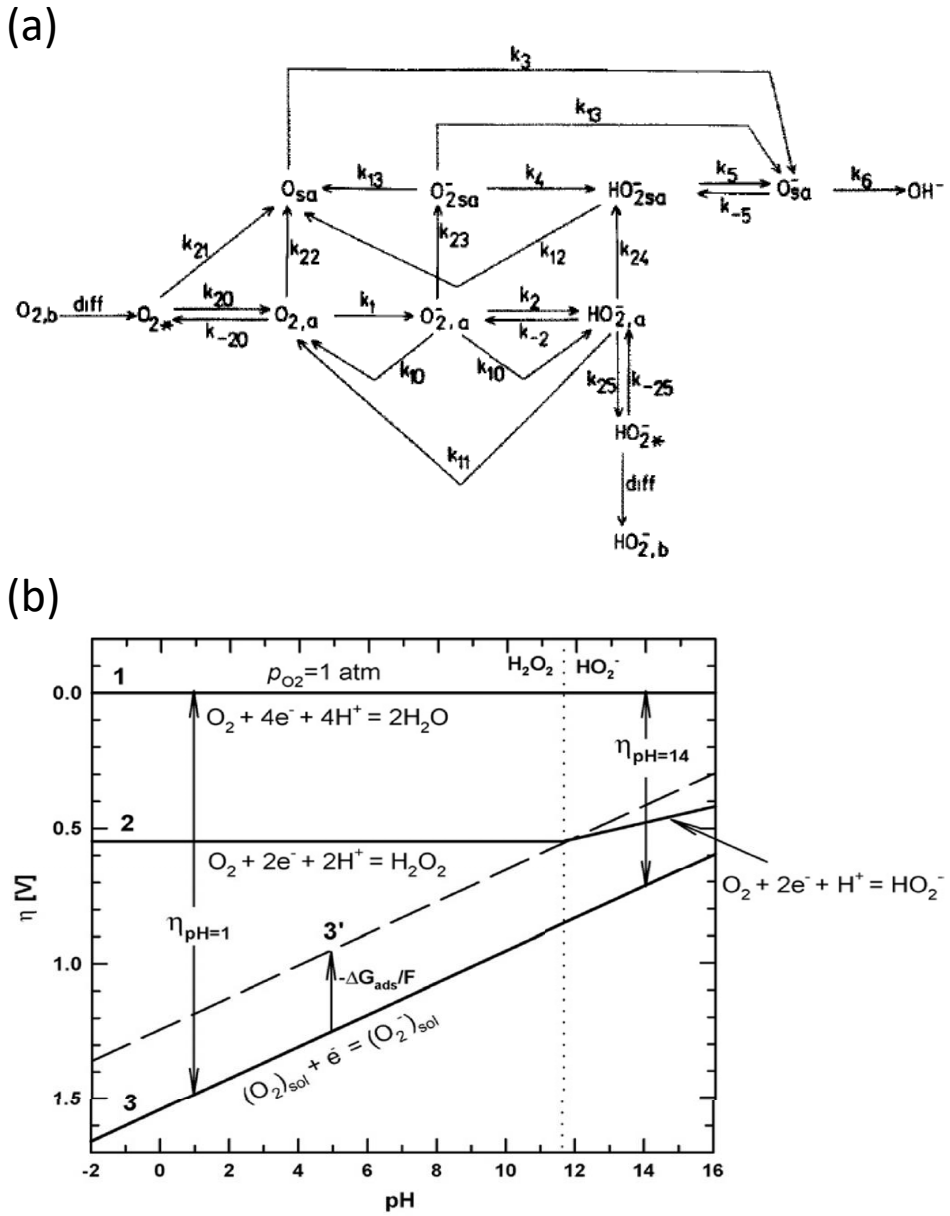

Figure 3. (a) General scheme of oxygen reduction reaction. [85]. Reproduced with permission from Elsevier. (b) Modified form of Pourbaix diagram [86]. Reproduced with permission from The Electrochemical Society.

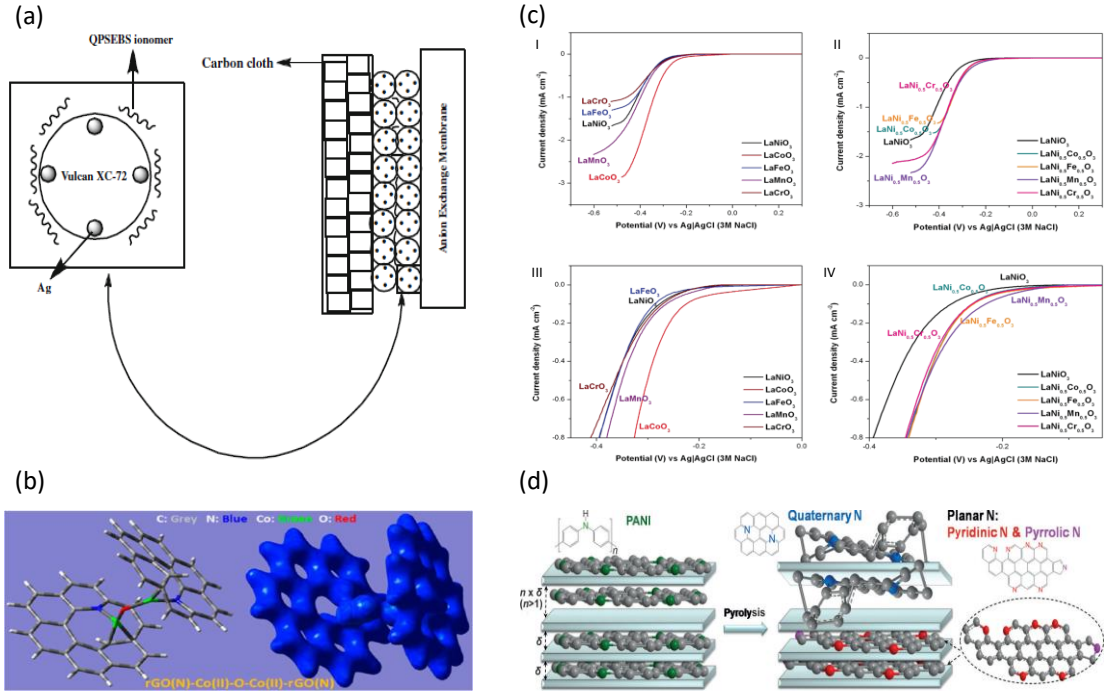

Figure 4. (a) Schematic of cathode side in the MEA using Ag/C as a catalyst [55]. Reproduced with permission from Springer. (b) Optimal structure of rGO(N)-Co(II)-O-Co(II)-rGO(N) [97]. (c) ORR current densities of thin film of (I) $LaNiO_3$, $LaCoO_3$, $LaFeO_3$, $LaMnO_3$, and $LaCrO_3$ and (II) $LaNi_{0.5}Co_{0.5}O_3$, $LaNi_{0.5}Fe_{0.5}O_3$, $LaNi_{0.5}Mn_{0.5}O_3$, and $LaNi_{0.5}Cr_{0.5}O_3$. (III) (IV) Magnified portion to pinpoint the onset ORR potentials on panels I and II, respectively. Reproduced with permission from American Chemical Society [99]. (d) Schematic of the selectivity inside and outside of MMT during NG synthesis [109]. Reproduced with permission from Wiley.

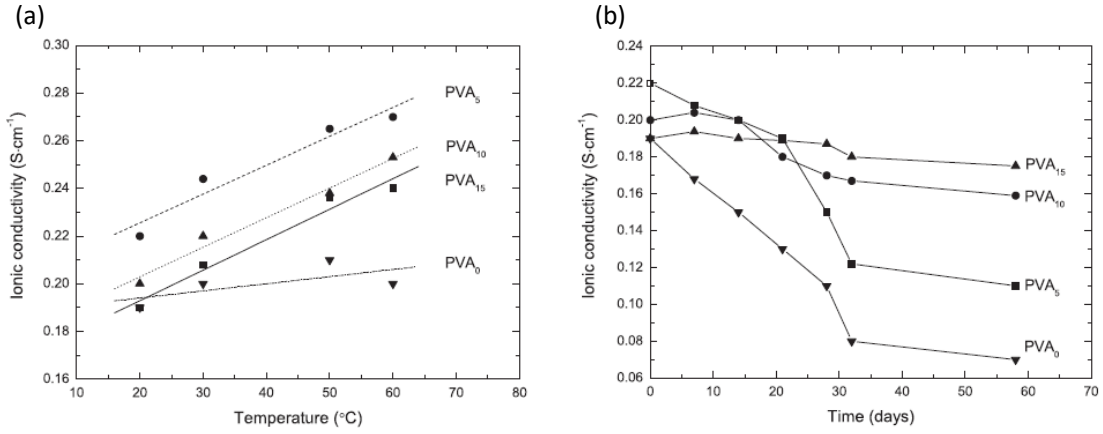

Figure 5. Effect of (a) the temperature and (b) the time on ionic conductivity [114]. Reproduced with permission from Elsevier.

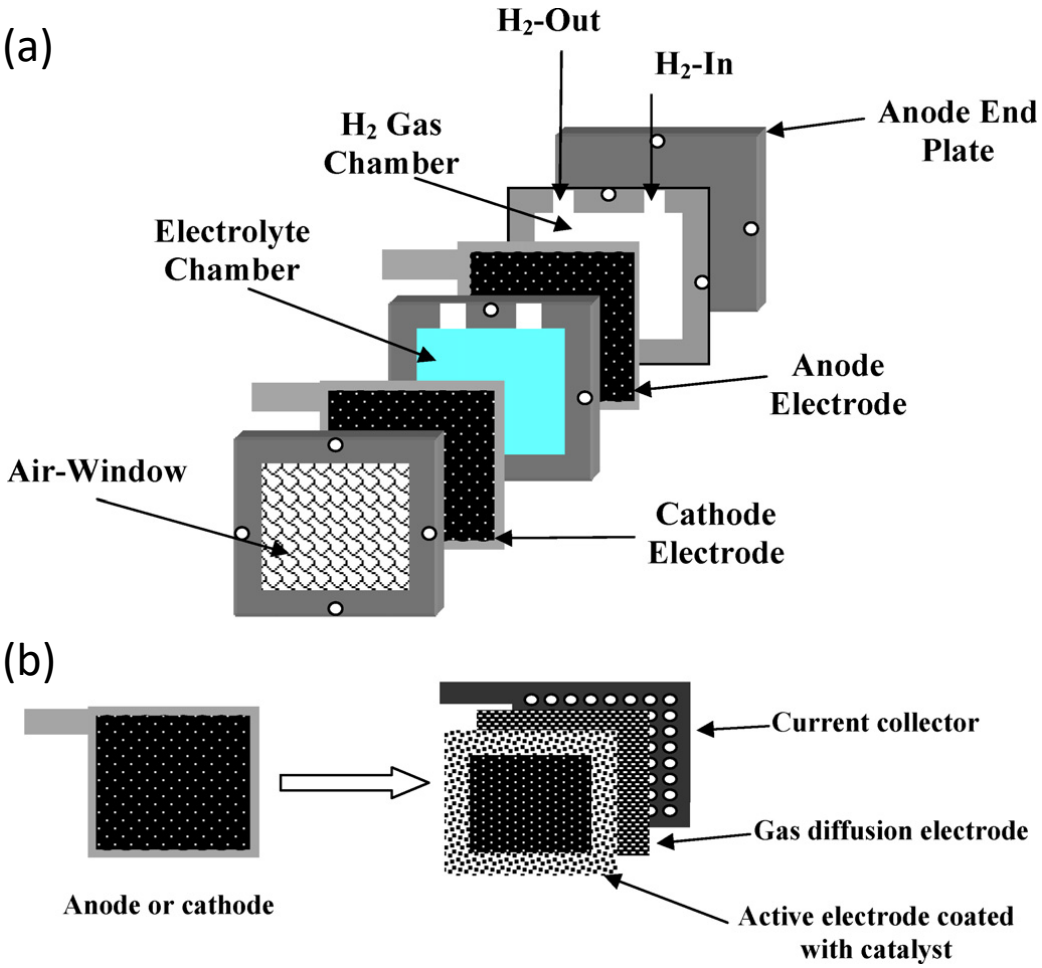

Figure 6. Schematic of (a) an air-breathing cell and (b) the electrode configuration [172]. Reproduced with permission from Elsevier.

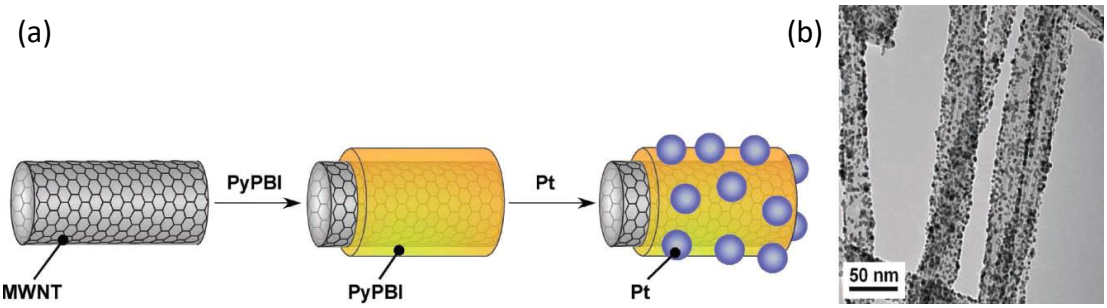

Figure 7. Schematic of (a) the preparation of the MWNT/PyPBI/Pt samples and (b) TEM image of

the MWNT/PyPBI/Pt [193]. Reproduced with permission from Wiley.

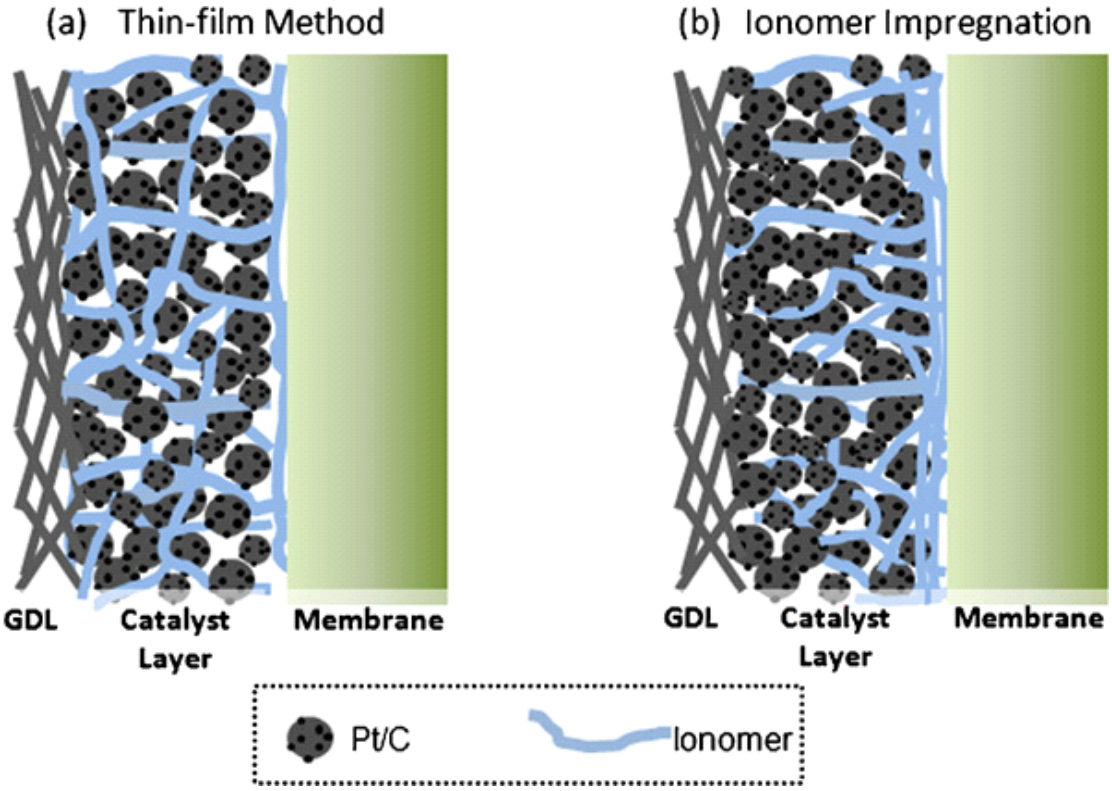

Figure 8. Schematic of the electrode structures made by (a) thin-film and (b) ionomer impregnation methods [199]. Reproduced with permission from Elsevier.

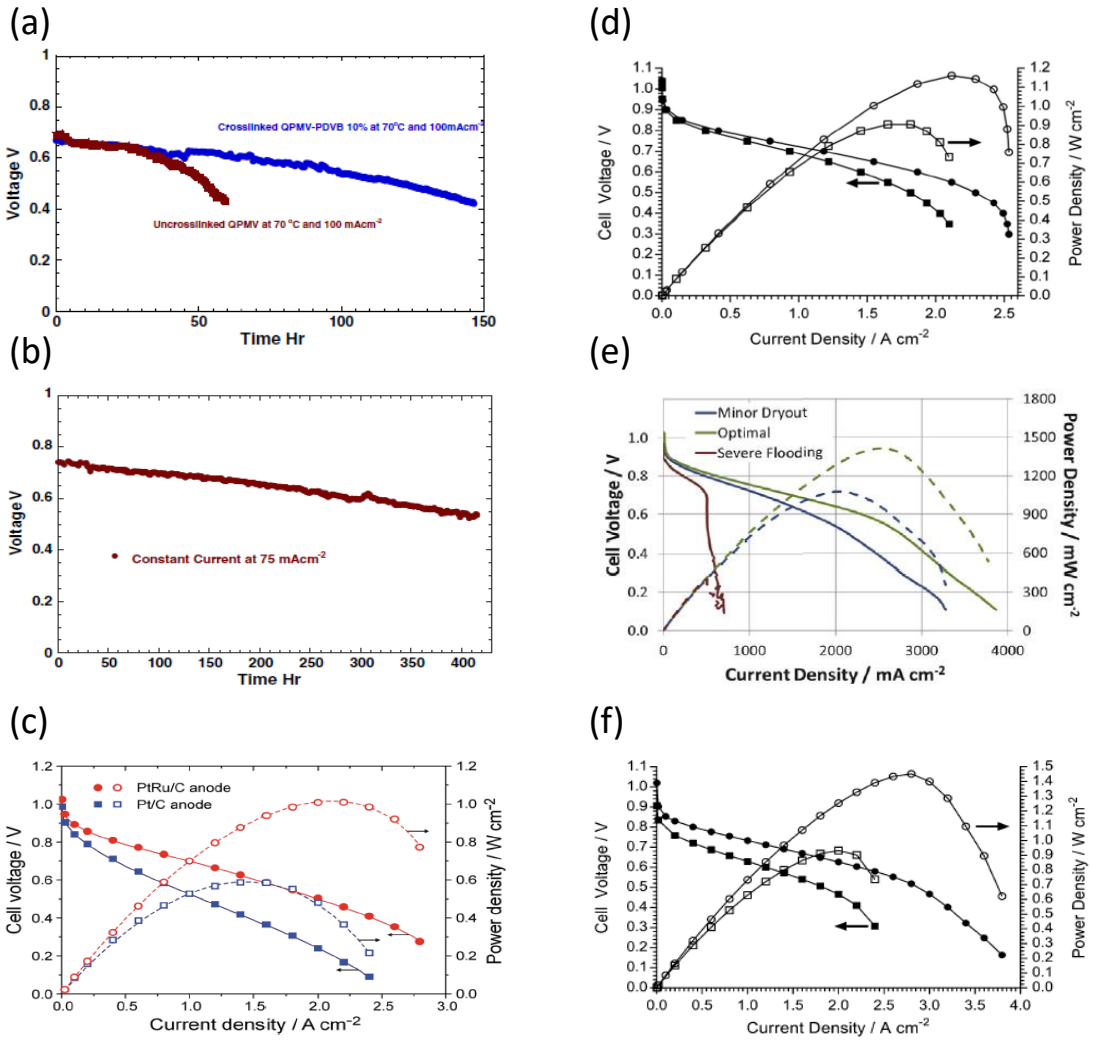

Figure 9. (a) Durability tests of uncrosslinked QPMV and 10% crosslinked QPMV-PDVB AAEMs at 70°C, (b) Durability test of 10% crosslinked AAEM at 50°C [207]. Reproduced with permission from Elsevier. (c) Cell performance of the AEMFC using the PtRu anode or Pt anode [210]. Reproduced with permission from The Royal Society of Chemistry. (d) Performance of H_2/O_2 AEMFC test data at 60 °C for E-R (squares) and E-6 (circles) using PtRu/C anodes and Pt/C cathodes and with no gas back-pressurization of the fully humidified gases [190]. (e) Performance of the AEMFC with different hypothesized distribution of water across the AEM and electrodes in an AEMFC [205]. (f) Performance of H_2/O_2 AEMFC at 80 °C with the LDPE-AEM with Pt/C (circles) or Ag/C (squares) as cathodes as well as PtRu/C anode [191]. Reproduced with permission from Elsevier.

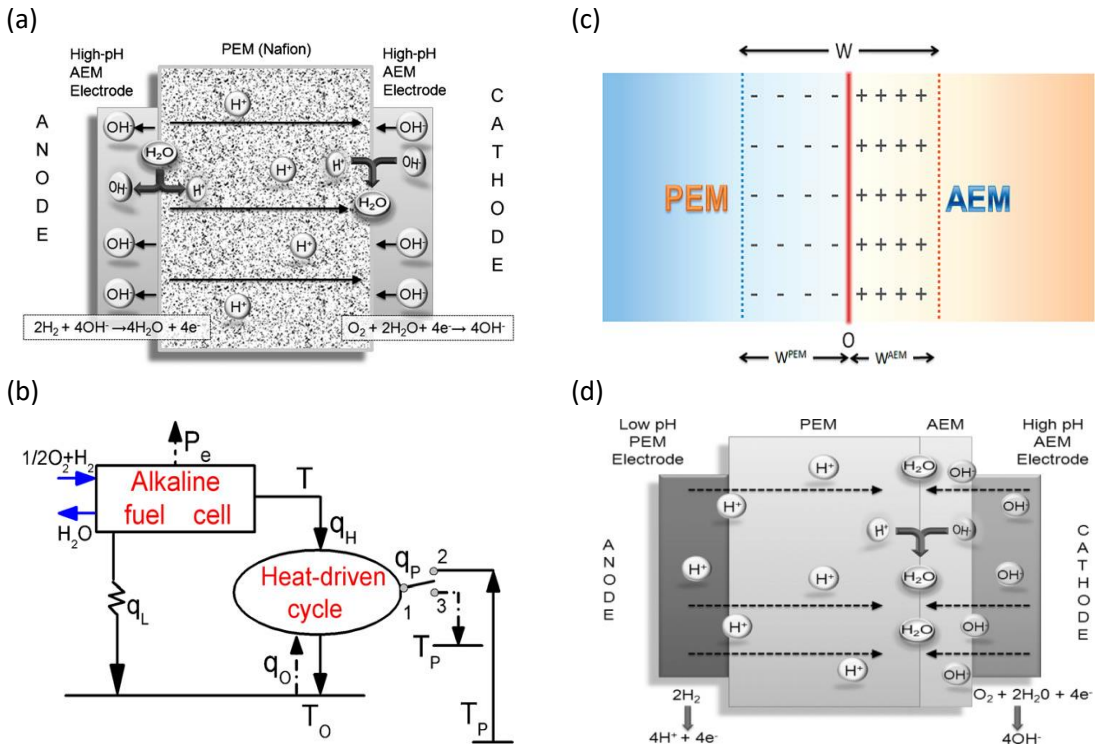

Figure 10. (a) Schematic of a hybrid fuel cell comprising high pH AEM electrodes and a PEM [211]. Reproduced with permission from Wiley. (b) Schematic of an AFC/heat-driven cycle hybrid system [213]. Reproduced with permission from Elsevier. (c) Schematic of the depletion region at the junction of the AEM and PEM in contact [214]. Reproduced with permission from American Chemical Society. (d) Schematic of hybrid fuel cells comprising low pH anode/high pH cathode [215]. Reproduced with permission from Wiley.

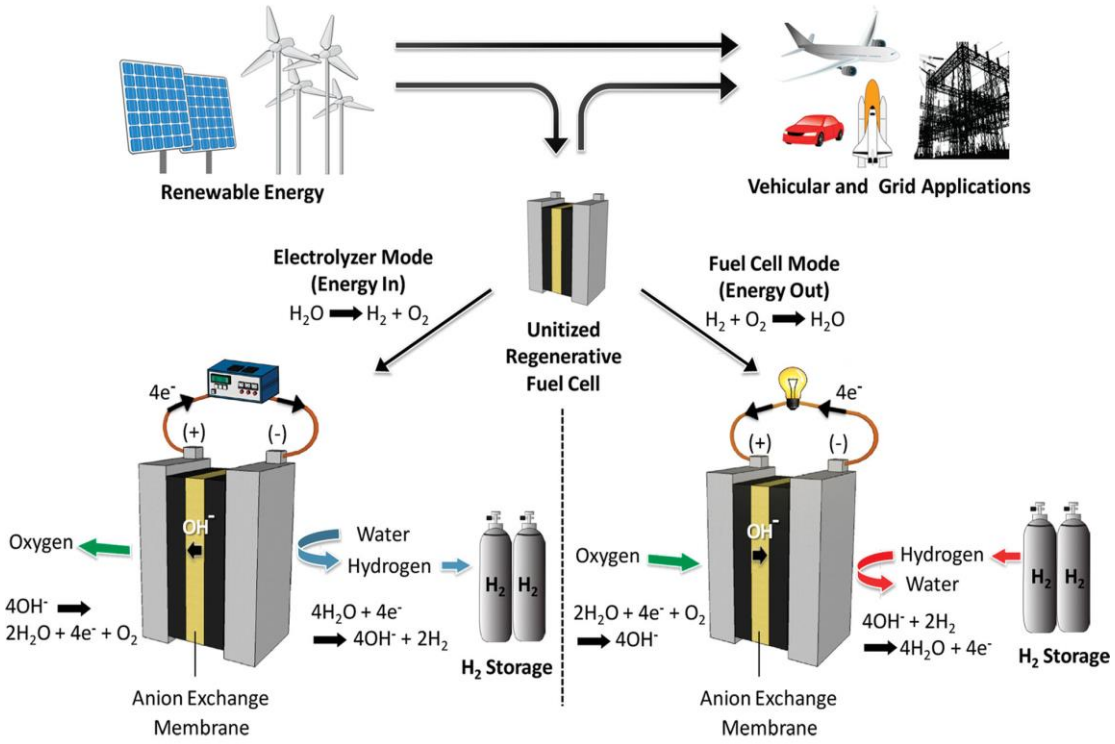

Figure 11. Schematic of an AEM-URFC as an energy storage device for grid applications [217]. Reproduced with permission from Wiley.

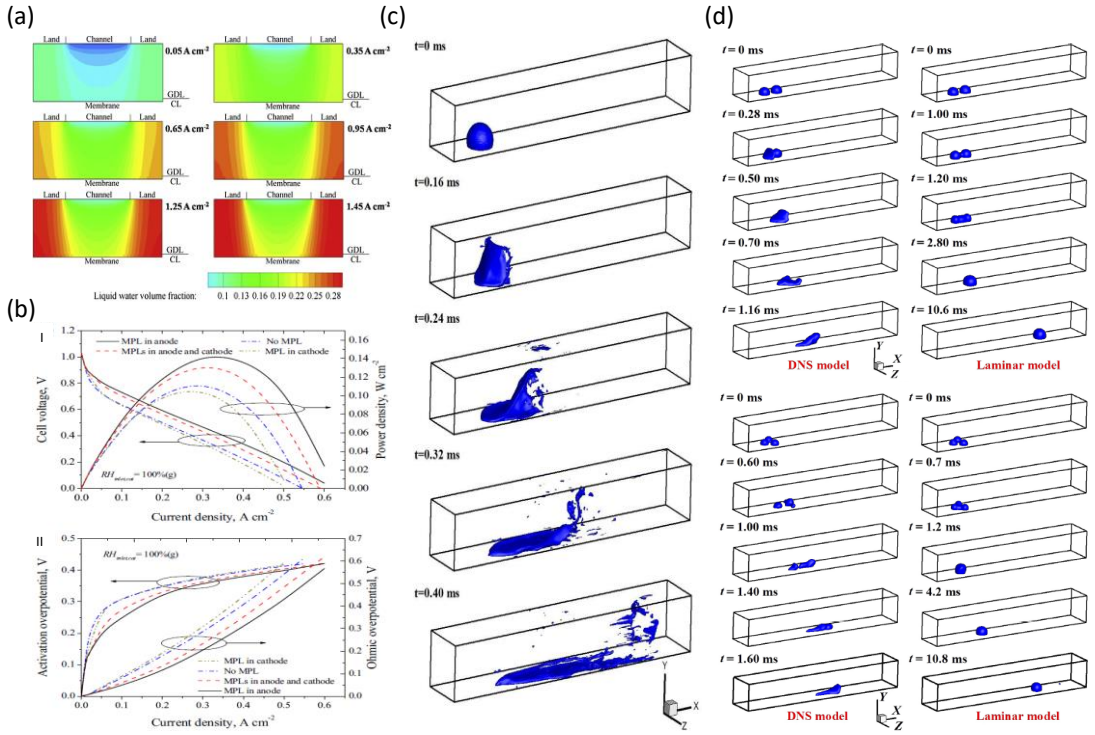

Figure 12. (a) Distributions of liquid water in anode catalyst layer and gas diffusion layer at different current densities [227]. (b) Effect of MPL configurations on (I) cell voltage and power density and (II) activation and ohmic overpotential with 100% cathode inlet humidification [230]. (c) Phase boundary of the water droplet in the DNS model of turbulent two-phase flow at different time instances [231]. (d) Iso-surface of the water phase fraction for two-droplet case and three-droplet case at different time instances [232]. Reproduced with permission from Elsevier.

Fuel/Oxidant	Anode	Cathode	Membrane	T (°C)	P(mW cm^{-2})	Ref.
H_2 (RH = 100%) / O_2 (RH = 100%)	Cr/Ni (5 mg cm^{-2})	Ag (1 mg cm^{-2})	quaternary ammonium polysulphone membranes	60	50	54
200 sccm dry H_2 / 1000 sccm air	Pd/Ni (1.5 mg cm^{-2})	Ag (3 mg cm^{-2})	AAEM	73	400	69
200 sccm dry H_2 / 1000 sccm air	Pd (1.5 mg cm^{-2})	Ag (3 mg cm^{-2})	AAEM	73	180	69
200 sccm dry H_2 / 1000 sccm air	Ni (1.5 mg cm^{-2})	Ag (3 mg cm^{-2})	AAEM	73	70	69
500 sccm H_2 (RH = 100%) / 500 sccm O_2 (RH = 100%)	Pt/C (0.5 mg cm^{-2})	Pt/C (0.5 mg cm^{-2})	Tokuyama A201	50	~185	70

500 sccm H_2 (RH = 100%) / 500 sccm O_2 (RH = 100%)	3 nm Ru/C (0.5 mg cm^{-2})	Pt/C (0.5 mg cm^{-2})	Tokuyama A201	50	~250	70
500 sccm H_2 (RH = 100%) / 500 sccm O_2 (RH = 100%)	11 nm Ru/C (0.5 mg cm^{-2})	Pt/C (0.5 mg cm^{-2})	Tokuyama A201	50	~135	70
200 sccm dry H_2 / 1000 sccm air	Pd/C (0.3 mg cm^{-2})	Ag (3 mg cm^{-2})	AAEM	73	100	73
200 sccm dry H_2 / 1000 sccm air	Pd/C-CeO_2 (0.3 mg cm^{-2})	Ag (3 mg cm^{-2})	AAEM	73	500	73
50 sccm H_2 (RH = 100%) / 50 sccm O_2 (RH = 100%)	Ni-W (17.5 mg cm^{-2})	Coppy/C (2 mg cm^{-2})	xQAPS membrane	60	40	74
50 sccm H_2 (RH = 100%) / 50 sccm air (RH = 100%)	Ni-W (17.5 mg cm^{-2})	Coppy/C (2 mg cm^{-2})	xQAPS membrane	60	27.5	74
200 sccm dry H_2 / 1000 sccm air	Pd/C-CeO_2 (0.3 mg cm^{-2}, Pd 6%)	Ag (3 mg cm^{-2})	AAEM	73	390	84
200 sccm dry H_2 / 1000 sccm air	Pd/C-CeO_2 (0.3 mg cm^{-2}, Pd 10%)	Ag (3 mg cm^{-2})	AAEM	73	500	84
200 sccm dry H_2 / 1000 sccm air	Pd/C-CeO_2 (0.3 mg cm^{-2}, Pd 20%)	Ag (3 mg cm^{-2})	AAEM	73	460	84

Table 1 Selected hydrogen/oxygen fuel cell performance with different HOR electrocatalysts reported in open literature.

Fuel/Oxidant	Anode	Cathode	Membrane	T (°C)	P(mW cm^{-2})	Ref.
H_2 / O_2	Pt/C (0.375 mg cm^{-2})	Ag/C (0.5 mg cm^{-2})	AEM	60	109	55
2000 sccm H_2 (RH = 100%) / 2000 sccm O_2 (RH = 100%)	Pt/C (20 wt%) (0.5 mg cm^{-2})	Pt/C (20 wt%) (0.5 mg cm^{-2})	AAEM-MEAs	50	~54	87
2000 sccm H_2 (RH =	Pt/C (20 wt%)	Ag/C (60 wt%)	AAEM-MEAs	50	~47	87

100%) / 2000 sccm O_2 (RH = 100%)	(0.5 mg cm^{-2})	(4 mg cm^{-2})				
2000 sccm H_2 (RH = 100%) / 2000 sccm O_2 (RH = 100%)	Pt/C (20 wt%) (0.5 mg cm^{-2})	Au/C (60 wt%) (4 mg cm^{-2})	AAEM-MEAs	50	~20	87
2000 sccm H_2 (RH = 100%) / 2000 sccm O_2 (RH = 82%)	Pt/C (20 wt%) (0.5 mg cm^{-2})	Pt/C (20 wt%) (0.5 mg cm^{-2})	AAEM-MEAs	50	~28	87
2000 sccm H_2 (RH = 82%) / 2000 sccm O_2 (RH = 100%)	Pt/C (20 wt%) (0.5 mg cm^{-2})	Pt/C (20 wt%) (0.5 mg cm^{-2})	AAEM-MEAs	50	~25	87
H_2 (RH = 100%) / Air (RH = 100%)	Pt/C (40 wt%) (0.5 mg cm^{-2})	Pt/C (0.5 mg cm^{-2})	the mixture of TMA and TMHDA with a ratio of 3:1	60	28.2	88
H_2 (RH = 100%) / Air (RH = 100%)	Pt/C (40 wt%) (0.5 mg cm^{-2})	Ag/C (0.5 mg cm^{-2})	the mixture of TMA and TMHDA with a ratio of 3:1	60	8.1	88
H_2 (RH = 100%) / Air (RH = 100%)	Pt/C (40 wt%) (0.5 mg cm^{-2})	Ag/C (1.0 mg cm^{-2})	the mixture of TMA and TMHDA with a ratio of 3:1	60	19.9	88
H_2 (RH = 100%) / Air (RH = 100%)	Pt/C (40 wt%) (0.5 mg cm^{-2})	Ag/C (2.0 mg cm^{-2})	the mixture of TMA and TMHDA with a ratio of 3:1	60	30.1	88
500 sccm H_2 (RH = 100%) / 500 sccm O_2 (RH = 100%)	Pt/C (0.5 mg cm^{-2})	Pt/C (0.5 mg cm^{-2})	AHA Membrane (without ionomer in both anode and cathode)	R.T.	~6	90
500 sccm H_2 (RH = 100%) / 500 sccm O_2 (RH = 100%)	Pt/C (0.5 mg cm^{-2})	Pt/C (0.5 mg cm^{-2})	ACS Membrane (without ionomer in both anode and cathode)	R.T.	2	90
500 sccm H_2 (RH = 100%) / 500 sccm O_2 (RH = 100%)	Pt/C (0.5 mg cm^{-2})	Pt/C (0.5 mg cm^{-2})	AHA Membrane (with ionomer in both anode and cathode)	R.T.	55	90
500 sccm H_2 (RH = 100%) / 500 sccm O_2 (RH = 100%)	Pt/C (0.5 mg cm^{-2})	Pt/C (0.5 mg cm^{-2})	AHA Membrane (with ionomer in cathode and without at anode)	R.T.	40	90
500 sccm H_2 (RH = 100%) / 500 sccm O_2 (RH = 100%)	Pt/C (0.5 mg cm^{-2})	Pd/C (0.5 mg cm^{-2})	AHA Membrane (with ionomer in cathode and without at anode)	R.T.	55	90

500 sccm H_2 (RH = 100%) / 500 sccm O_2 (RH = 100%)	Pt/C (0.5 mg cm^{-2})	Pt/C (0.5 mg cm^{-2})	AHA Membrane (with ionomer in cathode and without at anode)	R.T.	40	90
500 sccm H_2 (RH = 100%) / 500 sccm O_2 (RH = 100%)	Pt/C (0.5 mg cm^{-2})	Au/C (0.5 mg cm^{-2})	AHA Membrane (with ionomer in cathode and without at anode)	R.T.	1	90
500 sccm H_2 (RH = 100%) / 500 sccm O_2 (RH = 100%)	Pt/C (0.5 mg cm^{-2})	Pd/C (0.5 mg cm^{-2})	alkaline polymer electrolyte membrane	30	56	91
500 sccm H_2 (RH = 100%) / 500 sccm O_2 (RH = 100%)	Pt/C (0.5 mg cm^{-2})	PdCo(1:1)/C (0.5 mg cm^{-2})	alkaline polymer electrolyte membrane	30	26	91
500 sccm H_2 (RH = 100%) / 500 sccm O_2 (RH = 100%)	Pt/C (0.5 mg cm^{-2})	PdCo(2:1)/C (0.5 mg cm^{-2})	alkaline polymer electrolyte membrane	30	75	91
500 sccm H_2 (RH = 100%) / 500 sccm O_2 (RH = 100%)	Pt/C (0.5 mg cm^{-2})	PdCo(3:1)/C (0.5 mg cm^{-2})	alkaline polymer electrolyte membrane	30	85	91
500 sccm H_2 (RH = 100%) / 500 sccm air (RH = 100%)	Pt/C (0.5 mg cm^{-2})	Pd/C (0.5 mg cm^{-2})	alkaline polymer electrolyte membrane	30	19	91
500 sccm H_2 (RH = 100%) / 500 sccm air (RH = 100%)	Pt/C (0.5 mg cm^{-2})	PdCo(1:1)/C (0.5 mg cm^{-2})	alkaline polymer electrolyte membrane	30	15	91
500 sccm H_2 (RH = 100%) / 500 sccm air (RH = 100%)	Pt/C (0.5 mg cm^{-2})	PdCo(2:1)/C (0.5 mg cm^{-2})	alkaline polymer electrolyte membrane	30	26	91
500 sccm H_2 (RH = 100%) / 500 sccm air (RH = 100%)	Pt/C (0.5 mg cm^{-2})	PdCo(3:1)/C (0.5 mg cm^{-2})	alkaline polymer electrolyte membrane	30	37	91
200 sccm H_2 (RH = 100%) / 400 sccm O_2 (RH = 100%)	Pt/C (0.4 mg cm^{-2})	Tanaka Pt/C (0.6 mg cm^{-2})	Tokuyama A201 membrane	45	~130	94
200 sccm H_2 (RH = 100%) / 400 sccm O_2 (RH = 100%)	Pt/C (0.4 mg cm^{-2})	E-Tek Pt/C (0.6 mg cm^{-2})	Tokuyama A201 membrane	45	~120	94
200 sccm H_2 (RH = 100%)	Pt/C	CoPc/MWCNT	Tokuyama A201	45	~100	94

/ 400 sccm O_2 (RH = 100%)	(0.4 mg cm^{-2})	(0.6 mg cm^{-2})	membrane			
200 sccm H_2 (RH = 100%) / 400 sccm O_2 (RH = 100%)	Pt/C (0.4 mg cm^{-2})	FePc/MWCNT (0.6 mg cm^{-2})	Tokuyama A201 membrane	45	~60	94
200 sccm H_2 (RH = 100%) / 400 sccm O_2 (RH = 100%)	Pt/C (0.4 mg cm^{-2})	MWCNT (0.6 mg cm^{-2})	Tokuyama A201 membrane	45	~25	94
200 sccm H_2 (RH = 100%) / 400 sccm O_2 (RH = 100%)	Pt/C (0.4 mg cm^{-2})	Pt/C (0.4 mg cm^{-2})	anion exchange membrane	50	196	95
200 sccm H_2 (RH = 100%) / 400 sccm O_2 (RH = 100%)	Pt/C (0.4 mg cm^{-2})	CoFeN/C-HLH (4 mg cm^{-2})	anion exchange membrane	50	177	95
250 sccm H_2 (RH = 57%) / 500 sccm O_2 (RH = 100%)	Pt/C (1.5 mg cm^{-2})	Pt/C (1.5 mg cm^{-2})	Tokuyama A201	60	387	97
250 sccm H_2 (RH = 57%) / 500 sccm O_2 (RH = 100%)	Pt/C (1.5 mg cm^{-2})	CoO/rGO(N) (0.6 mg cm^{-2})	Tokuyama A201	60	248	97
300 sccm H_2 / 300 sccm O_2	Pt/C (0.5 mg cm^{-2})	ED-CNT (0.2 mg cm^{-2})	commercial FAA anion exchange membrane	80	25.5	107
300 sccm H_2 / 300 sccm O_2	Pt/C (0.5 mg cm^{-2})	Pt/C (0.2 mg cm^{-2})	commercial FAA anion exchange membrane	80	19.1	107

Table 2 Selected hydrogen/oxygen fuel cell performance with different ORR electrocatalysts reported in open literature.

2514
2515
2516
2517
2518
2519
2520
2521

Fuel/Oxidant	Anode	Cathode	Membrane	T (°C)	P(mW cm^{-2})	Ref.
H_2/O_2	Pt/C (0.4 mg cm^{-2})	Pt/C (0.4 mg cm^{-2})	X-23 AAEM	60	823	3
H_2/O_2	Pt/C (0.4 mg cm^{-2})	Pt/C (0.4 mg cm^{-2})	X-23 AAEM	50	718	3
H_2/O_2	Pt/C (0.4 mg cm^{-2})	Pt/C (0.4 mg cm^{-2})	X-19 AAEM	40	640	3
H_2/O_2	Pt/C (0.4 mg cm^{-2})	Pt/C (0.4 mg cm^{-2})	X-19 AAEM	20	648	3
H_2/Air	Pt/C (0.4 mg cm^{-2})	Pt/C (0.4 mg cm^{-2})	X-5 AAEM	60	506	3
H_2/Air	Pt/C (0.4 mg cm^{-2})	Pt/C (0.4 mg cm^{-2})	X-5 AAEM	50	464	3
H_2/Air	Pt/C (0.4 mg cm^{-2})	Pt/C (0.4 mg cm^{-2})	X-23 AAEM	40	450	3
2000 sccm H_2 (RH = 100%) / 2000 sccm O_2 (RH = 100%)	Pt/C (0.5 mg cm^{-2})	Pt/C (0.5 mg cm^{-2})	radiation-grafted AAEMs-S80	50	~100	9
2000 sccm H_2 (RH = 100%) / 2000 sccm O_2 (RH = 100%)	Pt/C (0.5 mg cm^{-2})	Pt/C (0.5 mg cm^{-2})	radiation-grafted AAEMs-S50	50	~150	9
2000 sccm H_2 (RH = 100%) / 2000 sccm O_2 (RH = 100%)	Pt/C (0.5 mg cm^{-2})	Pt/C (0.5 mg cm^{-2})	radiation-grafted AAEMs-S20	50	~230	9
2000 sccm H_2 (RH = 100%) / 2000 sccm O_2 (RH = 100%)	Pt/C (0.5 mg cm^{-2})	Au/C (0.5 mg cm^{-2})	radiation-grafted AAEMs-S80	50	36.6	9
2000 sccm H_2 (RH = 100%) / 2000 sccm O_2 (RH	Pt/C (0.5 mg cm^{-2})	Ag/C (0.5 mg cm^{-2})	radiation-grafted AAEMs-S80	50	19.1	9

= 100%)						
80 sccm H_2 (RH = 100%) / 100 sccm O_2 (RH = 100%)	Pt/C (0.5 mg cm^{-2})	Pt/C (0.5 mg cm^{-2})	PTFE-QDPSU composite membrane	30	~60	61
80 sccm H_2 (RH = 100%) / 100 sccm O_2 (RH = 100%)	Pt/C (0.5 mg cm^{-2})	Pt/C (0.5 mg cm^{-2})	PTFE-QDPSU composite membrane	40	~100	61
80 sccm H_2 (RH = 100%) / 100 sccm O_2 (RH = 100%)	Pt/C (0.5 mg cm^{-2})	Pt/C (0.5 mg cm^{-2})	PTFE-QDPSU composite membrane	50	146	61
80 sccm H_2 (RH = 100%) / 100 sccm CO_2 free air (RH = 100%)	Pt/C (0.5 mg cm^{-2})	Pt/C (0.5 mg cm^{-2})	PTFE-QDPSU composite membrane	50	103	61
40 sccm H_2 (RH = 100%) / 80 sccm O_2 (RH = 100%)	Pt/C (4 mg cm^{-2})	Pt/C (4 mg cm^{-2})	PVA_{15} membrane	25	72	114
100 sccm H_2 (RH = 100%) / 70 sccm O_2 (RH = 100%)	Pt/C (0.5 mg cm^{-2})	Pt/C (0.5 mg cm^{-2})	PVA/PDDA AAEM (HMw)	25	35.1	115
100 sccm H_2 (RH = 100%) / 70 sccm O_2 (RH = 100%)	Pt/C (0.5 mg cm^{-2})	Pt/C (0.5 mg cm^{-2})	PVA/PDDA AAEM (MMw)	25	28.5	115
100 sccm H_2 (RH = 100%) / 70 sccm O_2 (RH = 100%)	Pt/C (0.5 mg cm^{-2})	Pt/C (0.5 mg cm^{-2})	PVA/PDDA AAEM (LMw)	25	23.4	115
100 sccm H_2 (RH = 100%) / 70 sccm O_2 (RH = 100%)	Pt/C (0.5 mg cm^{-2})	Pt/C (0.5 mg cm^{-2})	PVA/PDDA AAEM (ULMw)	25	18.2	115
300 sccm H_2 (RH = 100%) / 800 sccm air (RH = 100%)	Pt/C (0.1 mg cm^{-2})	Pt/C (0.2 mg cm^{-2})	QBMPAE-d alkaline anion exchange membrane	70	20.1	117
100 sccm H_2 (RH = 100%) / 70 sccm O_2 (RH = 100%)	Pt/C (0.5 mg cm^{-2})	Pt/C (0.5 mg cm^{-2})	PVA/PDDA-OH^- membrane	25	32.7	120
100 sccm H_2 (RH = 100%) / 70 sccm O_2 (RH = 100%)	Pt/C (0.5 mg cm^{-2})	Pt/C (0.5 mg cm^{-2})	Tokuyama A901	R.T.	37.7	121
100 sccm H_2 (RH = 100%) / 70 sccm O_2 (RH = 100%)	Pt/C (0.5 mg cm^{-2})	Pt/C (0.5 mg cm^{-2})	PVA/PDDA-OH^- alkaline membranes (PVA:PDDA=1:0.75)	R.T.	14.8	121
100 sccm H_2 (RH = 100%) / 70 sccm O_2 (RH = 100%)	Pt/C (0.5 mg cm^{-2})	Pt/C (0.5 mg cm^{-2})	PVA/PDDA-OH^- alkaline membranes (PVA:PDDA=1:0.5)	R.T.	35.1	121
100 sccm H_2 (RH = 100%) / 70 sccm O_2 (RH = 100%)	Pt/C (0.5 mg cm^{-2})	Pt/C (0.5 mg cm^{-2})	PVA/PDDA-OH^- alkaline membranes (PVA:PDDA=1:0.25)	R.T.	11.5	121
40 sccm H_2 (RH = 100%) /	Pt/C	Pt/C	PVAc(1)-c-PVBC(1)/OH	40	124.7	122

70 sccm O_2 (RH = 100%)	(0.4 mg cm^{-2})	(0.4 mg cm^{-2})	membrane			
5 sccm H_2 (RH = 100%) / 10 sccm O_2 (RH = 100%)	Pt/C (0.65 mg cm^{-2})	Pt/C (0.65 mg cm^{-2})	PPO-based anion exchange membrane	25	~3	124
5 sccm H_2 (RH = 100%) / 10 sccm O_2 (RH = 100%)	Pt/C (0.65 mg cm^{-2})	Pt/C (0.65 mg cm^{-2})	PPO-based anion exchange membrane	30	~3	124
5 sccm H_2 (RH = 100%) / 10 sccm O_2 (RH = 100%)	Pt/C (0.65 mg cm^{-2})	Pt/C (0.65 mg cm^{-2})	PPO-based anion exchange membrane	40	~8.5	124
5 sccm H_2 (RH = 100%) / 10 sccm O_2 (RH = 100%)	Pt/C (0.65 mg cm^{-2})	Pt/C (0.65 mg cm^{-2})	PPO-based anion exchange membrane	50	~8	124
5 sccm H_2 (RH = 100%) / 10 sccm O_2 (RH = 100%)	Pt/C (0.65 mg cm^{-2})	Pt/C (0.65 mg cm^{-2})	PPO-based anion exchange membrane	60	~11.5	124
5 sccm H_2 (RH = 100%) / 10 sccm O_2 (RH = 100%)	Pt/C (0.65 mg cm^{-2})	Pt/C (0.65 mg cm^{-2})	PPO-based anion exchange membrane	70	19.5	124
5 sccm H_2 (RH = 100%) / 10 sccm O_2 (RH = 100%)	Pt/C (0.65 mg cm^{-2})	Pt/C (0.65 mg cm^{-2})	PPO-based anion exchange membrane	80	~15	124
600 sccm H_2 (RH = 100%) / 600 sccm O_2 (RH = 100%)	Pt/C (0.4 mg cm^{-2})	Pt/C (0.4 mg cm^{-2})	BIm-PPO-0.54 AAEM	35	13	126
600 sccm H_2 (RH = 100%) / 600 sccm O_2 (RH = 100%)	Pt/C (0.4 mg cm^{-2})	Pt/C (0.4 mg cm^{-2})	alkaline polymer electrolyte membrane (DIm-PPO-0.54)	35	56	127
600 sccm H_2 (RH = 100%) / 600 sccm O_2 (RH = 100%)	Pt/C (0.4 mg cm^{-2})	Pt/C (0.4 mg cm^{-2})	alkaline polymer electrolyte membrane (DIm-PPO-0.43)	35	40	127
600 sccm H_2 (RH = 100%) / 600 sccm O_2 (RH = 100%)	Pt/C (0.4 mg cm^{-2})	Pt/C (0.4 mg cm^{-2})	alkaline polymer electrolyte membrane (Im-PPO)	50	30	127
200 sccm H_2 (RH = 100%) / 200 sccm O_2 (RH = 100%)	Pt/C (0.5 mg cm^{-2})	Pt/C (0.5 mg cm^{-2})	1a electrolyte membrane	50	188.7	128
200 sccm H_2 (RH = 100%) / 200 sccm O_2 (RH = 100%)	Pt/C (0.5 mg cm^{-2})	Pt/C (0.5 mg cm^{-2})	TMA-20 electrolyte membrane	50	62.3	128
100 sccm H_2 (RH = 100%) / 2000 sccm O_2 (RH = 100%)	Pt/C (0.4 mg cm^{-2})	Pt/C (0.4 mg cm^{-2})	TPPVBN30	50	268	132

100 sccm H_2 (RH = 100%) / 2000 sccm O_2 (RH = 100%)	Pt/C (0.4 mg cm^{-2})	Pt/C (0.4 mg cm^{-2})	TPPVBN30	60	348	132
100 sccm H_2 (RH = 100%) / 200 sccm O_2 (RH = 100%)	Pt/C (0.4 mg cm^{-2})	Pt/C (0.4 mg cm^{-2})	QAPS/PTFE 29 um CCM	50	252	133
100 sccm H_2 (RH = 100%) / 200 sccm O_2 (RH = 100%)	Pt/C (0.4 mg cm^{-2})	Pt/C (0.4 mg cm^{-2})	QAPS/PTFE 20 um CCM	50	315	133
100 sccm H_2 (RH = 100%) / 200 sccm O_2 (RH = 100%)	Pt/C (0.4 mg cm^{-2})	Pt/C (0.4 mg cm^{-2})	QAPS/PTFE 29 um GDE	50	152	133
100 sccm H_2 (RH = 100%) / 200 sccm O_2 (RH = 100%)	Pt/C (0.4 mg cm^{-2})	Pt/C (0.4 mg cm^{-2})	QAPS 30 um GDE	50	145	133
120 sccm H_2 (RH = 100%) / 120 sccm O_2 (RH = 100%)	Pt/C (0.4 mg cm^{-2})	Pt/C (0.4 mg cm^{-2})	xQAPS@PTFE membrane	40 (0 MPa)	~180	134
120 sccm H_2 (RH = 100%) / 120 sccm O_2 (RH = 100%)	Pt/C (0.4 mg cm^{-2})	Pt/C (0.4 mg cm^{-2})	xQAPS@PTFE membrane	50 (0 MPa)	~400	134
120 sccm H_2 (RH = 100%) / 120 sccm O_2 (RH = 100%)	Pt/C (0.4 mg cm^{-2})	Pt/C (0.4 mg cm^{-2})	xQAPS@PTFE membrane	60 (0 MPa)	~450	134
120 sccm H_2 (RH = 100%) / 120 sccm O_2 (RH = 100%)	Pt/C (0.4 mg cm^{-2})	Pt/C (0.4 mg cm^{-2})	xQAPS@PTFE membrane	60 (0.1 MPa)	550	134
800 sccm H_2 (RH = 100%) / 600 sccm O_2 (RH = 100%)	Pt/C (2 mg cm^{-2})	Pt/C (2 mg cm^{-2})	PSU-PATC(1.2)	60	55	138
800 sccm H_2 (RH = 100%) / 600 sccm O_2 (RH = 100%)	Pt/C (2 mg cm^{-2})	Pt/C (2 mg cm^{-2})	PSU-PATC(1.5)	60	19	138
150 sccm H_2 (RH = 100%) / 200 sccm O_2 (RH = 100%)	Pt/C (0.5 mg cm^{-2})	Pt/C (2 mg cm^{-2})	QA-PSf membrane	60	115	139
150 sccm H_2 (RH = 100%)	Pt/C	Pt/C	QA-PSf-g-PEG350	60	~138	139

/ 200 sccm O_2 (RH = 100%)	(0.5 mg cm^{-2})	(2 mg cm^{-2})	membrane			
150 sccm H_2 (RH = 100%) / 200 sccm O_2 (RH = 100%)	Pt/C (0.5 mg cm^{-2})	Pt/C (2 mg cm^{-2})	QA-PSf-g-PEG750 membrane	60	180	139
H_2 (RH = 100%) / O_2 (RH = 100%)	Pt/C (0.375 mg cm^{-2})	Pt/C (0.125 mg cm^{-2})	QPSU membrane	R.T.	~70	140
H_2 (RH = 100%) / O_2 (RH = 100%)	Pt/C (0.375 mg cm^{-2})	Pt/C (0.125 mg cm^{-2})	QPSU / 2.5% ZrO_2 composite membrane	R.T.	~75	140
H_2 (RH = 100%) / O_2 (RH = 100%)	Pt/C (0.375 mg cm^{-2})	Pt/C (0.125 mg cm^{-2})	QPSU / 5% ZrO_2 composite membrane	R.T.	~80	140
H_2 (RH = 100%) / O_2 (RH = 100%)	Pt/C (0.375 mg cm^{-2})	Pt/C (0.125 mg cm^{-2})	QPSU / 7.5% ZrO_2 composite membrane	R.T.	~110	140
H_2 (RH = 100%) / O_2 (RH = 100%)	Pt/C (0.375 mg cm^{-2})	Pt/C (0.125 mg cm^{-2})	QPSU / 10% ZrO_2 composite membrane	R.T.	140	140
H_2 (RH = 100%) / O_2 (RH = 100%)	Pt/C (0.375 mg cm^{-2})	Pt/C (0.125 mg cm^{-2})	QPSU membrane	60	~155	140
H_2 (RH = 100%) / O_2 (RH = 100%)	Pt/C (0.375 mg cm^{-2})	Pt/C (0.125 mg cm^{-2})	QPSU / 2.5% ZrO_2 composite membrane	60	~165	140
H_2 (RH = 100%) / O_2 (RH = 100%)	Pt/C (0.375 mg cm^{-2})	Pt/C (0.125 mg cm^{-2})	QPSU / 5% ZrO_2 composite membrane	60	~175	140
H_2 (RH = 100%) / O_2 (RH = 100%)	Pt/C (0.375 mg cm^{-2})	Pt/C (0.125 mg cm^{-2})	QPSU / 7.5% ZrO_2 composite membrane	60	~210	140
H_2 (RH = 100%) / O_2 (RH = 100%)	Pt/C (0.375 mg cm^{-2})	Pt/C (0.125 mg cm^{-2})	QPSU / 10% ZrO_2 composite membrane	60	250	140
2000 sccm H_2 (RH = 100%) / 2000 sccm O_2 (RH = 100%)	Pt/C (0.5 mg cm^{-2})	Pt/C (0.5 mg cm^{-2})	AAEM-MEAs with alkaline interface polymer	50	55	141
2000 sccm H_2 (RH = 100%) / 2000 sccm O_2 (RH = 100%)	Pt/C (0.5 mg cm^{-2})	Pt/C (0.5 mg cm^{-2})	AAEM-MEAs without alkaline interface polymer	50	1.6	141
200 sccm H_2 (RH = 100%) / 200 sccm O_2 (RH =	Pt/C (1 mg cm^{-2})	Pt/C (1 mg cm^{-2})	A901:0.97	50	343	143

100%)						
200 sccm H_2 (RH = 100%) / 200 sccm O_2 (RH = 100%)	Pt/C (1 mg cm^{-2})	Pt/C (1 mg cm^{-2})	SEBS:0.51	50	169	143
200 sccm H_2 (RH = 100%) / 200 sccm O_2 (RH = 100%)	Pt/C (1 mg cm^{-2})	Pt/C (1 mg cm^{-2})	SEBS:0.70	50	222	143
200 sccm H_2 (RH = 100%) / 200 sccm O_2 (RH = 100%)	Pt/C (1 mg cm^{-2})	Pt/C (1 mg cm^{-2})	SEBS:0.90	50	285	143
200 sccm H_2 (RH = 100%) / 200 sccm O_2 (RH = 100%)	Pt/C (0.5 mg cm^{-2})	Pt/C (0.5 mg cm^{-2})	Tokuyama A201 (C16D40)	50	77	144
200 sccm H_2 (RH = 100%) / 200 sccm O_2 (RH = 100%)	Pt/C (0.5 mg cm^{-2})	Pt/C (0.5 mg cm^{-2})	Tokuyama A201 (C6D60)	50	67	144
500 sccm H_2 (RH = 100%) / 200 sccm O_2 (RH = 100%)	Pt/C (0.5 mg cm^{-2})	Pt/C (0.5 mg cm^{-2})	Tokuyama A201 (C6D60)	50	~80	144
1000 sccm H_2 (RH = 100%) / 200 sccm O_2 (RH = 100%)	Pt/C (0.5 mg cm^{-2})	Pt/C (0.5 mg cm^{-2})	Tokuyama A201 (C6D60)	50	~105	144
2000 sccm H_2 (RH = 100%) / 200 sccm O_2 (RH = 100%)	Pt/C (0.5 mg cm^{-2})	Pt/C (0.5 mg cm^{-2})	Tokuyama A201 (C6D60)	50	~120	144
2000 sccm H_2 (RH = 100%) / 2000 sccm O_2 (RH = 100%)	Pt/C (0.5 mg cm^{-2})	Pt/C (0.5 mg cm^{-2})	Tokuyama A201 (C6D60)	50	145	144
250 sccm H_2 (RH = 95%) / 250 sccm air (RH = 95%)	Pt/C (1 mg cm^{-2})	Pt/C (1 mg cm^{-2})	Tokuyama A201	50	148	145
250 sccm H_2 (RH = 95%) / 250 sccm air (RH = 95%)	Pt/C (1 mg cm^{-2})	Pt/C (1 mg cm^{-2})	C30D70-1.7 AEM	50	168	145
50 sccm H_2 (RH = 100%) / 100 sccm O_2 (RH = 100%)	Pt/C (0.4 mg cm^{-2})	Pt/C (0.4 mg cm^{-2})	PES-MeIm/OH-#4 (FC-#1)	45	0.81	146
50 sccm H_2 (RH = 100%) / 100 sccm O_2 (RH = 100%)	Pt/C (0.4 mg cm^{-2})	Pt/C (0.4 mg cm^{-2})	PES-MeIm/OH-#4 (FC-#2)	45	7.1	146
50 sccm H_2 (RH = 100%) / 100 sccm O_2 (RH = 100%)	Pt/C (0.4 mg cm^{-2})	Pt/C (0.4 mg cm^{-2})	PES-MeIm/OH-#4 (FC-#3)	45	22.5	146

50 sccm H_2 (RH = 100%) / 100 sccm O_2 (RH = 100%)	Pt/C (0.4 mg cm^{-2})	Pt/C (0.4 mg cm^{-2})	PES-MeIm/OH-#4 (FC-#4)	45	21.0	146
50 sccm H_2 (RH = 100%) / 100 sccm O_2 (RH = 100%)	Pt/C (0.4 mg cm^{-2})	Pt/C (0.4 mg cm^{-2})	PES-MeIm/OH-#4 (FC-#5)	45	29.5	146
H_2 (RH = 100%) / O_2 (RH = 100%)	Pt/C (2 mg cm^{-2})	Pt/C (1 mg cm^{-2})	PSf135-ImOH membrane	60	16	147
H_2 (RH = 100%) / O_2 (RH = 100%)	Pt/C (2 mg cm^{-2})	Pt/C (1 mg cm^{-2})	PSf102-ImOH membrane	60	~6	147
600 sccm H_2 (RH = 100%) / 600 sccm air (RH = 100%)	Pt/C (0.4 mg cm^{-2})	Pt/C (0.4 mg cm^{-2})	Alkaline anion exchange membrane 5	50	30	148
80 sccm H_2 (RH = 60%) / 80 sccm O_2 (RH = 60%)	Pt/C (1.0 mg cm^{-2})	Pt/C (1.0 mg cm^{-2})	QPMBV-1 membrane	60	35	153
80 sccm H_2 (RH = 60%) / 80 sccm O_2 (RH = 60%)	Pt/C (1.0 mg cm^{-2})	Pt/C (1.0 mg cm^{-2})	QPMBV-2 membrane	60	~22	153
80 sccm H_2 (RH = 60%) / 80 sccm O_2 (RH = 60%)	Pt/C (1.0 mg cm^{-2})	Pt/C (1.0 mg cm^{-2})	QPMBV-3 membrane	60	~5	153
80 sccm H_2 (RH = 60%) / 80 sccm O_2 (RH = 60%)	Pt/C (1.0 mg cm^{-2})	Pt/C (1.0 mg cm^{-2})	QPMBV-1 membrane	40	~11	153
80 sccm H_2 (RH = 60%) / 80 sccm O_2 (RH = 60%)	Pt/C (1.0 mg cm^{-2})	Pt/C (1.0 mg cm^{-2})	QPMBV-1 membrane	80	59	153
100 sccm H_2 (RH = 80%) / 100 sccm O_2 (RH = 80%)	Pt/C (0.4 mg cm^{-2})	Pt/C (0.4 mg cm^{-2})	QPMBV-APE	50	115	154
100 sccm H_2 (RH = 80%) / 100 sccm O_2 (RH = 80%)	Pt/C (0.4 mg cm^{-2})	Pt/C (0.4 mg cm^{-2})	QPMBV-APE	60	160	154
100 sccm H_2 (RH = 80%) / 100 sccm O_2 (RH = 80%)	Pt/C (0.4 mg cm^{-2})	Pt/C (0.4 mg cm^{-2})	QPMBV-APE	70	180	154
80 sccm H_2 (RH = 80%) / 80 sccm O_2 (RH = 80%)	Pt/C (0.5 mg cm^{-2})	Pt/C (0.5 mg cm^{-2})	QPMBV AEM	50	~15	155
80 sccm H_2 (RH = 80%) / 80 sccm O_2 (RH = 80%)	Pt/C (0.5 mg cm^{-2})	Pt/C (0.5 mg cm^{-2})	QPMBV AEM	60	25	155
80 sccm H_2 (RH = 80%) / 80 sccm O_2 (RH = 80%)	Pt/C (0.5 mg cm^{-2})	Pt/C (0.5 mg cm^{-2})	QPMBV AEM	70	~21	155
100 sccm H_2 (RH = 80%) / 100 sccm O_2 (RH = 80%)	Pt/C (0.4 mg cm^{-2})	Pt/C (0.4 mg cm^{-2})	QPMBV-1 membrane	70	80	156
100 sccm H_2 (RH = 80%) / 100 sccm O_2 (RH = 80%)	Pt/C (0.4 mg cm^{-2})	Pt/C (0.4 mg cm^{-2})	QPMBV-2 membrane	70	~150	156

100 sccm H_2 (RH = 80%) / 100 sccm O_2 (RH = 80%)	Pt/C (0.4 mg cm^{-2})	Pt/C (0.4 mg cm^{-2})	QPMBV-3 membrane	70	180	156
100 sccm H_2 (RH = 80%) / 100 sccm O_2 (RH = 80%)	Pt/C (0.4 mg cm^{-2})	Pt/C (0.4 mg cm^{-2})	QPMBV-1 membrane	60	~30	156
100 sccm H_2 (RH = 80%) / 100 sccm O_2 (RH = 80%)	Pt/C (0.4 mg cm^{-2})	Pt/C (0.4 mg cm^{-2})	QPMBV-2 membrane	60	~95	156
100 sccm H_2 (RH = 80%) / 100 sccm O_2 (RH = 80%)	Pt/C (0.4 mg cm^{-2})	Pt/C (0.4 mg cm^{-2})	QPMBV-3 membrane	60	~105	156
100 sccm H_2 (RH = 70%) / 100 sccm O_2 (RH = 70%)	Pt/C (0.4 mg cm^{-2})	Pt/C (0.4 mg cm^{-2})	QPMBV-2 membrane	70	~115	156
100 sccm H_2 (RH = 60%) / 100 sccm O_2 (RH = 60%)	Pt/C (0.4 mg cm^{-2})	Pt/C (0.4 mg cm^{-2})	QPMBV-2 membrane	70	~75	156
100 sccm H_2 (RH = 50%) / 100 sccm O_2 (RH = 50%)	Pt/C (0.4 mg cm^{-2})	Pt/C (0.4 mg cm^{-2})	QPMBV-2 membrane	70	~50	156
100 sccm H_2 (RH = 40%) / 100 sccm O_2 (RH = 40%)	Pt/C (0.4 mg cm^{-2})	Pt/C (0.4 mg cm^{-2})	QPMBV-2 membrane	70	~15	156
H_2 (RH = 100%) / O_2 (RH = 100%)	Pt/C (0.17 mg cm^{-2})	Pt/C (0.17 mg cm^{-2})	Anion exchange crosslinked membrane (cell 1)	25	100	158
H_2 (RH = 100%) / O_2 (RH = 100%)	Pt/C (0.17 mg cm^{-2})	Pt/C (0.17 mg cm^{-2})	Anion exchange crosslinked membrane (cell 2)	25	~100	158
H_2 (RH = 100%) / O_2 (RH = 100%)	Pt/C (0.17 mg cm^{-2})	Pt/C (0.17 mg cm^{-2})	Anion exchange crosslinked membrane (cell 3)	25	~95	158
H_2 (RH = 100%) / O_2 (RH = 100%)	Pt/C (0.17 mg cm^{-2})	Pt/C (0.17 mg cm^{-2})	Anion exchange crosslinked membrane (cell 4)	25	~90	158
50 sccm H_2 (RH = 100%) / 50 sccm air (RH = 100%)	Pt/C (unmodified) (2 mg cm^{-2})	Pt/C (unmodified) (2 mg cm^{-2})	$Sn_{0.92}Sb_{0.08}P_2O_7$-PTFE composite membrane	75	15	160
50 sccm H_2 (RH = 100%) / 50 sccm air (RH = 100%)	Pt/C (unmodified) (2 mg cm^{-2})	Pt/C (unmodified) (2 mg cm^{-2})	$Sn_{0.92}Sb_{0.08}P_2O_7$-PTFE composite membrane	100	~20	160
50 sccm H_2 (RH = 100%) / 50 sccm air (RH = 100%)	Pt/C (unmodified) (2 mg cm^{-2})	Pt/C (unmodified) (2 mg cm^{-2})	$Sn_{0.92}Sb_{0.08}P_2O_7$-PTFE composite membrane	125	~28	160

50 sccm H_2 (RH = 100%) / 50 sccm air (RH = 100%)	Pt/C (unmodified) (2 mg cm^{-2})	Pt/C (unmodified) (2 mg cm^{-2})	$Sn_{0.92}Sb_{0.08}P_2O_7$-PTFE composite membrane	150	~35	160
50 sccm H_2 (RH = 100%) / 50 sccm air (RH = 100%)	Pt/C (unmodified) (2 mg cm^{-2})	Pt/C (unmodified) (2 mg cm^{-2})	$Sn_{0.92}Sb_{0.08}P_2O_7$-PTFE composite membrane	175	~50	160
50 sccm H_2 (RH = 100%) / 50 sccm air (RH = 100%)	Pt/C (unmodified) (2 mg cm^{-2})	Pt/C (unmodified) (2 mg cm^{-2})	$Sn_{0.92}Sb_{0.08}P_2O_7$-PTFE composite membrane	200	61	160
50 sccm H_2 (RH = 100%) / 50 sccm air (RH = 100%)	Pt/C (modified) (2 mg cm^{-2})	Pt/C (modified) (2 mg cm^{-2})	$Sn_{0.92}Sb_{0.08}P_2O_7$-PTFE composite membrane	75	76	160
50 sccm H_2 (RH = 100%) / 50 sccm air (RH = 100%)	Pt/C (modified) (2 mg cm^{-2})	Pt/C (modified) (2 mg cm^{-2})	$Sn_{0.92}Sb_{0.08}P_2O_7$-PTFE composite membrane	100	94	160
50 sccm H_2 (RH = 100%) / 50 sccm air (RH = 100%)	Pt/C (modified) (2 mg cm^{-2})	Pt/C (modified) (2 mg cm^{-2})	$Sn_{0.92}Sb_{0.08}P_2O_7$-PTFE composite membrane	125	114	160
50 sccm H_2 (RH = 100%) / 50 sccm air (RH = 100%)	Pt/C (modified) (2 mg cm^{-2})	Pt/C (modified) (2 mg cm^{-2})	$Sn_{0.92}Sb_{0.08}P_2O_7$-PTFE composite membrane	150	130	160
50 sccm H_2 (RH = 100%) / 50 sccm air (RH = 100%)	Pt/C (modified) (2 mg cm^{-2})	Pt/C (modified) (2 mg cm^{-2})	$Sn_{0.92}Sb_{0.08}P_2O_7$-PTFE composite membrane	175	132	160
50 sccm H_2 (RH = 100%) / 50 sccm air (RH = 100%)	Pt/C (modified) (2 mg cm^{-2})	Pt/C (modified) (2 mg cm^{-2})	$Sn_{0.92}Sb_{0.08}P_2O_7$-PTFE composite membrane	200	147	160
100 sccm H_2 (RH = 100%) / 200 sccm O_2 (RH = 100%)	Pt/C (0.4 mg cm^{-2})	Pt/C (0.4 mg cm^{-2})	ACDH96 membrane (electrode1)	50	252	161
100 sccm H_2 (RH = 100%) / 200 sccm O_2 (RH = 100%)	Pt/C (0.4 mg cm^{-2})	Pt/C (0.4 mg cm^{-2})	ACDH98 membrane	50	278	161
100 sccm H_2 (RH = 100%) / 200 sccm O_2 (RH = 100%)	Pt/C (0.4 mg cm^{-2})	Pt/C (0.4 mg cm^{-2})	CD96 membrane	50	237	161
100 sccm H_2 (RH = 100%) / 200 sccm O_2 (RH = 100%)	Pt/C (0.4 mg cm^{-2})	Pt/C (0.4 mg cm^{-2})	ACDH96 membrane (electrode2)	50	370	161
H_2 (RH = 100%) / O_2 (RH = 100%)	Pt/C (3.4 mg cm^{-2})	Pt/C (6.5 mg cm^{-2})	ATM-PP (ionomer: M-Nafion-FA-TMG)	80	577	162

H_2 (RH = 100%) / air (RH = 100%)	Pt/C (3.4 mg cm^{-2})	Pt/C (6.5 mg cm^{-2})	ATM-PP (ionomer: M-Nafion-FA-TMG)	80	466	162
H_2 (RH = 100%) / O_2 (RH = 100%)	Pt/C (3.4 mg cm^{-2})	Pt/C (6.5 mg cm^{-2})	ATM-PP (ionomer : ATM-PP)	80	335	162
200 sccm H_2 (RH = 95%) / 200 sccm O_2 (RH = 95%)	Pt/C (0.5 mg cm^{-2})	Pt/C (0.5 mg cm^{-2})	PSF-DMP AEM (IEC = 1.81 mmol g^{-1})	70	~8	165
200 sccm H_2 (RH = 95%) / 200 sccm O_2 (RH = 95%)	Pt/C (0.5 mg cm^{-2})	Pt/C (0.5 mg cm^{-2})	PSF-TMA AEM (IEC = 1.79 mmol g^{-1})	70	46	165
200 sccm H_2 (RH = 95%) / 200 sccm O_2 (RH = 95%)	Pt/C (0.5 mg cm^{-2})	Pt/C (0.5 mg cm^{-2})	PSF-TMA AEM (IEC = 2.05 mmol g^{-1})	70	179	165
200 sccm H_2 (RH = 95%) / 200 sccm air (RH = 95%)	Pt/C (0.5 mg cm^{-2})	Pt/C (0.5 mg cm^{-2})	PSF-DMP AEM (IEC = 1.81 mmol g^{-1})	70	~53	165
200 sccm H_2 (RH = 95%) / 200 sccm air (RH = 95%)	Pt/C (0.5 mg cm^{-2})	Pt/C (0.5 mg cm^{-2})	PSF-TMA AEM (IEC = 1.79 mmol g^{-1})	70	~2	165
200 sccm H_2 (RH = 95%) / 200 sccm air (RH = 95%)	Pt/C (0.5 mg cm^{-2})	Pt/C (0.5 mg cm^{-2})	PSF-TMA AEM (IEC = 2.05 mmol g^{-1})	70	~40	165
50 sccm H_2 (RH = 100%) / 100 sccm O_2 (RH = 100%)	Pt/C (2 mg cm^{-2})	Pt/C (2 mg cm^{-2})	AEM based on [VBMI]Cl	30	33	170
20 sccm H_2 / Air	Pt/C (0.4 mg cm^{-2})	Pt/C (0.4 mg cm^{-2})	solid alkaline electrolyte membrane (1 M KOH)	20	~10	172
20 sccm H_2 / Air	Pt/C (0.4 mg cm^{-2})	Pt/C (0.4 mg cm^{-2})	solid alkaline electrolyte membrane (1 M KOH)	40	~17	172
20 sccm H_2 / Air	Pt/C (0.4 mg cm^{-2})	Pt/C (0.4 mg cm^{-2})	solid alkaline electrolyte membrane (1 M KOH)	60	~22	172
20 sccm H_2 / Air	Pt/C (0.4 mg cm^{-2})	Pt/C (0.4 mg cm^{-2})	solid alkaline electrolyte membrane (1 M KOH)	80	~28	172
20 sccm H_2 / Air	Pt/C (0.4 mg cm^{-2})	Pt/C (0.4 mg cm^{-2})	solid alkaline electrolyte membrane (1 M TMAOH)	20	13.6	172

20 sccm H_2 / Air	Pt/C (0.4 mg cm^{-2})	Pt/C (0.4 mg cm^{-2})	solid alkaline electrolyte membrane (1 M TEAOH)	20	~12.5	172
20 sccm H_2 / Air	Pt/C (0.4 mg cm^{-2})	Pt/C (0.4 mg cm^{-2})	solid alkaline electrolyte membrane (0.5 M TPrAOH)	20	~12	172
20 sccm H_2 / Air	Pt/C (0.4 mg cm^{-2})	Pt/C (0.4 mg cm^{-2})	solid alkaline electrolyte membrane (0.05 M TMAOH)	20	2.4	172
20 sccm H_2 / Air	Pt/C (0.4 mg cm^{-2})	Pt/C (0.4 mg cm^{-2})	solid alkaline electrolyte membrane (0.2 M TMAOH)	20	7.0	172
20 sccm H_2 / Air	Pt/C (0.4 mg cm^{-2})	Pt/C (0.4 mg cm^{-2})	solid alkaline electrolyte membrane (0.6 M TMAOH)	20	13.5	172
20 sccm H_2 / Air	Pt/C (0.4 mg cm^{-2})	Pt/C (0.4 mg cm^{-2})	solid alkaline electrolyte membrane (1 M TMAOH)	40	16.3	172
20 sccm H_2 / Air	Pt/C (0.4 mg cm^{-2})	Pt/C (0.4 mg cm^{-2})	solid alkaline electrolyte membrane (1 M TMAOH)	60	18.6	172
20 sccm H_2 / Air	Pt/C (0.4 mg cm^{-2})	Pt/C (0.4 mg cm^{-2})	solid alkaline electrolyte membrane (1 M TMAOH)	80	20.2	172
20 sccm H_2 / Air	Pt/C (0.4 mg cm^{-2})	Pt/C (0.4 mg cm^{-2})	solid alkaline electrolyte membrane (1 M $TMACO_3$ PH=8)	20	4.1	172
20 sccm H_2 / Air	Pt/C (0.4 mg cm^{-2})	Pt/C (0.4 mg cm^{-2})	solid alkaline electrolyte membrane (1 M TMA-Ac PH=7.6)	20	2.1	172
20 sccm H_2 / Air	Pt/C (0.4 mg cm^{-2})	Pt/C (0.4 mg cm^{-2})	solid alkaline electrolyte membrane (1 M TMA-SO_4 PH=4.6)	20	1.1	172
20 sccm H_2 / Air	Pt/C (0.4 mg cm^{-2})	Pt/C (0.4 mg cm^{-2})	solid alkaline electrolyte membrane (1 M $TMACO_3$ PH=8)	40	~4.8	172
20 sccm H_2 / Air	Pt/C (0.4 mg cm^{-2})	Pt/C (0.4 mg cm^{-2})	solid alkaline electrolyte membrane	60	~6.5	172

			(1 M $TMACO_3$ PH=8)			
20 sccm H_2 / Air	Pt/C (0.4 mg cm^{-2})	Pt/C (0.4 mg cm^{-2})	solid alkaline electrolyte membrane (1 M $TMACO_3$ PH=8)	80	9.7	172
20 sccm H_2 / Air	Pt/C (0.4 mg cm^{-2})	Pt/C (0.4 mg cm^{-2})	solid alkaline electrolyte membrane (1 M TMA-Ac PH=7.6)	40	~2.2	172
20 sccm H_2 / Air	Pt/C (0.4 mg cm^{-2})	Pt/C (0.4 mg cm^{-2})	solid alkaline electrolyte membrane (1 M TMA-Ac PH=7.6)	60	~2.6	172
20 sccm H_2 / Air	Pt/C (0.4 mg cm^{-2})	Pt/C (0.4 mg cm^{-2})	solid alkaline electrolyte membrane (1 M TMA-Ac PH=7.6)	80	~3.0	172
20 sccm H_2 / Air	Pt/C (0.4 mg cm^{-2})	Pt/C (0.4 mg cm^{-2})	solid alkaline electrolyte membrane (1 M TMA-SO_4 PH=4.6)	40	~1.2	172
20 sccm H_2 / Air	Pt/C (0.4 mg cm^{-2})	Pt/C (0.4 mg cm^{-2})	solid alkaline electrolyte membrane (1 M TMA-SO_4 PH=4.6)	60	~1.4	172
20 sccm H_2 / Air	Pt/C (0.4 mg cm^{-2})	Pt/C (0.4 mg cm^{-2})	solid alkaline electrolyte membrane (1 M TMA-SO_4 PH=4.6)	80	~1.6	172
2000 sccm H_2 (RH = 100%) / 2000 sccm O_2 (RH = 100%)	Pt/C (0.5 mg cm^{-2})	Pt/C (0.5 mg cm^{-2})	ETFE-based AAEM	60	110	185
2000 sccm H_2 (RH = 100%) / 2000 sccm O_2 (RH = 100%)	Pt/C (0.5 mg cm^{-2})	Pt/C (0.5 mg cm^{-2})	ETFE-based AAEM	50	90	185
2000 sccm H_2 (RH = 100%) / 2000 sccm O_2 (RH = 100%)	Pt/C (0.5 mg cm^{-2})	Pt/C (0.5 mg cm^{-2})	4 mg cm^{-2} catalysed AAEM	50	130	185
H_2 / O_2	Pt/C (0.2 mg cm^{-2})	Pt/C (0.2 mg cm^{-2})	PVA membrane	R.T.	~5.0	187
H_2 / O_2	Pt/C (0.2 mg cm^{-2})	Pt/C (0.2 mg cm^{-2})	γ-PVA membrane	R.T.	~6.4	187
H_2 / O_2	Pt/C (0.2 mg cm^{-2})	Pt/C (0.2 mg cm^{-2})	PVA-Mo membrane	R.T.	~6.8	187
600 sccm H_2 (RH = 100%)	Pt/C	Pt/C	PVBTMA-OH^- (1)	50	~140	188

/ 600 sccm O_2 (RH = 100%)	(0.4 mg cm^{-2})	(0.4 mg cm^{-2})	AAEM			
600 sccm H_2 (RH = 100%) / 600 sccm O_2 (RH = 100%)	Pt/C (0.4 mg cm^{-2})	Pt/C (0.4 mg cm^{-2})	PVBMI-OH^- (1) AAEM	50	~0.8	188
600 sccm H_2 (RH = 100%) / 600 sccm O_2 (RH = 100%)	Pt/C (0.4 mg cm^{-2})	Pt/C (0.4 mg cm^{-2})	PVBMI-OH^- (2) AAEM	50	~1.1	188
1000 sccm H_2 (RH = 100%) / 1000 sccm O_2 (RH = 100%)	PtRu/C (0.4 mg_{pt} cm^{-2})	Pt/C (0.4 mg cm^{-2})	E-6 AAEM	60	1160	190
1000 sccm H_2 (RH = 100%) / 1000 sccm O_2 (RH = 100%)	PtRu/C (0.4 mg_{pt} cm^{-2})	Pt/C (0.4 mg cm^{-2})	E-R AAEM	60	910	190
1000 sccm H_2 (RH = 100%) / 1000 sccm O_2 (RH = 100%)	PtRu/C (0.4 mg_{pt} cm^{-2})	Pt/C (0.4 mg cm^{-2})	LDPE-AAEM	80	1450	191
1000 sccm H_2 (RH = 100%) / 1000 sccm O_2 (RH = 100%)	PtRu/C (0.4 mg_{pt} cm^{-2})	Pt/C (0.4 mg cm^{-2})	ETFE-AAEM	80	1210	191
1000 sccm H_2 (RH = 68%) / 1000 sccm O_2 (RH = 68%)	PtRu/C (0.4 mg_{pt} cm^{-2})	Pt/C (0.4 mg cm^{-2})	LDPE-AAEM	60	960	191
1000 sccm H_2 (RH = 68%) / 1000 sccm O_2 (RH = 68%)	PtRu/C (0.4 mg_{pt} cm^{-2})	Pt/C (0.4 mg cm^{-2})	ETFE-AAEM	60	910	191
1000 sccm H_2 (RH = 100%) / 1000 sccm O_2 (RH = 100%)	PtRu/C (0.4 mg_{pt} cm^{-2})	Ag/C (0.8 mg cm^{-2})	LDPE-AAEM	80	~980	191
1000 sccm H_2 (RH = 100%) / 1000 sccm air (RH = 100%)	PtRu/C (0.4 mg_{pt} cm^{-2})	Pt/C (0.4 mg cm^{-2})	LDPE-AAEM	80	630	191
1000 sccm H_2 (RH = 75%) / 1000 sccm O_2 (RH = 85%)	PtRu/C (0.67 mg cm^{-2})	Pt/C (0.53 mg cm^{-2})	ETFE-g-VBCTMA AAEM	60	1400	205
100 sccm H_2 (RH = 100%) / 100 sccm O_2 (RH = 100%)	Pt/C (0.4 mg cm^{-2})	Pt/C (0.4 mg cm^{-2})	10% crosslinked QPMV-PDVB AAEM	50	46	207

100 sccm H_2 (RH = 100%) / 100 sccm O_2 (RH = 100%)	Pt/C (0.4 mg cm^{-2})	Pt/C (0.4 mg cm^{-2})	5% crosslinked QPMV-PDVB AAEM	50	~45	207
100 sccm H_2 (RH = 100%) / 100 sccm O_2 (RH = 100%)	Pt/C (0.4 mg cm^{-2})	Pt/C (0.4 mg cm^{-2})	0% crosslinked QPMV-PDVB AAEM	50	~55	207
H_2 / O_2	Pt/C (3 mg cm^{-2})	Pt/C (3 mg cm^{-2})	F-PAE AEM	60	193	208
H_2 / O_2	Pt/C (3 mg cm^{-2})	Pt/C (3 mg cm^{-2})	ATM-PP 1 AEM	60	205	208
H_2 / O_2	Pt/C (3 mg cm^{-2})	Pt/C (3 mg cm^{-2})	ATM-PP 2 AEM	60	80	208
H_2 / O_2	Pt/C (3 mg cm^{-2})	Pt/C (3 mg cm^{-2})	ATM-PP 3 AEM	60	~20	208
400 sccm H_2 (RH = 100%) / 400 sccm O_2 (RH = 100%)	PtRu/C (0.4 mg cm^{-2})	Pt/C (0.4 mg cm^{-2})	aQAPS-S_8 membrane	60	1000	210
400 sccm H_2 (RH = 100%) / 400 sccm O_2 (RH = 100%)	Pt/C (0.4 mg cm^{-2})	Pt/C (0.4 mg cm^{-2})	aQAPS-S_8 membrane	60	870	210

Table 3 Selected hydrogen/oxygen fuel cell performance with different AEMs reported in open literature.

Fuel/Oxidant	Anode	Cathode	Membrane	T (°C)	P(mW cm^{-2})	Ref.
H_2 (RH = 100%) / O_2 (RH = 100%)	Pt/C (0.4 mg cm^{-2})	Pt/C (0.4 mg cm^{-2})	Anion exchange polymer membrane (ionomer: TMA)	50	478	171
H_2 (RH = 100%) / O_2 (RH	Pt/C	Pt/C	Anion exchange polymer	50	236	171

= 100%)	(0.4 mg cm^{-2})	(0.4 mg cm^{-2})	membrane (ionomer: TMHDA)			
H_2 (RH = 100%) / O_2 (RH = 100%)	Pt/C (0.4 mg cm^{-2})	Pt/C (0.4 mg cm^{-2})	Anion exchange polymer membrane (ionomer: DABCO)	50	116	171
H_2 (RH = 100%) / O_2 (RH = 100%)	Pt/C (0.4 mg cm^{-2})	Pt/C (0.4 mg cm^{-2})	Anion exchange polymer membrane (ionomer: TEA)	50	100	171
H_2 (RH = 100%) / O_2 (RH = 100%)	Pt/C (0.4 mg cm^{-2})	Pt/C (0.4 mg cm^{-2})	Anion exchange polymer membrane (ionomer: DMS)	50	58	171
200 sccm H_2 (RH = 100%) / 200 sccm O_2 (RH = 100%)	Pt/C (1.28 mg cm^{-2})	Pt/C (1.28 mg cm^{-2})	Tokuyama A901 (ionomer: QSEBS-L)	50	~70	192
200 sccm H_2 (RH = 100%) / 200 sccm O_2 (RH = 100%)	Pt/C (1.28 mg cm^{-2})	Pt/C (1.28 mg cm^{-2})	Tokuyama A901 (ionomer: QSEBS-M)	50	210	192
200 sccm H_2 (RH = 100%) / 200 sccm O_2 (RH = 100%)	Pt/C (1.28 mg cm^{-2})	Pt/C (1.28 mg cm^{-2})	Tokuyama A901 (ionomer: QSEBS-H)	50	~200	192
200 sccm H_2 (RH = 100%) / 200 sccm O_2 (RH = 100%)	Pt/C (1.28 mg cm^{-2})	Pt/C (1.28 mg cm^{-2})	Tokuyama A901 (ionomer: QBSF)	50	30	192
1000 sccm H_2 (RH = 95%) / 2000 sccm air (RH = 95%)	Pt/C (0.45 mg cm^{-2})	Pt/C (0.45 mg cm^{-2})	Tokuyama A2012 AEM (ionomer : PyPBI)	50	256	193
1000 sccm H_2 (RH = 95%) / 2000 sccm O_2 (RH = 95%)	Pt/C (0.45 mg cm^{-2})	Pt/C (0.45 mg cm^{-2})	Tokuyama A2012 AEM (ionomer : AS-4)	50	174	193
100 sccm H_2 (RH = 100%) / 200 sccm O_2 (RH = 100%)	Pt/C (0.4 mg cm^{-2})	Pt/C (0.4 mg cm^{-2})	Tokuyama A201 (ionomer content: 10) (solvent : IPA)	50	~85	194
100 sccm H_2 (RH = 100%) / 200 sccm O_2 (RH = 100%)	Pt/C (0.4 mg cm^{-2})	Pt/C (0.4 mg cm^{-2})	Tokuyama A201 (ionomer content: 15) (solvent : IPA)	50	~330	194

100 sccm H_2 (RH = 100%) / 200 sccm O_2 (RH = 100%)	Pt/C (0.4 mg cm^{-2})	Pt/C (0.4 mg cm^{-2})	Tokuyama A201 (ionomer content: 20) (solvent : IPA)	50	358	194
100 sccm H_2 (RH = 100%) / 200 sccm O_2 (RH = 100%)	Pt/C (0.4 mg cm^{-2})	Pt/C (0.4 mg cm^{-2})	Tokuyama A201 (ionomer content: 25) (solvent : IPA)	50	~135	194
100 sccm H_2 (RH = 100%) / 200 sccm O_2 (RH = 100%)	Pt/C (0.4 mg cm^{-2})	Pt/C (0.4 mg cm^{-2})	Tokuyama A201 (ionomer content: 20) (solvent : EtOH)	50	321	194
100 sccm H_2 (RH = 100%) / 200 sccm O_2 (RH = 100%)	Pt/C (0.4 mg cm^{-2})	Pt/C (0.4 mg cm^{-2})	Tokuyama A201 (ionomer content: 20) (solvent : PA)	50	220	194
100 sccm H_2 (RH = 100%) / 200 sccm O_2 (RH = 100%)	Pt/C (0.4 mg cm^{-2})	Pt/C (0.4 mg cm^{-2})	Tokuyama A201 (ionomer content: 20) (solvent : NBA)	50	407	194
H_2 (RH = 75%) / O_2 (RH = 75%)	Pt/C (50 ug cm^{-2})	Pt/C (50 ug cm^{-2})	porous silver membrane (Laminated)	50	~5	196
H_2 (RH = 75%) / O_2 (RH = 75%)	Pt/C (50 ug cm^{-2})	Pt/C (50 ug cm^{-2})	porous silver membrane (Not Laminated)	50	~7.5	196
H_2 (RH = 75%) / O_2 (RH = 75%)	Pt/C (50 ug cm^{-2})	Pt/C (50 ug cm^{-2})	porous silver membrane (Not Laminated, Tokuyama ionomer)	50	30	196
H_2 (RH = 75%) / O_2 (RH = 75%)	Pt/C (50 ug cm^{-2})	Pt/C (50 ug cm^{-2})	porous silver membrane (Nafion ionomer in catalyst layer + AS4 interface layer)	50	30	196
H_2 (RH = 75%) / O_2 (RH = 75%)	Pt/C (50 ug cm^{-2})	Pt/C (50 ug cm^{-2})	porous silver membrane (AS4 ionomer in catalyst layer + AS4 interface layer)	50	60	196
H_2 (RH = 0%) / O_2 (RH = 0%)	Pt/C (0.5 mg cm^{-2})	Pt/C (0.5 mg cm^{-2})	MEA-2	70	~180	197
H_2 (RH = 50%) / O_2 (RH = 50%)	Pt/C (0.5 mg cm^{-2})	Pt/C (0.5 mg cm^{-2})	MEA-2	70	~100	197
H_2 (RH = 100%) / O_2 (RH = 100%)	Pt/C (0.5 mg cm^{-2})	Pt/C (0.5 mg cm^{-2})	MEA-2	70	~56	197
200 sccm H_2 (RH = 100%)	Pt/C	Ag/P	FAA commercial	80	208	198

/ 200 sccm O_2 (RH = 100%)	(0.5 mg cm^{-2})	(0.5 mg cm^{-2})	membrane			
200 sccm H_2 (RH = 100%) / 200 sccm O_2 (RH = 100%)	Pt/C (0.5 mg cm^{-2})	Pt/C (0.5 mg cm^{-2})	FAA commercial membrane	80	196	198
200 sccm H_2 (RH = 100%) / 200 sccm O_2 (RH = 100%)	Ni/C (5 mg cm^{-2})	Ag/TPQPOH (0.5 mg cm^{-2})	TPQPOH152 membrane	70	76	198
H_2 (RH = 100%) / O_2 (RH = 100%)	Pt/C (0.5 mg cm^{-2})	Pt/C (0.5 mg cm^{-2})	Nafion membrane and AEM (thin-film method)	70	44	199
H_2 (RH = 100%) / O_2 (RH = 100%)	Pt/C (0.5 mg cm^{-2})	Pt/C (0.5 mg cm^{-2})	Nafion membrane and AEM (ionomer impregnation)	70	125	199
H_2 (RH = 100%) / O_2 (RH = 100%)	Pt/C (0.5 mg cm^{-2})	Pt/C (0.5 mg cm^{-2})	Nafion membrane and AEM (ionomer impregnation with 9% PTFE)	70	315	199
H_2 (RH = 0%) / O_2 (RH = 0%)	Pt/C (0.5 mg cm^{-2})	Pt/C (0.5 mg cm^{-2})	Nafion membrane and AEM (thin-film method)	70	144	199
H_2 (RH = 0%) / O_2 (RH = 0%)	Pt/C (0.5 mg cm^{-2})	Pt/C (0.5 mg cm^{-2})	Nafion membrane and AEM (ionomer impregnation)	70	191	199
H_2 (RH = 0%) / O_2 (RH = 0%)	Pt/C (0.5 mg cm^{-2})	Pt/C (0.5 mg cm^{-2})	Nafion membrane and AEM (ionomer impregnation with 9% PTFE)	70	369	199
H_2 (RH = 100%) / O_2 (RH = 100%)	Pt/C (0.5 mg cm^{-2})	Pt/C (0.5 mg cm^{-2})	AEM and Nafion membrane (thin-film method)	70	95	199
H_2 (RH = 100%) / O_2 (RH = 100%)	Pt/C (0.5 mg cm^{-2})	Pt/C (0.5 mg cm^{-2})	AEM and Nafion membrane (ionomer impregnation)	70	375	199
H_2 (RH = 100%) / O_2 (RH = 100%)	Pt/C (0.5 mg cm^{-2})	Pt/C (0.5 mg cm^{-2})	QAPSF	25	~160	200
H_2 (RH = 100%) / O_2 (RH = 100%)	Pt/C (0.5 mg cm^{-2})	Pt/C (0.5 mg cm^{-2})	QAPAE-4	25	~230	200

H_2 (RH = 100%) / O_2 (RH = 100%)	Pt/C (0.5 mg cm^{-2})	Pt/C (0.5 mg cm^{-2})	QAPSF	60	215	200
H_2 (RH = 100%) / O_2 (RH = 100%)	Pt/C (0.5 mg cm^{-2})	Pt/C (0.5 mg cm^{-2})	QAPAE-4	60	315	200
2000 sccm H_2 (RH = 100%) / 2000 sccm O_2 (RH = 100%)	Pt/C (20 wt%) (0.5 mg cm^{-2}) XC-72 (2 mg cm^{-2})	Pt/C (20 wt%) (0.5 mg cm^{-2}) XC-72 (2 mg cm^{-2})	MEA-A (Solvay AAEM)	50	55	202
2000 sccm H_2 (RH = 100%) / 2000 sccm O_2 (RH = 100%)	Pt/C (20 wt%) (0.53 mg cm^{-2}) XC-72 (2.1 mg cm^{-2})	Pt/C (20 wt%) (0.53 mg cm^{-2}) XC-72 (2.1 mg cm^{-2})	MEA-B (Solvay AAEM)	50	25	202
2000 sccm H_2 (RH = 100%) / 2000 sccm O_2 (RH = 100%)	Pt/C (20 wt%) (0.56 mg cm^{-2}) XC-72 (2.2 mg cm^{-2})	Pt/C (20 wt%) (0.56 mg cm^{-2}) XC-72 (2.2 mg cm^{-2})	MEA-C (Solvay AAEM)	50	34	202
2000 sccm H_2 (RH = 100%) / 2000 sccm O_2 (RH = 100%)	Pt/C (20 wt%) (0.55 mg cm^{-2}) XC-72 (2.2 mg cm^{-2})	Pt/C (20 wt%) (0.55 mg cm^{-2}) XC-72 (2.2 mg cm^{-2})	MEA-D (Solvay AAEM)	50	32	202
2000 sccm H_2 (RH = 100%) / 2000 sccm O_2 (RH = 100%)	Pt/C (20 wt%) (0.57 mg cm^{-2}) XC-72 (2.3 mg cm^{-2})	Pt/C (20 wt%) (0.57 mg cm^{-2}) XC-72 (2.3 mg cm^{-2})	MEA-E (Solvay AAEM)	50	35	202
2000 sccm H_2 (RH = 100%) / 2000 sccm O_2 (RH = 100%)	Pt/C (20 wt%) (0.55 mg cm^{-2}) XC-72 (2.2 mg cm^{-2})	Pt/C (20 wt%) (0.55 mg cm^{-2}) XC-72 (2.2 mg cm^{-2})	MEA-F (Solvay AAEM)	50	80	202
2000 sccm H_2 (RH = 100%) / 2000 sccm O_2 (RH = 100%)	Pt/C (20 wt%) (0.57 mg cm^{-2}) XC-72 (2.3 mg cm^{-2})	Pt/C (20 wt%) (0.57 mg cm^{-2}) XC-72 (2.3 mg cm^{-2})	MEA-G (Solvay AAEM)	50	75	202
2000 sccm H_2 (RH = 100%) / 2000 sccm O_2 (RH = 100%)	Pt/C (20 wt%) (0.49 mg cm^{-2}) XC-72 (2.0 mg cm^{-2})	Pt/C (20 wt%) (0.49 mg cm^{-2}) XC-72 (2.0 mg cm^{-2})	MEA-H (Solvay AAEM)	50	61	202
2000 sccm H_2 (RH = 100%) / 2000 sccm O_2 (RH	XC-72 (2.2 mg cm^{-2})	XC-72 (2.2 mg cm^{-2})	MEA-I (Solvay AAEM)	50	22	202

= 100%)						
2000 sccm H_2 (RH = 100%) / 2000 sccm O_2 (RH = 100%)	Pt/C (20 wt%) (0.55 mg cm^{-2}) XC-72 (2.2 mg cm^{-2})	Pt/C (20 wt%) (0.55 mg cm^{-2}) XC-72 (2.2 mg cm^{-2})	MEA-J (Surrey AAEM)	50	104	202
H_2 (RH = 100%) / air (RH = 100%)	Pt/C (0.4 mg cm^{-2})	Pt/C (0.4 mg cm^{-2})	57 um LDPE-VBC membrane	50	255	203
H_2 (RH = 100%) / air (1 bar gauge) (RH = 100%)	Pt/C (0.4 mg cm^{-2})	Pt/C (0.4 mg cm^{-2})	57 um LDPE-VBC membrane	50	300	203
H_2 (RH = 100%) / air (1 bar gauge) (RH = 100%)	Pt/C (0.4 mg cm^{-2})	Pt/C (0.4 mg cm^{-2})	57 um LDPE-VBC membrane	60	337	203
H_2 (RH = 100%) / O_2 (RH = 100%)	Pt/C (0.4 mg cm^{-2})	Pt/C (0.4 mg cm^{-2})	57 um LDPE-VBC membrane	60	390	203
200 sccm H_2 (RH = 100%) / 200 sccm O_2 (RH = 100%)	Pt/C (0.5 mg cm^{-2})	Pt/C (0.5 mg cm^{-2})	FAA-3 membrane (0.6 activated) (25% FAA ionomer) (150 cN m)	50	71	209
200 sccm H_2 (RH = 100%) / 200 sccm O_2 (RH = 100%)	Pt/C (0.5 mg cm^{-2})	Pt/C (0.5 mg cm^{-2})	FAA-3 membrane (0.1 activated) (25% FAA ionomer) (150 cN m)	50	75	209
200 sccm H_2 (RH = 100%) / 200 sccm O_2 (RH = 100%)	Pt/C (0.5 mg cm^{-2})	Pt/C (0.5 mg cm^{-2})	FAA-3 membrane (VI activated) (25% FAA ionomer) (150 cN m)	50	110	209
200 sccm H_2 (RH = 100%) / 200 sccm O_2 (RH = 100%)	Pt/C (0.5 mg cm^{-2})	Pt/C (0.5 mg cm^{-2})	FAA-3 membrane (VI activated) (25% FAA ionomer) (150 cN m)	40	41	209
200 sccm H_2 (RH = 100%) / 200 sccm O_2 (RH = 100%)	Pt/C (0.5 mg cm^{-2})	Pt/C (0.5 mg cm^{-2})	FAA-3 membrane (VI activated) (25% FAA ionomer) (150 cN m)	50	112	209
200 sccm H_2 (RH = 100%) / 200 sccm O_2 (RH = 100%)	Pt/C (0.5 mg cm^{-2})	Pt/C (0.5 mg cm^{-2})	FAA-3 membrane (VI activated) (25% FAA ionomer) (150 cN m)	60	176	209
200 sccm H_2 (RH = 100%)	Pt/C	Pt/C	FAA-3 membrane	60	140	209

/ 200 sccm O_2 (RH = 100%)	(0.4 mg cm^{-2})	(0.4 mg cm^{-2})	(VI activated) (25% FAA ionomer) (150 cN m)			
200 sccm H_2 (RH = 100%) / 200 sccm O_2 (RH = 100%)	Pt/C (0.5 mg cm^{-2})	Pt/C (0.5 mg cm^{-2})	FAA-3 membrane (VI activated) (25% FAA ionomer) (150 cN m)	60	178	209
200 sccm H_2 (RH = 100%) / 200 sccm O_2 (RH = 100%)	Pt/C (0.6 mg cm^{-2})	Pt/C (0.6 mg cm^{-2})	FAA-3 membrane (VI activated) (25% FAA ionomer) (150 cN m)	60	181	209
200 sccm H_2 (RH = 100%) / 200 sccm O_2 (RH = 100%)	Pt/C (0.8 mg cm^{-2})	Pt/C (0.8 mg cm^{-2})	FAA-3 membrane (VI activated) (25% FAA ionomer) (150 cN m)	60	201	209
200 sccm H_2 (RH = 100%) / 200 sccm O_2 (RH = 100%)	Pt/C (1.0 mg cm^{-2})	Pt/C (1.0 mg cm^{-2})	FAA-3 membrane (VI activated) (25% FAA ionomer) (150 cN m)	60	194	209
200 sccm H_2 (RH = 100%) / 200 sccm O_2 (RH = 100%)	Pt/C (0.8 mg cm^{-2})	Pt/C (0.8 mg cm^{-2})	FAA-3 membrane (VI activated) (15% FAA ionomer) (150 cN m)	60	77	209
200 sccm H_2 (RH = 100%) / 200 sccm O_2 (RH = 100%)	Pt/C (0.8 mg cm^{-2})	Pt/C (0.8 mg cm^{-2})	FAA-3 membrane (VI activated) (25% FAA ionomer) (150 cN m)	60	176	209
200 sccm H_2 (RH = 100%) / 200 sccm O_2 (RH = 100%)	Pt/C (0.8 mg cm^{-2})	Pt/C (0.8 mg cm^{-2})	FAA-3 membrane (VI activated) (45% FAA ionomer) (150 cN m)	60	153	209
200 sccm H_2 (RH = 100%) / 200 sccm O_2 (RH = 100%)	Pt/C (0.8 mg cm^{-2})	Pt/C (0.8 mg cm^{-2})	FAA-3 membrane (VI activated) (25% FAA ionomer) (100 cN m)	60	150	209

200 sccm H_2 (RH = 100%) / 200 sccm O_2 (RH = 100%)	Pt/C (0.8 mg cm^{-2})	Pt/C (0.8 mg cm^{-2})	FAA-3 membrane (VI activated) (25% FAA ionomer) (150 cN m)	60	199	209
200 sccm H_2 (RH = 100%) / 200 sccm O_2 (RH = 100%)	Pt/C (0.8 mg cm^{-2})	Pt/C (0.8 mg cm^{-2})	FAA-3 membrane (VI activated) (25% FAA ionomer) (200 cN m)	60	223	209
200 sccm H_2 (RH = 100%) / 200 sccm O_2 (RH = 100%)	Pt/C (0.8 mg cm^{-2})	Pt/C (0.8 mg cm^{-2})	FAA-3 membrane (VI activated) (25% FAA ionomer) (250 cN m)	60	177	209
6 sccm H_2 (RH = 0%) / 8 sccm O_2 (RH = 0%)	Pt/C (0.5 mg cm^{-2})	Pt/C (0.5 mg cm^{-2})	AEM/PEM(Nafion)/AEM	60	78.3	211
6 sccm H_2 (RH = 100%) / 8 sccm O_2 (RH = 100%)	Pt/C (0.5 mg cm^{-2})	Pt/C (0.5 mg cm^{-2})	AEM/PEM(Nafion)/AEM	60	55.6	211
12 sccm H_2 (RH = 100%) / 6 sccm O_2 (RH = 100%)	Pt/C (0.5 mg cm^{-2})	Pt/C (0.5 mg cm^{-2})	HMEA-II (a high-pH cathode with a Nafion core membrane)	50	22	214
12 sccm H_2 (RH = 80%) / 6 sccm O_2 (RH = 80%)	Pt/C (0.5 mg cm^{-2})	Pt/C (0.5 mg cm^{-2})	HMEA-II (a high-pH cathode with a Nafion core membrane)	50	35	214
12 sccm H_2 (RH = 37%) / 6 sccm O_2 (RH = 37%)	Pt/C (0.5 mg cm^{-2})	Pt/C (0.5 mg cm^{-2})	HMEA-II (a high-pH cathode with a Nafion core membrane)	50	63	214
12 sccm H_2 (RH = 0%) / 6 sccm O_2 (RH = 0%)	Pt/C (0.5 mg cm^{-2})	Pt/C (0.5 mg cm^{-2})	HMEA-II (a high-pH cathode with a Nafion core membrane)	50	52	214
1000 sccm H_2 (RH = 95%) / 2000 sccm air (RH = 95%)	Pt/C (0.5 mg cm^{-2})	Pt/C (0.5 mg cm^{-2})	A901	50	~330	216
500 sccm H_2 (RH = 95%) / 1000 sccm air (RH = 95%)	Pt/C (0.5 mg cm^{-2})	Pt/C (0.5 mg cm^{-2})	A201	50	~260	216
500 sccm H_2 (RH = 95%) / 1000 sccm air (RH = 95%)	Pt/C (0.4 mg cm^{-2})	Pt/C (0.4 mg cm^{-2})	A201 (Pt/C:AS-4 = 6:4)	50	~20	216

500 sccm H_2 (RH = 95%) / 1000 sccm air (RH = 95%)	Pt/C (0.4 mg cm^{-2})	Pt/C (0.4 mg cm^{-2})	A201 (Pt/C:AS-4 = 7:3)	50	~275	216
500 sccm H_2 (RH = 95%) / 1000 sccm air (RH = 95%)	Pt/C (0.4 mg cm^{-2})	Pt/C (0.4 mg cm^{-2})	A201 (Pt/C:AS-4 = 8:2)	50	~140	216
500 sccm H_2 (RH = 95%) / 1000 sccm air (RH = 95%)	Pt/C (0.5 mg cm^{-2})	Pt/C (0.5 mg cm^{-2})	A201 (Pt/C:AS-4 = 7:3)	50	~260	216
500 sccm H_2 (RH = 95%) / 1000 sccm air (RH = 95%)	Pt/C (0.5 mg cm^{-2})	Pt/C (0.5 mg cm^{-2})	A201 (Pt/C:AS-X = 7:3)	50	~295	216
1000 sccm H_2 (RH = 95%) / 2000 sccm air (RH = 95%)	Pt/C (0.5 mg cm^{-2})	Pt/C (0.5 mg cm^{-2})	A901 (Pt/C:AS-X = 7:3)	50	340	216
1000 sccm H_2 (RH = 95%) / 2000 sccm O_2 (RH = 95%)	Pt/C (0.5 mg cm^{-2})	Pt/C (0.5 mg cm^{-2})	A901 (Pt/C:AS-X = 7:3)	50	450	216

Table 4 Selected hydrogen/oxygen fuel cell performance with different MEA structures reported in open literature.

Fuel/Oxidant	Anode	Cathode	Membrane	T (°C)	P(mW cm^{-2})
H_2 (RH = 100%) / O_2 (RH = 100%)	Cr/Ni (5 mg cm^{-2})	Ag (1 mg cm^{-2})	quaternary ammonium polysulphone membranes	60	50
200 sccm dry H_2 / 1000 sccm air	Pd/Ni (1.5 mg cm^{-2})	Ag (3 mg cm^{-2})	AAEM	73	400

200 sccm dry H_2 / 1000 sccm air	Pd (1.5 mg cm^{-2})	Ag (3 mg cm^{-2})	AAEM	73	180
200 sccm dry H_2 / 1000 sccm air	Ni (1.5 mg cm^{-2})	Ag (3 mg cm^{-2})	AAEM	73	70
500 sccm H_2 (RH = 100%) / 500 sccm O_2 (RH = 100%)	Pt/C (0.5 mg cm^{-2})	Pt/C (0.5 mg cm^{-2})	Tokuyama A201	50	~185
500 sccm H_2 (RH = 100%) / 500 sccm O_2 (RH = 100%)	3 nm Ru/C (0.5 mg cm^{-2})	Pt/C (0.5 mg cm^{-2})	Tokuyama A201	50	~250
500 sccm H_2 (RH = 100%) / 500 sccm O_2 (RH = 100%)	11 nm Ru/C (0.5 mg cm^{-2})	Pt/C (0.5 mg cm^{-2})	Tokuyama A201	50	~135
200 sccm dry H_2 / 1000 sccm air	Pd/C (0.3 mg cm^{-2})	Ag (3 mg cm^{-2})	AAEM	73	100
200 sccm dry H_2 / 1000 sccm air	Pd/C-CeO_2 (0.3 mg cm^{-2})	Ag (3 mg cm^{-2})	AAEM	73	500

2548

2549